Subcritical Neutron Multiplication Inference Measurements for Nuclear Data and Computational Methods Validation

by

Jennifer Arthur

A dissertation submitted in partial fulfillment
of the requirements for the degree of
Doctor of Philosophy
(Nuclear Engineering and Radiological Sciences)
in the University of Michigan
2019

Doctoral Committee:

Dr. Rian Bahran, Co-Chair, Los Alamos National Laboratory
Professor Sara Pozzi, Co-Chair
Professor Frederick Becchetti
Jesson Hutchinson, Los Alamos National Laboratory
Professor Igor Jovanovic

Jennifer Arthur

jennifera@umich.edu

ORCID iD: 0000-0002-7138-2080

Acknowledgements

This material is based upon work supported in part by the Department of Energy National Nuclear Security Administration under Award Number(s) DE-NA0002576. This work was also supported in part by the DOE Nuclear Criticality Safety Program, funded and managed by the National Nuclear Security Administration for the Department of Energy. Special thanks to my dissertation committee, Avneet Sood, Mike Rising, Patrick Talou, Nick Thompson, and Alex McSpaden for all of their help. Thank you to Joel A. Kulesza for providing the template used to present this work.

Table of Contents

List of Figures

List of Tables

List of Appendices

Abstract

Subcritical measurements have been continually performed since the 1940s, and simulation capabilities were developed alongside the measurements for comparison purposes. The accuracy of predictive radiation transport simulations is limited by the accuracy of the Monte Carlo simulation codes and underlying nuclear data. A subcritical benchmark measurement is a high-quality subcritical measurement in which all physical parameters and uncertainties are well characterized to a high degree of accuracy, and which is peer reviewed and compiled with other benchmark experiments into a database such as the International Criticality Safety Benchmark Evaluation Project (ICSBEP). Benchmark measurements are therefore trusted to provide accurate comparisons between experimental and simulated data, for nuclear data and radiation transport code validation purposes. Critical benchmarks are plentiful, but are not sensitive to correlated neutron parameters in the way that the handful of existing subcritical benchmarks are. This work demonstrates how we can apply subcritical neutron multiplication measurements and simulations to better validate relevant nuclear data and radiation transport computational methods currently used for nuclear nonproliferation and safety applications. The work encompasses the entire process of an advanced subcritical measurement, from the earliest planning stages to the final analysis and comparison to simulated results. Both the Critical and Subcritical 0-Power Experiment at Rensselaer (CaSPER) measurement, a novel advanced subcritical measurement, and the SCRαP measurement, a state-of-the-art subcritical benchmark measurement, campaigns have been completed. Simulations of LANL ICSBEP benchmark-quality reflected plutonium (BeRP) ball subcritical measurements have been conducted using various radiation transport codes that take into account the correlated physics of fission neutrons. Comparisons of both the results and the underlying neutron multiplicity models applied by the codes have been investigated, as well as new methods of applying comparisons of these subcritical neutron multiplication inference measurements and the associated simulations to nuclear data and computational methods validation. Optimization algorithm frameworks have been applied to both nuclear data evaluation based on subcritical neutron multiplication inference benchmarks, and the design of subcritical neutron multiplication inference benchmarks.

Chapter 1

Introduction and Theory

Due to the importance of measurements of multiplying special nuclear material (SNM) to the fields of nuclear nonproliferation, safeguards, and criticality safety, subcritical measurements have been continually performed since the 1940s. As a result of the improvements in nuclear detection instrumentation and SNM availability in the 1950s and 1960s, both the theory and practice of multiplication measurements were heavily investigated. These measurements take advantage of the fact that neutrons emitted in fission are correlated in time and can be used to gain knowledge about the system being measured. Simulation capabilities were developed alongside the measurements for comparison purposes. Observables of interest were found to be sensitive to the distribution of the number of neutrons emitted per fission. Therefore, neutron multiplication measurements can be used to identify and correct deficiencies in both nuclear data and Monte Carlo (MC) simulation codes. More recently (1990s and 2000s) methods of obtaining list mode data (time stamps of neutron events registered in a detector) from both measurements and simulations have also been developed and allow for more detailed comparison between the two. These predictive radiation transport simulation capabilities are extensively used in the field of nuclear nonproliferation (e.g. SNM identification and characterization, experiment planning, detection system development, etc.). In turn, the accuracy of these predictive radiation transport simulations are limited by the accuracy of the MC simulation codes and underlying nuclear data. Predictive radiation transport codes and accurate nuclear data knowledge are therefore necessary for precisely predicting the results of SNM measurements for applications such as criticality safety and nuclear nonproliferation [5].

1.1 Special nuclear material

SNM is defined as Pu, or U enriched in ^{233}U or ^{235}U. SNM therefore includes many fissile isotopes, as well as some isotopes that decay by spontaneous fission. SNM measurements and simulations are integral to nuclear nonproliferation and criticality safety, for applications

such as SNM identification and characterization, experiment planning, detection system development, and many others. Neutrons emitted in fission are correlated in time and can be used to gain knowledge about the system being measured.

The nominal density of α-phase Pu near room temperature is approximately 19.816 g/cm^3. Uranium is less dense at a nominal density of 19.1 g/cm^3. The bare sphere critical masses of ^{239}Pu, ^{233}U, and ^{235}U are 10 kg, 15 kg, and 52 kg, respectively. These values represent the masses at which a pure bare sphere of the isotope of interest will achieve a self-sustaining fission reaction. Critical mass can be reduced by increasing reflection around the sphere, and increased by increasing the neutron leakage (e.g. changing the system geometry, among other things). In general, a larger fission-to-total cross-section ratio results in a smaller critical mass for that specific nuclide. This resulting smaller critical mass is because a larger fission-to-total cross-section ratio is analogous with a larger fission-to-absorption reaction rate ratio, and therefore a more multiplying system. Thus, less mass is required to sustain a fission chain reaction. The fission, capture, and total cross-sections of ^{239}Pu, ^{233}U, and ^{235}U are plotted in Figures 1.1-1.3 as a function of incident neutron energy. All of the cross-section data are taken from ENDF/B-VII.1 [6] and plotted using the Java-based Nuclear Data Information System (JANIS).

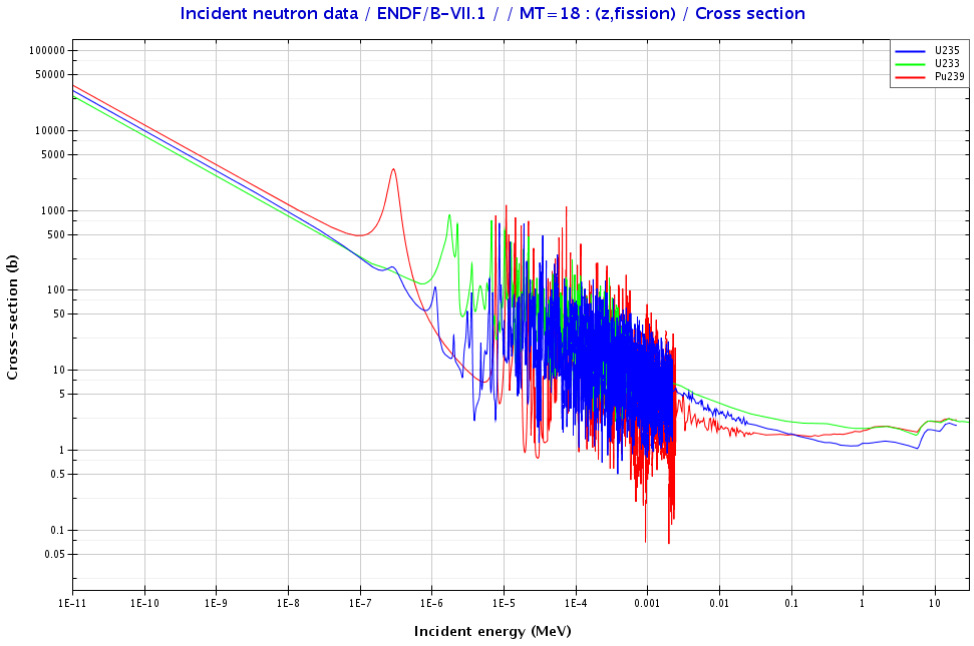

FIGURE 1.1: Fission cross-sections of ^{239}Pu, ^{233}U, and ^{235}U as a function of incident neutron energy.

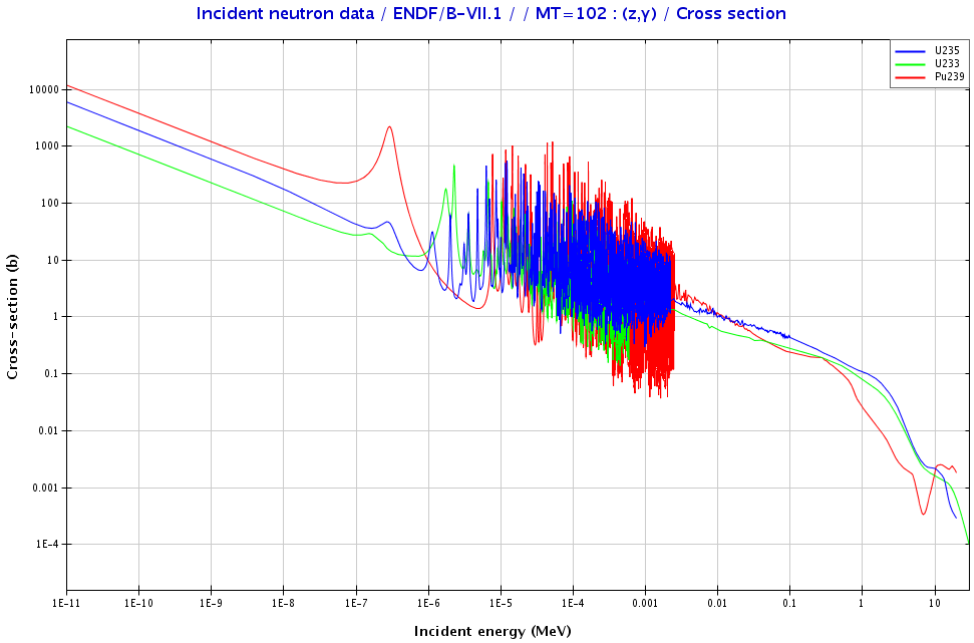

FIGURE 1.2: Capture cross-sections of ^{239}Pu, ^{233}U, and ^{235}U as a function of incident neutron energy.

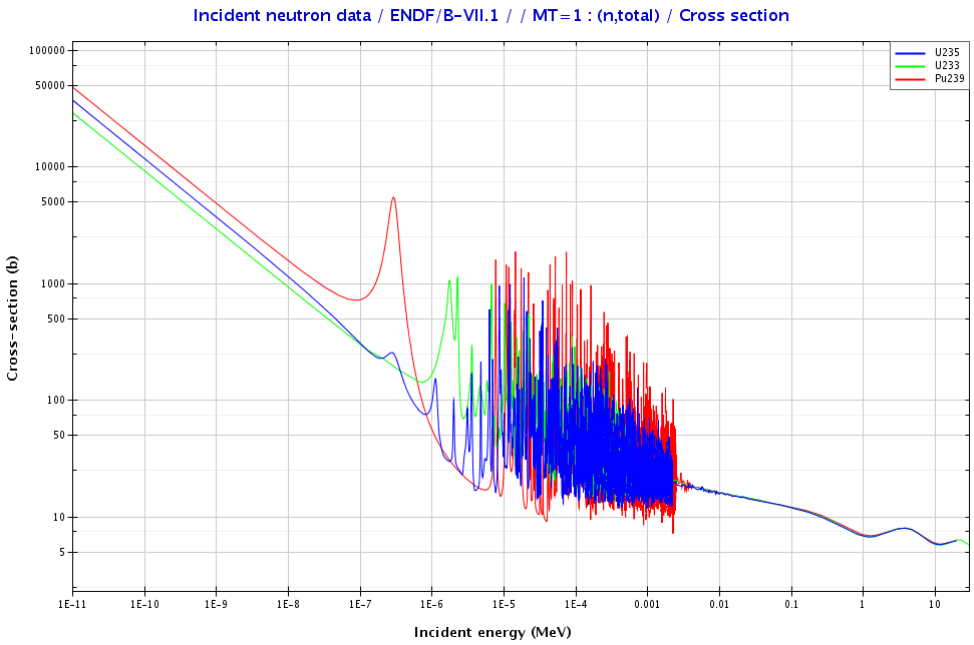

FIGURE 1.3: Total cross-sections of ^{239}Pu, ^{233}U, and ^{235}U as a function of incident neutron energy.

The fission, capture, and total cross-sections follow the $\frac{1}{v}$ law of neutron-induced reactions, with a resonance region. The $\frac{1}{v}$ law states that the probability of interaction is inversely proportional to the speed (v) at which the neutron is traveling. The resonance region is present because at specific neutron energies, the energy level structure of the target nucleus can drastically increase or decrease the likelihood of interaction. For the SNM isotopes of interest, the total cross-section is dominated by the fission, rather than the capture, portion of the total cross-section. This domination of the fission cross-section is expected for fissile isotopes, since they are capable of achieving self-sustaining fission chain reactions. The average number of neutrons released per fission of ^{239}Pu, ^{233}U, and ^{235}U are plotted versus incident neutron energy in Figure 1.4.

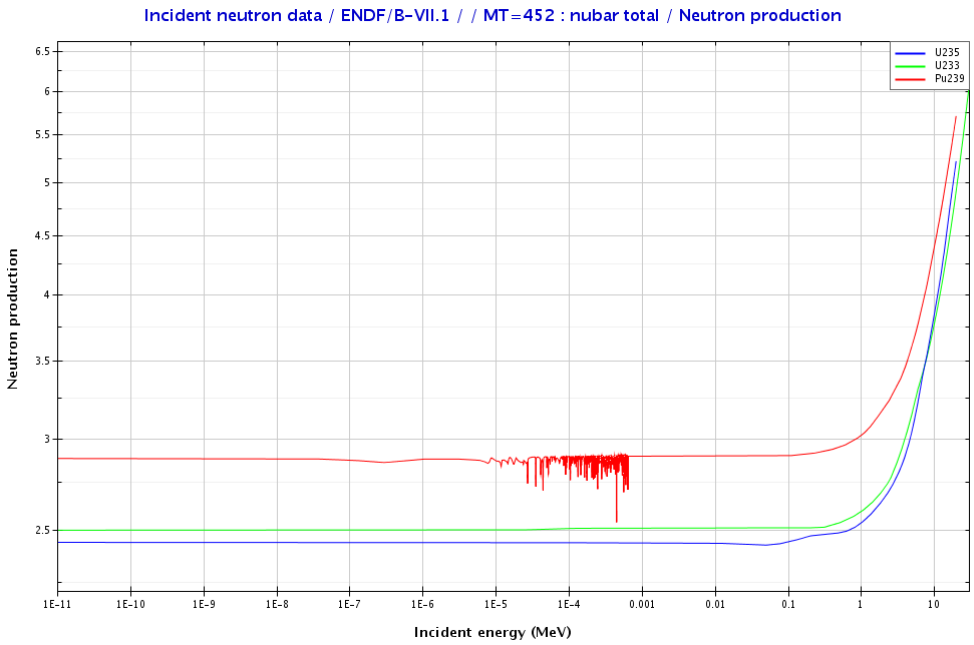

FIGURE 1.4: Average number of neutrons released per fission of ^{239}Pu, ^{233}U, and ^{235}U as a function of incident neutron energy.

^{239}Pu emits an average of 2.9 neutrons per fission, with some resonance structure around 1E-4 MeV, until 0.1 MeV. At this point the average number of neutrons begins to increase exponentially as a function of energy. The same behavior is shown by ^{233}U and ^{235}U, but with initial values of 2.5 and 2.4 neutrons per fission, respectively. ^{239}Pu, ^{233}U, and ^{235}U do undergo spontaneous fission, but their spontaneous fission yields are negligible compared to that of ^{240}Pu as shown in Table 1.1.

TABLE 1.1: Spontaneous fission yields of several SNM isotopes of interest [3].

Isotope	Spontaneous fission yield ($\frac{n}{s*g}$)
^{233}U	8.60E-4
^{235}U	2.99E-4
^{239}Pu	2.18E-2
^{240}Pu	1.02E+3

The half-lives of ^{239}Pu, ^{240}Pu, ^{233}U, and ^{235}U are listed in Table 1.2. These half-lives are all on the order of thousands of years or more, and therefore do not affect the relatively short time-scale types of SNM measurements discussed in this work.

TABLE 1.2: Half-lives of several SNM isotopes of interest [3].

Isotope	Half-life (years)
^{233}U	1.59E5
^{235}U	7.04E8
^{239}Pu	2.41E4
^{240}Pu	6.56E3

1.1.1 Fission

A fission event occurs when a nucleus either spontaneously fissions, or is induced to fission by an incident neutron colliding with the nucleus. In the case of spontaneous fission, the nucleus is inherently unstable and randomly decays by fission. In the case of neutron-induced fission, an unstable compound nucleus forms after an incident neutron collides with the original nucleus. In either case, the nucleus generally scissions into two fission fragments, which receive some of the binding energy liberated from the rearrangement of mass as kinetic energy. The fission fragments release the remaining energy in the form of prompt neutron emission, prompt gamma ray emission, and delayed β or electron conversion decay. The time from the point of scission to the emission of neutrons can range from times on the order of 1E-14 seconds for prompt neutrons to times on the order of 1E-3 to 60 seconds for delayed neutrons. Although delayed neutrons can be represented by any number of groups, they are generally represented as being emitted from 6 different groups of fission products, with the specific half-lives, energies, yields, etc. varying for different fissionable isotopes. In reality there are hundreds of fission products that emit delayed neutrons, but they are broken into groups for convenience. Delayed neutron data for fast fission of several fissionable nuclides are listed in Table 1.3.

TABLE 1.3: Delayed neutron data for fast fission of several fissionable nuclides [4]. Effective delayed neutron fractions are calculated at 2 MeV incident neutron energy.

Fission nuclide	Delayed neutron fraction	Effective neutron energy (MeV)	Effective delayed neutron fraction
^{239}Pu	0.0063 +/- 0.0003	1.58	0.0020
^{233}U	0.0070 +/- 0.0004	1.45	0.0026
^{240}Pu	0.0088 +/- 0.0006	2.13	0.0028
^{235}U	0.0165 +/- 0.0005	1.45	0.0062
^{238}U	0.0412 +/- 0.0017	3.01	0.0156
^{232}Th	0.0496 +/- 0.0020	3.50	0.0220

Because the prompt particles are emitted from moving fission fragments, the multiplicities, energies, and angles of emission of prompt neutrons and gamma rays are dependent upon both each other and the initial masses and kinetic energies of the fission fragments [7]. This dependence results in particles that are correlated in time, angle, energy, and multiplicity. The properties of the fission neutrons can be described by various probability distributions, including the multiplicity distribution $P(\nu)$ and the energy distribution $\chi(E)$. The multiplicity distribution gives the probability that ν neutrons are emitted in a fission, and the energy distribution gives the probability of a fission neutron having energy E.

Sample multiplicity and energy distributions, for ^{239}Pu induced fission at 2 MeV incident neutron energy, are shown in Figures 1.5 and 1.6. The average, $\bar{\nu}$, and width, σ , used to generate the Gaussian neutron multiplicity distribution were taken from ENDF/B-VII.1 and Lestone [8], respectively. Lestone's values of σ (typically assumed to remain constant with energy) for the SNM isotopes are listed in Table 1.4. The energy distribution was taken from ENDF/B-VII.1.

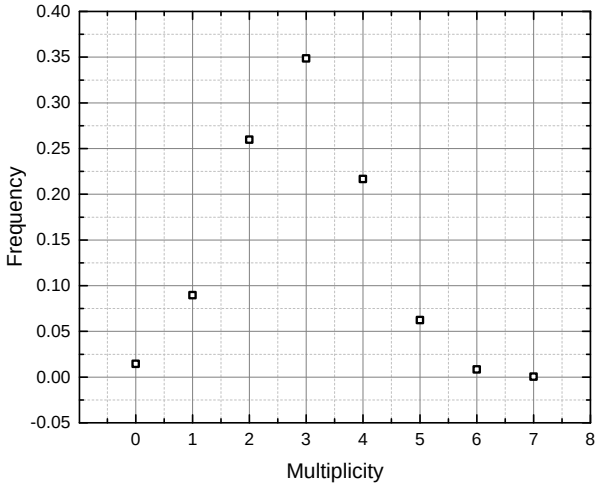

FIGURE 1.5: ^{239}Pu induced fission multiplicity distribution at 2 MeV incident neutron energy.

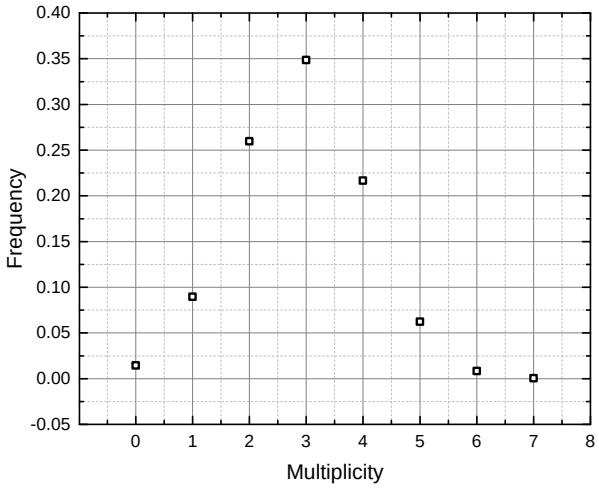

FIGURE 1.6: ^{239}Pu induced fission energy distribution at 2 MeV incident neutron energy.

TABLE 1.4: Width of the neutron multiplicity distribution for various SNM isotopes, for thermal neutron induced fission (IF) and spontaneous fission (SF).

Isotope	σ
^{233}U (IF)	1.070
^{235}U (IF)	1.088
^{239}Pu (IF)	1.140
^{240}Pu (SF)	1.151

1.1.2 Multiplication and multiplication factor

Multiplying system parameters of interest that can be inferred from fissioning systems include leakage multiplication M_L, total multiplication M_T, k_{eff}, and k_p. M_L represents the number of neutrons escaping a system for every neutron injected into the system, while M_T represents the number of prompt neutrons created on average by a single neutron in the multiplying system. The effective multiplication factor k_{eff} is a measure of ratio of the total number of neutrons in the current generation to the total number of neutrons in the previous generation, and can be related to the system multiplication M according to Equation 1.1.

$$M = \frac{1}{1 - k_{eff}} \tag{1.1}$$

However, in critical and subcritical measurements the prompt multiplication factor k_p, together with the leakage multiplication and total multiplication (Equation 1.2 [9]) are more often used to characterize the system. The symbol α represents the ratio of the capture to fission cross-sections. The prompt multiplication factor is analogous to the effective multiplication factor, but does not take into account delayed neutrons. Delayed neutrons are important for the steady state operation of a critical system, but are considered uncorrelated random neutrons for the purposes of correlated neutron detection in critical and subcritical measurements. The two multiplication factors are related by the delayed neutron fraction according to Equation 1.3. Unlike the average quantities k_{eff} and k_p, M_L and M_T are sensitive to the distribution of the number of neutrons emitted per fission $P(\nu)$.

$$M_T = \frac{1}{1-k_p} = \frac{M_L\bar{\nu} - \alpha - 1}{\bar{\nu} - \alpha - 1} \tag{1.2}$$

$$k_p = k_{eff}\,(1 - \beta_{eff}) \tag{1.3}$$

M_L and M_T can also be represented in terms of the induced fission rate per neutron ($Q_{F,n}$), $\bar{\nu}$, and the ratio of the capture cross-section to the fission cross-section ($\frac{\Sigma_c}{\Sigma_f}$) as shown in Equations 1.4 and 1.5. The effective multiplication factor can also be represented in terms of the probability of fission in the system (p_{if}) and $\bar{\nu}$ as shown in Equation 1.6 [10].

$$M_L = 1 + Q_{F,n}\left(\bar{\nu} - 1 - \frac{\Sigma_c}{\Sigma_f}\right) \tag{1.4}$$

$$M_T = 1 + Q_{F,n}\bar{\nu} \tag{1.5}$$

$$k_{eff} = p_{if}\bar{\nu} \tag{1.6}$$

1.2 Benchmark experiments

Historically, criticality safety has always been a concern for those working with systems containing nuclear material. In the early years of the nuclear industry, physical experiments were used to answer questions pertaining to criticality safety. Then, analytic calculations were performed using computers. Finally, Monte Carlo radiation transport simulation techniques were developed that allowed for accurate modeling of complex multi-dimensional systems. Because of these more accurate modeling capabilities, validation of radiation transport codes and associated basic nuclear data through comparisons with integral experimental data became an issue of importance to the criticality safety field. Experimental data is needed to increase confidence in the results obtained from simulations. Experimenters executed many measurements, but these measurements lacked quality assurance and sufficient documentation.

A benchmark experiment is a measurement in which all physical parameters and uncertainties

are well characterized to a high degree of accuracy, and which is preferably peer reviewed and compiled with other benchmark experiments into a database. The International Criticality Safety Benchmark Evaluation Project (ICSBEP) Handbook [11] contains hundreds of benchmark quality critical and subcritical measurement evaluations. The purpose of the handbook is to provide benchmark quality data that can be used for validation and improvement of nuclear databases and radiation transport codes. ICSBEP was created by the United States Department of Energy in 1992 to satisfy the need for systematic evaluation and documentation of integral experimental data, and the Organisation for Economic Cooperation and Development (OECD) - Nuclear Energy Agency (NEA) took on the project as one of its official duties in 1995 [11, 12]. The ICSBEP handbook contains thousands of benchmark quality critical and subcritical measurement evaluations from Argentina, Brazil, Canada, China, the Czech Republic, France, Germany, Hungary, India, Japan, Kazakhstan, Poland, Russia, Serbia, Slovenia, Spain, Sweden, the United Kingdom, and the United States. Each benchmark entry is separated into 4 main sections: a detailed description of the experiment, evaluation of experimental data, benchmark specifications, and results of the sample calculations. The purpose of the handbook is to provide peer-reviewed benchmark quality data for validation and improvement of nuclear databases and radiation transport codes, specifically codes that calculate the effective neutron multiplication factor [11, 12]. Several of the included measurements involve inferred multiplication measurements, wherein list-mode data is used to calculate leakage multiplication from the sample of interest. The result can then be compared to both criticality and fixed source Monte Carlo calculations for validation purposes, as shown in Figure 1.7. Raw list-mode data and other parameters of interest can also be compared. The LANL critical benchmarks are some of the most commonly used benchmark experiments for criticality testing [13].

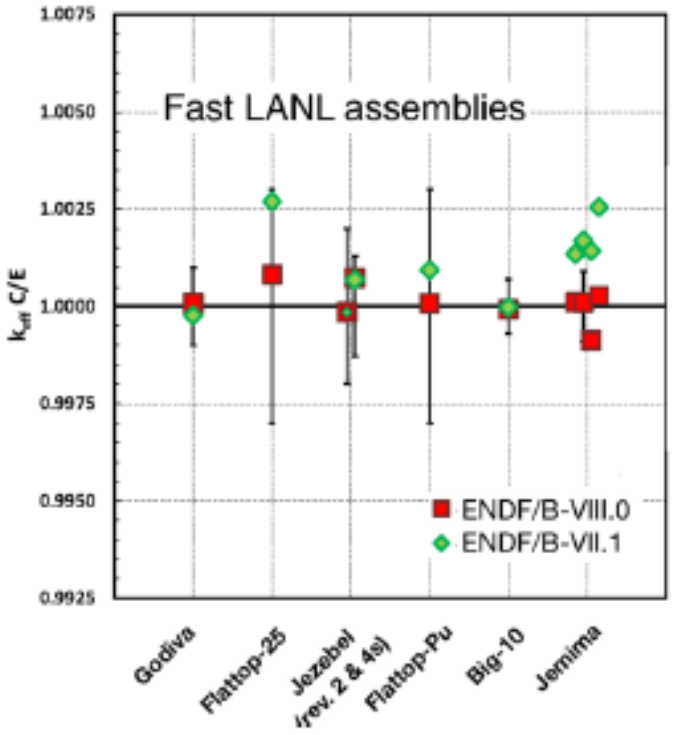

FIGURE 1.7: Calculated eigenvalue C/E values obtained with ENDF/B-VII.1 (E71) and ENDF/B-VIII.0 (E80) cross sections for a selection of fast LANL critical assemblies [1].

1.3 Critical benchmarks

A critical benchmark experiment is a benchmark experiment that consists of a system of SNM in the critical state, corresponding to an effective multiplication factor of 1. The effective multiplication factor k_{eff} is a measure of the ratio of the total number of neutrons in the current generation to the total number of neutrons in the previous generation. The prompt multiplication factor k_p is similar to k_{eff}, except that it only takes into account prompt neutrons. Critical benchmarks are plentiful, but are not sensitive to correlated neutron parameters in the way that subcritical benchmarks are.

The first critical assembly laboratory in the United States was the Kiva building at the Pajarito Canyon Site in Los Alamos. The Los Alamos Critical Experiments Facility (LACEF) allowed for remote operation of various critical assemblies over the several decades of its operation. Experiments began in 1947, for the purpose of guiding the safe handling and transportation of nuclear weapons. Some of the most prominent assemblies include Topsy,

consisting of enriched uranium with natural uranium reflection, Lady Godiva, a bare sphere of enriched uranium, Jezebel, a bare sphere of delta-phase plutonium, and Flattop, similar to Topsy but with spherical rather than block reflectors. By varying the SNM used in the different assemblies, measurements were taken of all fissile metal (^{235}U, ^{233}U, and ^{239}Pu) assemblies both bare and reflected by natural uranium. The first basic information on fast neutron chain behavior was obtained from Topsy, and was used to validate both nuclear weapon and fast reactor computational methods. Experiments using these assemblies in subcritical, near-critical, and critical configurations allowed for validation of computations of weapon super-criticality as well as other fission chain reaction characteristics. Criticality safety knowledge also grew out of these experiments. The remote operations allowed for superprompt-critical burst experiments (originally on Lady Godiva) which for a fraction of a second created a chain reaction surviving on prompt neutrons alone and therefore resulted in a massive burst of radiation. Such a burst could be created by passing a slug through a near-critical assembly of similar material. The Rover program that began in 1955 shifted the focus of critical experiments towards rocket reactor development, but was terminated in the early 1970's. The critical experiments at the Pajarito Site continued until the last experiment (using the Planet assembly) in 2004 [14–16].

Between 1947 and 2004, the LACEF site was used to conduct measurements that provided information for the design of nuclear weapons, criticality safety guidance, and the physics of the neutron-induced fission chain reaction. After this period, the Nuclear Criticality Safety Program (NCSP) became the primary sponsor for critical experiments, and continues to sponsor the execution of both subcritical and critical benchmarks at the National Criticality Experiments Research Center (NCERC) at the Nevada Test Site [16], now known as the Nevada National Security Site. The early critical benchmarks are still heavily used to this day for computational methods validations, such as in the MCNP validation suite [13].

1.4 Subcritical benchmarks

A subcritical benchmark experiment is a benchmark experiment that consists of a system of SNM that is subcritical, corresponding to an effective multiplication factor less than 1. Subcritical measurements have been continually performed since the 1940s. The results of these experiments have provided data used for simulations of SNM systems in the fields of nuclear nonproliferation, safeguards, and criticality safety. Improvements in nuclear detection instrumentation and SNM availability in the 1950s and 1960s lead to increased research activity in both the theory and practice of multiplication and reactivity measurements. Multiplication is an extremely important parameter in SNM systems, as it can give information about the

type, enrichment, and risk level of the SNM being investigated for nuclear security reasons. In addition, for criticality safety purposes, it is extremely important to be able to accurately predict the multiplication of systems for various processes and experiments. Multiplication inference measurements take advantage of the fact that neutrons emitted during fission are correlated in time and can be used to gain knowledge about the system being measured.

Multiplying system parameters of interest include leakage multiplication M_L, total multiplication M_T, k_{eff}, and k_p. As previously stated, unlike the average quantities k_{eff} and k_p, M_L and M_T are sensitive to the distribution of the number of neutrons emitted per fission $P(\nu)$. Simulation capabilities were historically developed alongside the measurements for comparison purposes. Comparisons between neutron multiplication measurements and simulations are used to validate multiplication inference techniques and radiation particle transport codes, and to identify and correct deficiencies in underlying nuclear data quantities such as $\bar{\nu}$ (average number of neutrons emitted per fission) [17–23]. Most notably, recent (1990s and 2000s) methods of obtaining list mode data from both measurements and simulations have also been developed and allow for a more detailed comparison between the two [5].

1.5 Neutron sources and background

Several sources of neutrons exist within subcritical neutron multiplication inference measurements. These sources include spontaneous fissions, induced fissions, and (α,n) reactions. Fission neutrons energies are distributed according to a Watt spectrum, with the 1 MeV being the most probable energy of emission and 2 MeV being the average energy of emission. In addition, as opposed to other source neutrons and background neutrons, only fission neutrons are correlated in time, energy, angle, and multiplicity. SNM isotopes that have appreciable spontaneous fission neutron emission rates include ^{238}Pu, ^{240}Pu, and ^{242}Pu. Spontaneous fission data for these nuclides, as well as other nuclides of interest in SNM measurements, are given in Table 1.5. Several light elements that can appear as either trace impurities or oxides of an SNM metal have high (α,n) cross-sections, as shown in Table 1.6.

TABLE 1.5: Spontaneous fission data on several nuclides of interest [3].

Isotope	Spontaneous fission yield ($\frac{n}{s*g}$)	Spontaneous fission multiplicity ($\bar{\nu}$)
^{238}Pu	2.59E3	2.21
^{240}Pu	1.02E3	2.16
^{242}Pu	1.72E3	2.15
^{238}U	1.36E-2	2.01
^{252}Cf	2.34E12	3.76

TABLE 1.6: (α,n) data on several light elements [3].

Element	Neutron yield per 10^6 α particles of energy 5.2 MeV	Average neutron energy (MeV)
Li	1.13	0.3
Be	65	4.2
B	17.5	2.9
C	0.078	4.4
O	0.059	1.9
F	5.9	1.2
Mg	0.89	2.7
Al	0.41	1.0
Si	0.076	1.2

At sea level, the average background neutron flux is known to be about 120 $\frac{n}{m^2*s}$ [24]. Cosmic events can include bursts of hundreds of neutrons within a very short time, which could potentially create a large background signal within the measured list-mode data. However, such events can be removed during the time binning step of data processing, by neglecting all larger than reasonable clusters of events.

1.6 Detectors

1.6.1 Scintillation detectors

Various types of detectors can be used in subcritical neutron measurements. One of the most commonly used types is the scintillation detector. In a scintillation detector, neutrons and gammas generally interact with nuclei or electrons, respectively, typically via scattering. The recoil charged particle then deposits energy in the detector which excites the scintillation material. The scintillation material will then de-excite, giving off light. That light is then detected by a photomultiplier tube (PMT). The scintillation material is usually coated in some sort of reflective material, so that any light not initially directed at the PMT will continuously be reflected back into the material until it reaches the PMT. The PMT converts light into electrons, which then become the detected signal. There are two main types of

scintillation detectors: organics and inorganics. Organic scintillators typically have a faster response time but lower light yield. The high Z values of inorganic scintillators make them an ideal choice for gamma ray spectroscopy, while the high hydrogen content of organics makes them suitable neutron, or dual neutron and gamma ray, detectors. Thus, organic scintillators are used for neutron multiplication measurements. Organic scintillators are advantageous when energy, particle type, or spatial information is desired in an SNM measurement.

The detected neutron and gamma ray events in an organic scintillator can be separated with reasonable accuracy by taking advantage of the different pulse shapes created by the different particles. Because neutron events involve a slower de-excitation process (due to an increased amount of inter-system crossing from the singlet into the triplet excited states), the tail end of the detected pulse is larger for neutron pulses than for gamma ray pulses. The mechanism of absorption and de-excitation is diagramed in Figure 1.8. In pulse shape discrimination (PSD) methods, a metric such as the tail-to-total ratio is used to separate neutron and gamma ray events [25]. Once the events are classified as either a neutron or a gamma ray interaction, a portion of the initial neutron energy and the gamma ray energy can also be recovered during post-processing because the pulse height and pulse integral of each event is proportional (or approximately proportional for some neutron energies) to the energy deposited by that event. Arrays of scintillation detectors do have the downside of being susceptible to neutron cross-talk, but work has been done to characterize and correct for this when estimating fissile mass of a system [26]. Work has also been done to characterize and correct for neutron cross-talk when measuring the angular distribution of ^{240}Pu spontaneous fission [27].

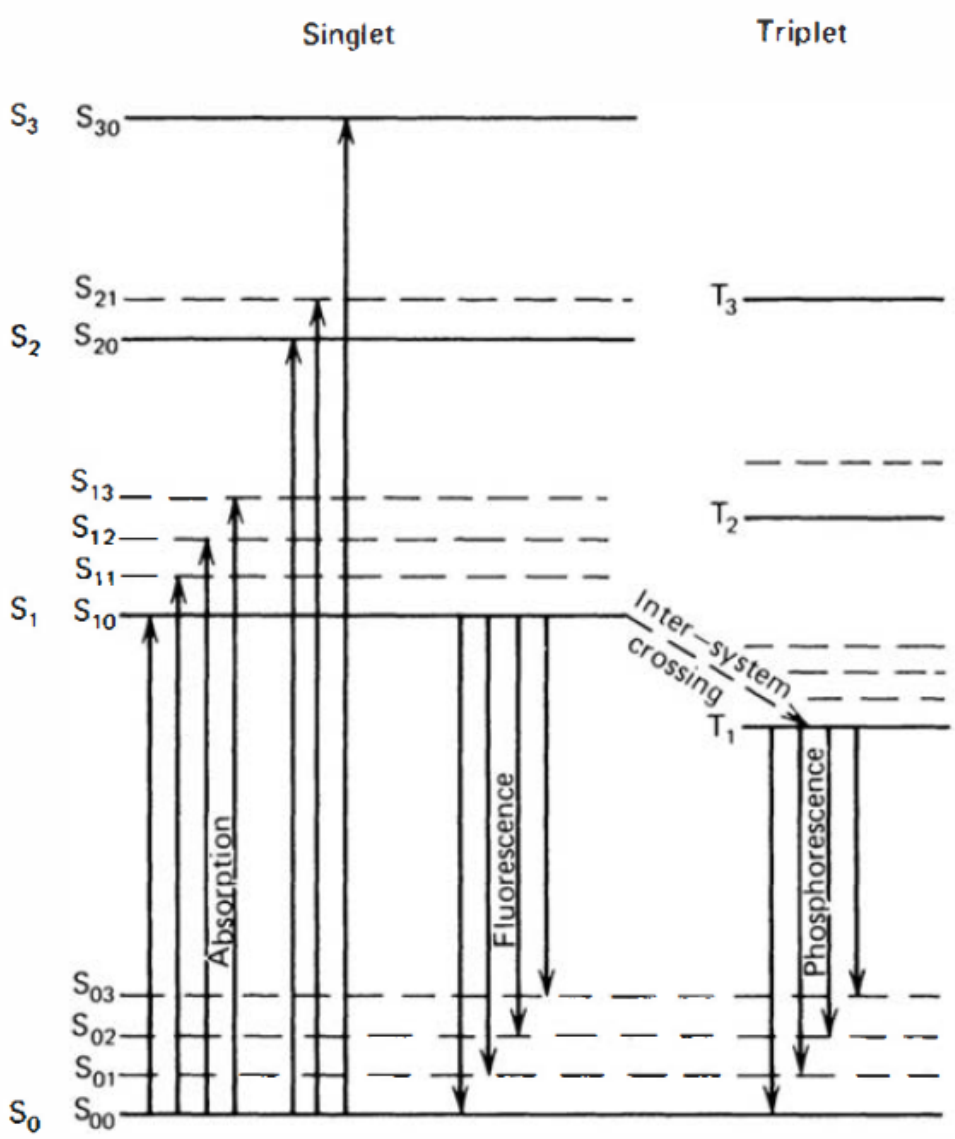

FIGURE 1.8: Energy levels of an organic scintillator molecule [2].

1.6.2 Proportional counters

Proportional counters are another type of detector that are frequently used in subcritical neutron measurements. The incident neutrons ionize the fill gas inside the proportional counter. Each ionization process creates a free electron and a positively charged ion (also called a cation). The electric field placed across the detector by a high-voltage supply forces the electron towards the anode and the cation towards the cathode. The most common

proportional counters are cylinders, with the cathode being the outer cylindrical surface, and the anode being a wire running along the central cylindrical axis of the detector. When the cations reach the outer surface cathode they do not contribute to the measured signal. As an electron gets closer to the central anode wire, an electron avalanche (Townsend avalanche) is caused by the increasing strength of the electric field within the gas just around the wire, which electric field is inversely proportional to the distance from the anode wire. This stronger electric field causes increasing amounts of charge multiplication, therefore increasing the magnitude of a detected pulse. However, this also causes dead time. The electric field is perturbed by the buildup of cation space charge caused by cations liberated from the electron avalanche drifting towards the cathode, and typically takes several micro-seconds to return to its original state.

Proportional counters operate in the "proportional" region of the pulse amplitude vs. applied voltage curve, as shown in Figure 1.9 taken from [2]. When voltage is very low, the electric field is not strong enough to prevent recombination of some of the electrons and cations liberated by the ionization process. Once the electric field is strong enough to prevent any recombination of electron-cation pairs, the ion saturation region has been reached. As the electric field becomes even stronger and the curve enters the proportional region, the electron avalanche occurs. In this region the detected pulse is proportional to the energy deposited within the detector. Very high applied voltage can cause the detector to operate in the Geiger-Mueller region, in which every detected pulse is the same magnitude and does not depend on the amount of deposited energy.

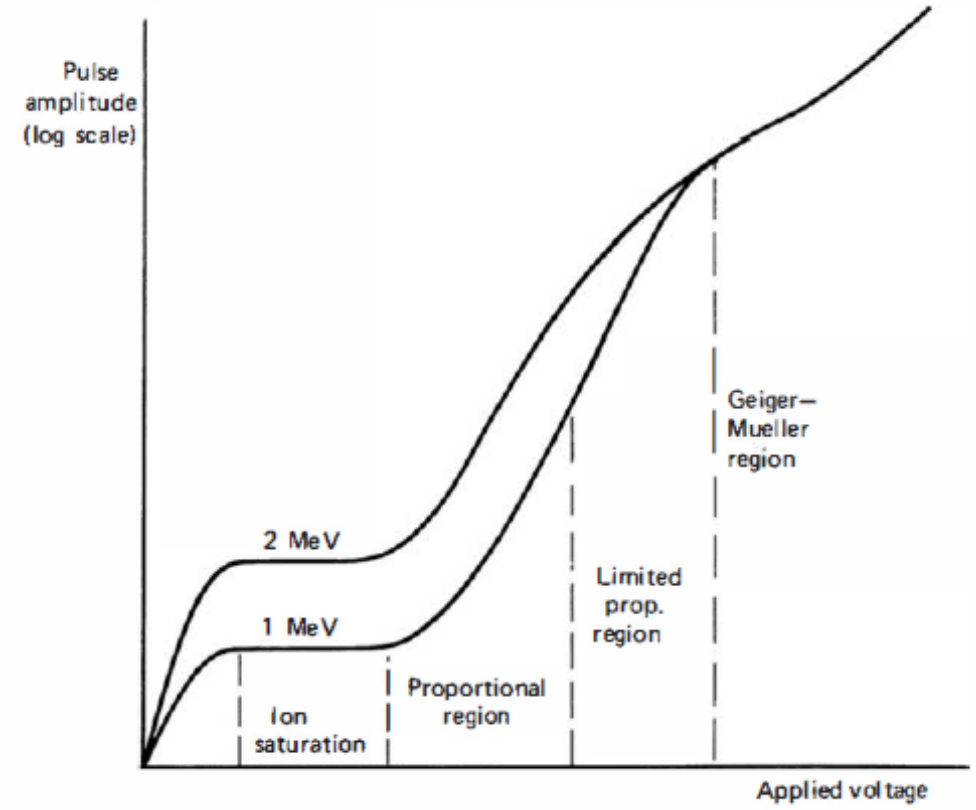

FIGURE 1.9: The different regions of operation of gas-filled detectors. The observed pulse amplitude is plotted for events depositing two different amounts of energy within the gas [2].

1.7 Neutron noise methods

Various types of neutron noise data processing methods exist. All are based on the time correlation between prompt neutrons emitted from the same fission event. All methods can be categorized as either methods of comparing the time differences between neutron events (such as Rossi-α), or moment analysis methods (such as Feynman Variance-to-Mean). Much of the following discussion is taken from the information presented in [28].

1.7.1 Rossi-α

Rossi data is a histogram of time differences between events in the list-mode data, as shown in Figure 1.10. The theory behind this method is to use the probability that a neutron will be detected in an infinitesimal time interval following a previous detected neutron event in

order to obtain the decay constant of the system. The decay constant (Rossi-α value) is obtained from a fit of the Rossi data versus time to Equation 1.7. The prompt neutron decay constant λ in Equation 1.7 is traditionally represented as α , but in this work λ is being used to represent the prompt neutron decay constant. This is because typically α is used to represent the decay constant of the fission die-away only, while λ also includes the detector system slowing down time. The Rossi equation is a summation of 2 terms because there is probability of detecting both an uncorrelated (different fission chain, or a from a source other than fission) neutron and a correlated (same fission chain) neutron. The first term of Equation 1.7 is the uncorrelated term, whereas the second term represents correlated counts. A, B, and Δ are the coefficient of the uncorrelated count contribution, the coefficient of the correlated count contribution, and an infinitesimal time window, respectively. Type I binning - taking the time difference between a single neutron and all neutrons detected later in time - is used in this work, although other methods of Rossi binning exist [29–31]. Experimental data has provided some evidence that a double exponential term for the correlated portion of the Rossi equation is more appropriate, especially for systems with reflection, which can affect the time behavior of the neutrons [32, 33]. Due to this, a probability density function (PDF) was developed which supports a double exponential fit in the case of reflected and/or moderated systems. Development of the PDF enables an analytic approximation of the uncertainty in the parameters of the fit (and therefore α) [34]. In addition, the region of subcriticality in which the system reactivity is linearly proportional to α has been investigated [29]. Sample Rossi data is plotted in Figure 1.11.

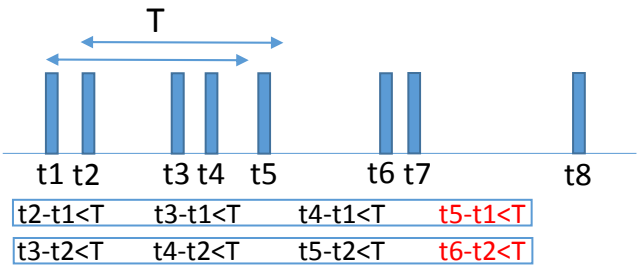

FIGURE 1.10: The time differences between events used to generate Type 1 binning Rossi data.

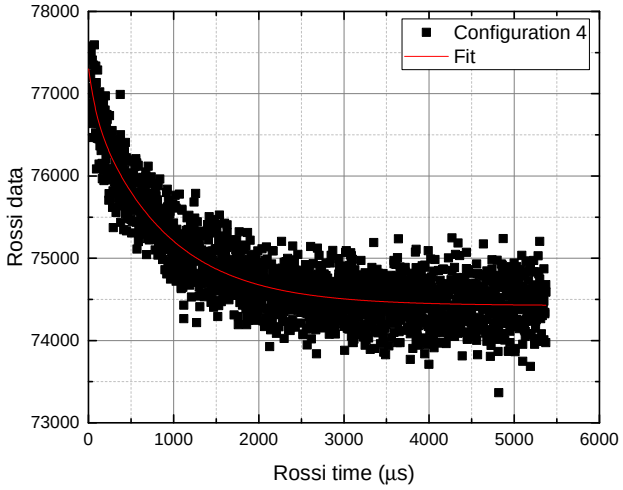

FIGURE 1.11: Sample Rossi data for configuration 4 of the CaSPER measurement.

$$P(t)\,\Delta = A\Delta + Be^{-\lambda t}\Delta \tag{1.7}$$

1.7.2 Feynman variance-to-mean

A Feynman histogram is a representation of the relative frequencies of various multiplets (i.e., 1 event, 2 events, etc.) occurring within the specified gate width. To illustrate the binning method, Figure 1.12 shows a sample series of events for a very short measurement time. Figure 1.13 then shows how the events are sorted into different gates, using 2 different values of the gate width τ. The very simple Feynman histograms produced by binning the multiplets of each gate width for the 2 different gate width sizes are plotted in Figure 1.14. This example illustrates how a larger gate width shifts the histogram to larger multiplets, but also decreases the overall number of gates. An actual Feynman histogram would consist of a very large number (millions) of gate widths rather than just a few.

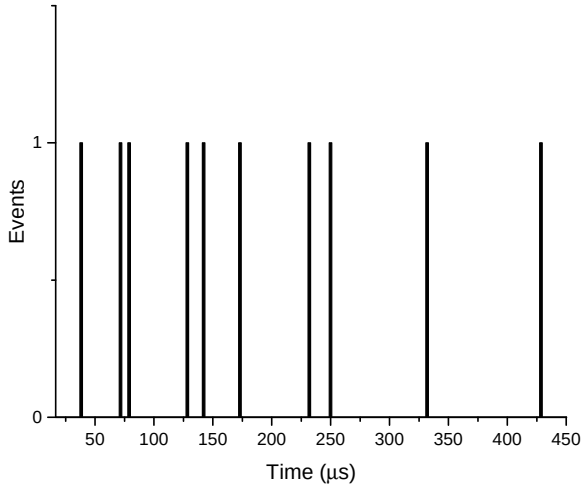

FIGURE 1.12: Sample series of events over a very short measurement time.

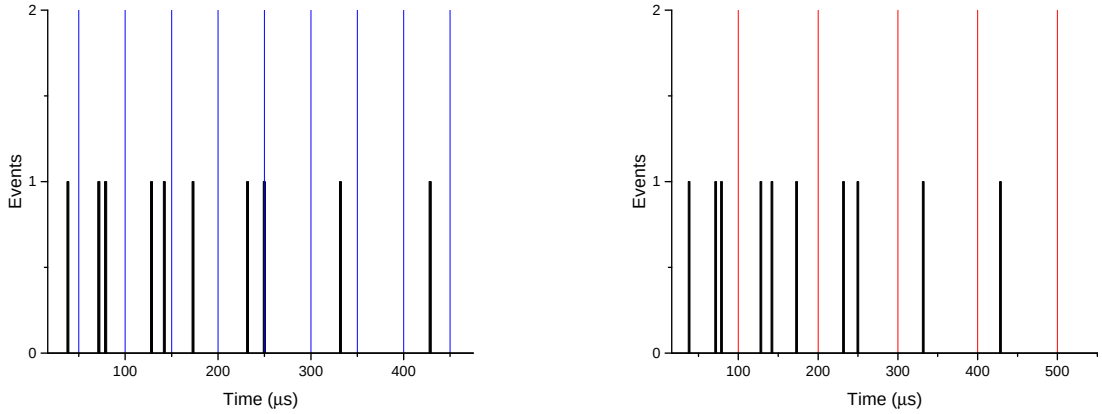

FIGURE 1.13: Application of gate widths $\tau = 50\mu s$ (left) and $\tau = 100\mu s$ (right) to the sample series of events. The blue and red lines indicate the boundaries of the various gates.

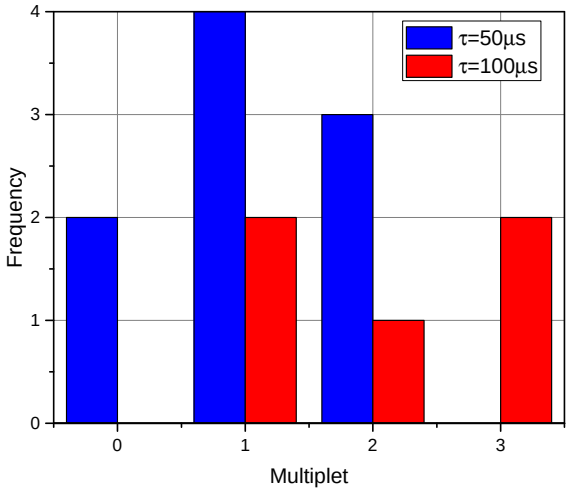

FIGURE 1.14: Feynman histograms created by applying the different gate widths to the sample series of events.

The principle of the Feynman variance-to-mean method is to calculate the relationship between the variance of the number of counts detected in a certain time gate width to the mean of the number of counts detected in the same gate width. The distribution of the "number of counts detected in a certain gate width" is simply the Feynman histogram. The Feynman histogram representing an independent random process is Poissonian, therefore the variance is equal to the mean of the distribution. As the multiplication (and therefore correlation between detected neutrons) of a system increases, the histogram diverges further from a Poissonian distribution as the variance becomes representative of a chain-related variable rather than a random variable.

The magnitude of the n^{th} bin of the Feynman histogram at the specified gate width τ is represented by the variable $C_n(\tau)$ in Equation 1.8. Standard multiplicity equations, in the form of Equations 1.8-1.16 [35], are applied to calculate the singles (R_1) and doubles (R_2) rates, as well as the leakage multiplication (M_L). The "singles" rate is defined as the rate of detection of single neutrons from a fission chain. The "doubles" rate is defined as the rate of detection of two neutrons from the same fission chain. M_L represents the average number of neutrons that escape the system following the introduction of a single neutron to the system. Equation 1.13 is Equation 1.12 evaluated at $\mu = 2$, which is needed to

calculate the doubles rate. Equations for the uncertainties in R_1, R_2, and M_L can be found in reference [35]. In the following equations, the symbols λ, ϵ , ν_{Ii} and ν_{si} represent the prompt neutron decay constant, detector absolute efficiency, i^{th} moment of the induced fission multiplicity distribution, and i^{th} moment of the spontaneous fission multiplicity distribution, respectively. $m_r(\tau)$ is the r^{th} reduced factorial moment of the Feynman histogram. Y_2 is directly proportional to the Feynman Y value, which is a measure of the deviation of the histogram from a Poisson distribution. The prompt neutron decay constant λ can be obtained by fitting the normalized Y_2 data to the form of Equation 1.13.

$$p_n(\tau) = \frac{C_n(\tau)}{\sum_{n=0}^{\infty} C_n(\tau)} \tag{1.8}$$

$$m_r(\tau) = \frac{\sum_{n=0}^{\infty} n(n-1)\ldots(n-r+1)\, p_n(\tau)}{r!} \tag{1.9}$$

$$R_1(\tau) = \frac{m_1(\tau)}{\tau} \tag{1.10}$$

$$Y_2(\tau) = \frac{m_2(\tau) - \frac{1}{2}\left[m_1(\tau)\right]^2}{\tau} \tag{1.11}$$

$$\omega_\mu(\lambda,\tau) = \sum_{K=0}^{\mu-1} \binom{\mu-1}{K} (-1)^K \frac{1-e^{-\lambda\tau K}}{\lambda\tau K} \tag{1.12}$$

$$\omega_2(\lambda,\tau) = 1 - \frac{1-e^{-\lambda\tau}}{\lambda\tau} \tag{1.13}$$

$$R_2(\tau) = \frac{Y_2(\tau)}{\omega_2(\lambda,\tau)} \tag{1.14}$$

$$M_L = \frac{-C_2 + \sqrt{C_2^2 - 4C_1C_3}}{2C_1} \tag{1.15}$$

$$C_1 = \frac{\nu_{s1}\nu_{I2}}{\nu_{I1} - 1},\ C_2 = \nu_{s2} - \frac{\nu_{s1}\nu_{I2}}{\nu_{I1} - 1},\ C_3 = -\frac{R_2(\tau)\,\nu_{s1}}{R_1(\tau)\,\epsilon} \tag{1.16}$$

Because the value of M_L is calculated (i.e., inferred) and not directly measured, measurements that utilize the Feynman variance-to-mean method are typically referred to as neutron multiplication inference measurements. The general equations for ν_{Ii} and ν_{si}, in terms of the neutron multiplicity distribution $P(\nu)$, are shown in Equations 1.17 and 1.18 [35].

$$\nu_{Ii} = \frac{1}{i}\sum \nu_I(\nu_I - 1)...(\nu_I - i + 1)P(\nu_I) \tag{1.17}$$

$$\nu_{si} = \frac{1}{i}\sum \nu_s(\nu_s - 1)...(\nu_s - i + 1)P(\nu_s) \tag{1.18}$$

1.7.3 Other methods

One disadvantage of the Feynman variance-to-mean method is the divergence of the multiplicity equations as the system approaches delayed critical. The Bennett variance method was therefore developed to still be applicable near delayed critical. Rather than using the variation in the number of counts in subsequent time intervals, this method uses the 2^{nd} moment (derivative) of the variation of the number of counts in subsequent time intervals. This use of the variation of the number of counts in subsequent time intervals causes the system to behave as a subcritical system from a statistical perspective. However, results of this method show that the correlation in the derivative of the distribution (Bennett) is smaller than the correlation in the distribution itself (Feynman) [36].

Count probability methods define the probability distribution in Equation 1.7 as a function of the physical nuclear parameters describing the system of interest. The zero probability (or Mogilner) method specifically utilizes the fraction of all time intervals during which zero events are recorded, as the time interval is varied greatly. This method is typically only used with thermal systems at very low power because a statistically significant number of empty time intervals are necessary [37]. The Polya-model method measures the probability of a wide range of multiplets occurring within the time interval as the time interval is varied, and compares this to the Feynman histogram [38].

The interval distribution (or Babala) method calculates the distribution of the lengths of time intervals between subsequent detection events. This method results in either a count-to-count distribution or a random-origin distribution, depending on which technique is preferred. The random-origin technique follows the same principle as the count-to-count technique, except that the start of the time interval is chosen randomly rather than being triggered by an initial detection event. For fast reactors the count-to-count distribution simplifies to the Rossi-α distribution [39]. In general, the interval distribution method can be useful for determining dead time for any channel in a detector system.

In the dead-time (or Srinivasan) method, the detection equipment dead time is artificially varied, which variation affects the amount of correlation between detected events [39]. Correlation analysis techniques use the cross-correlation function, which is the joint probability distribution of an initial event occurring at time t_1 followed by a subsequent event at t_2. By defining the time interval between t_1 and t_2 as the independent variable, the probability distribution becomes the Rossi-α distribution multiplied by a constant. Covariance measurements use the output from two different neutron detectors to calculate the covariance (difference between the expected value of the multiplication of two variables and the multiplication of the expected values of the two variables) between the different sets of data. This method is sometimes preferred over the Feynman variance-to-mean method due to the fact that it reduces the bias that affects finite time measurements. The endogenous-pulsed-source technique triggers data collection only when the variable neutron flux in the system rises above the mean value by a specific amount. The decay of the neutron population is then, as in Rossi-α, governed by the decay constant α. However, because data collection is triggered instead of constant, the signal-to-noise ratio is larger than that of the Rossi method [28].

1.8 Nuclear data

For the purposes of this work we will focus on the nuclear reaction database utilized by the general purpose Monte Carlo (MC) code MCNP®6.2[1], namely the Evaluated Nuclear Data File (ENDF) [1, 6]. ENDF contains information related to the types and probabilities of the different possible reactions between radiation particles and various nuclides. Evaluators use data from high-quality differential measurements to evaluate nuclear data libraries such as ENDF, and comparisons of simulated and measured data from benchmark-quality integral measurements to validate the libraries. Figure 1.15 summarizes the process. Included in the information provided by ENDF are data summarizing both the probability of fission

[1]MCNP® and Monte Carlo N-Particle® are registered trademarks owned by Los Alamos National Security, LLC, manager and operator of Los Alamos National Laboratory.

occurring and the average number of neutrons released per fission of each fissionable nuclide, represented as $\overline{\nu}$, as functions of incident neutron energy. If assumed to be Gaussian, neutron multiplicity distributions can be described by a set of 2 nuclear data values. These are $\bar{\nu}(E)$, the average number of neutrons emitted per fission for a given isotope at a given incident neutron energy, and σ, the standard deviation of the number of neutrons emitted per fission for a given isotope. The standard deviation is typically assumed to remain relatively constant across all incident neutron energies. Complete multiplicity distributions, $P(\nu)$, are not included in either ENDF/B-VII.1 or ENDF/B-VIII.0; correlations in angle and energy are also not included. Some examples of tabulated data describing $P(\nu)$ are those by Lestone, Santi, and Terrell [8, 40, 41]. Examples of fission cross-section and $\overline{\nu}$ values as a function of incident neutron energy for some fissile isotopes of interest are plotted in Figure 1.16.

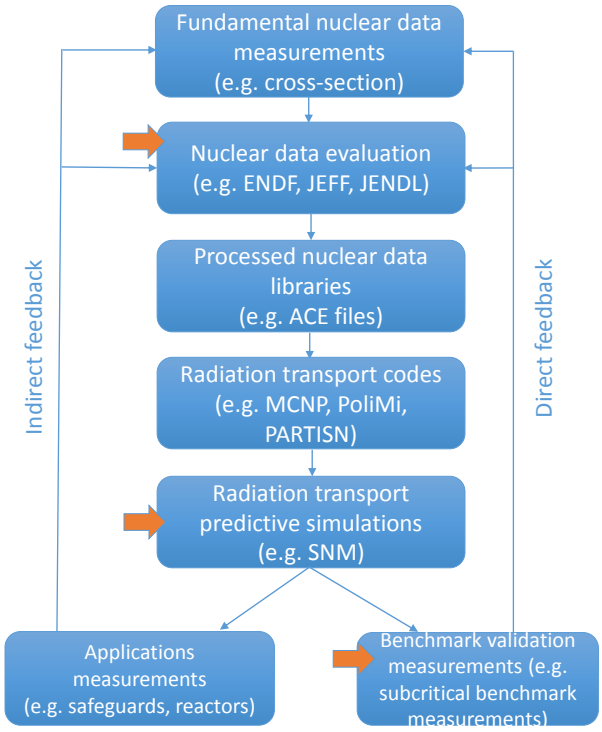

FIGURE 1.15: The nuclear data evaluation and validation process. Arrows indicate the steps in the process that this work focuses on.

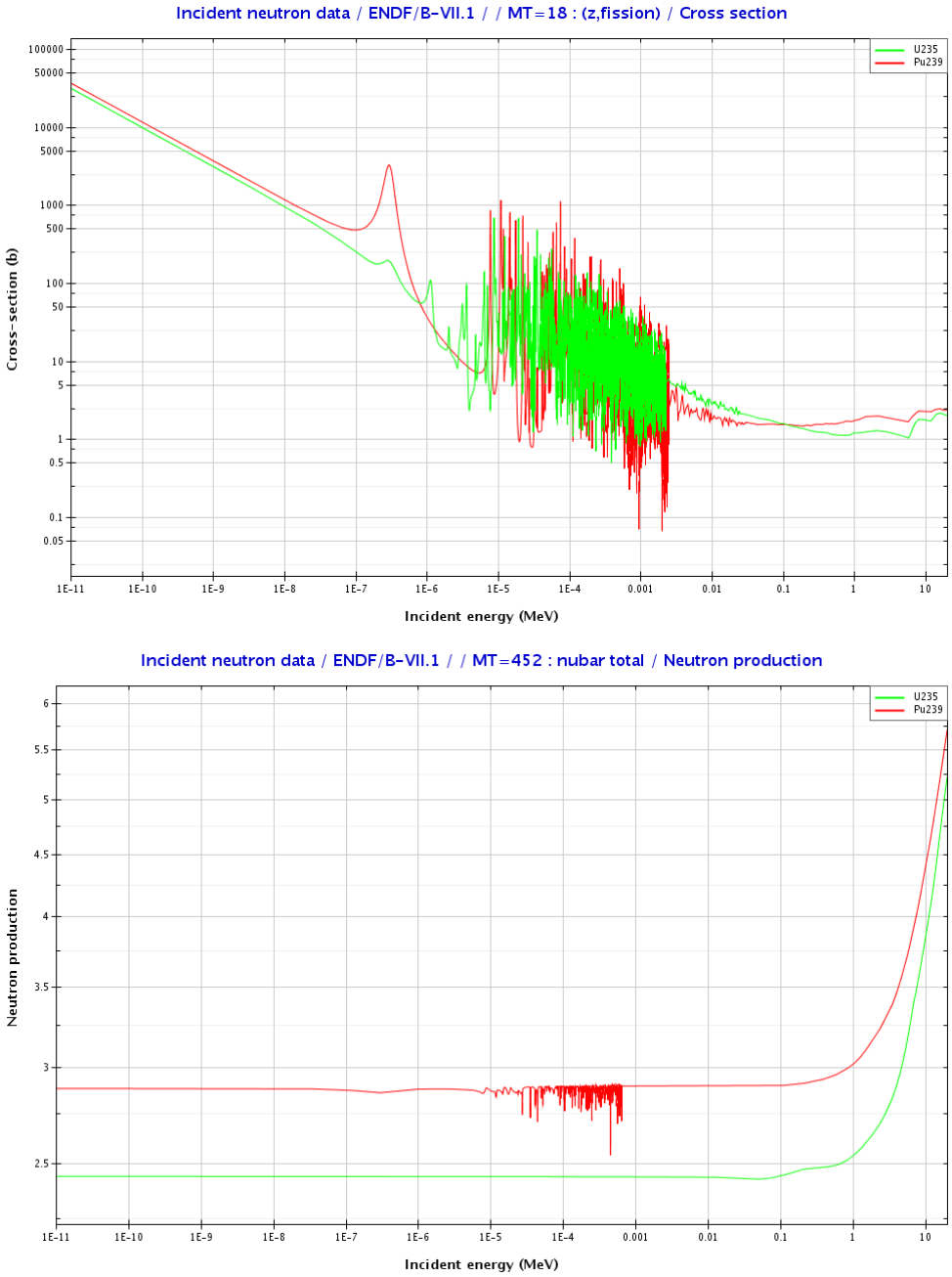

FIGURE 1.16: Fission cross-section and $\overline{\nu}$ vs. incident neutron energy for some fissile isotopes of interest, taken from ENDF/B-VII.1 using the nuclear data plotting tool JANIS.

Overall, the ENDF evaluation process focuses on complying as closely as possible with differential experimental data contained in the CSISRS (or EXFOR) database [42], while

simultaneously showing general agreement with critical benchmark measured data. Evaluators did not make any changes to $\bar{\nu}$ between the previous evaluation (ENDF/B-VII.0) and the evaluation used in this work (ENDF/B-VII.1) [43]. Therefore, the evaluation process of the ENDF/B-VII.0 version will be described with regard to $\bar{\nu}$. For the ENDF/B-VII.0 evaluation, the experimental database from the ENDF/B-VI evaluation was used, with corrections to the normalization of the $\bar{\nu}$ nuclear data. These corrections resulted in evaluations that match well with the corrected experimental database for ^{235}U, ^{238}U and ^{239}Pu. Appreciable deviation from experimental data occurs in the energy range below 1.5 MeV for ^{239}Pu, and this is partially due to the desire to match JEZEBEL (a LANL fast critical benchmark experiment) results in particular [43]. The bulk of the simulations performed in this work were done using ENDF/B-VII.1 because ENDF/B-VIII.0 had not yet been released. However, some limited results with ENDF/B-VIII.0 are include in some sections of this work. The most significant change in terms of this work is the overall decrease of ^{239}Pu $\bar{\nu}$ in ENDF/B-VIII.0.

One of the main parameters of interest that is used to validate ENDF is the effective multiplication factor k_{eff}, which is sensitive to $\bar{\nu}$ but not to the other moments of the $P(\nu)$ distribution. The effective multiplication factor is in general insensitive to changes in the correlated physics of fission and depends only on averages. This insensitivity can be illustrated by examining the neutron transport equation, which consists of terms representing the loss of neutrons due to leakage out of the system, the loss of neutrons due to all interactions, the addition of neutrons due to in-scattering from another energy group, and the production of neutrons due to fission. Only the average quantity $\bar{\nu}(E)$ is required to calculate neutron transport and the effective multiplication factor of a system. However, by looking at the Hage-Cifarelli equation for the leakage multiplication of a system, in Equations 1.15 and 1.16, it is clear that other moments of the multiplicity distribution (ν_{s2}, ν_{I2}) are also important.

Integral experiments, such as JEZEBEL, are continually being used to validate nuclear data items of interest, such as ^{239}Pu $\bar{\nu}$. The LANL critical experiments are some of the main benchmarks used to test out new cross-section library versions (as shown in Figure 1.7). The MCNP criticality validation suite also uses these LANL critical benchmarks [13], and work is being done to add a suite of subcritical benchmarks that can increase the range of nuclear data items being validated [44].

The average number of neutrons released per fission is a specific measured observable of some of the differential measurements of fission product yields, masses, and fission neutron energy spectra contained in EXFOR. Because of the contribution of neutrons from interactions other

than fission, it is difficult to measure characteristics of the fission neutrons only, such as the spectra or the number released per fission, especially at high incident neutron energies. In addition, some actinides are not readily available in a very pure isotopic concentration, and impurities affect the observed yields. Methods such as time-of-flight, multiplicative transmission through a fissionable target, and gamma-ray spectroscopic techniques have been used to measure fission yields, but overall few measurements of this type have been conducted. As a result of the lack of reliable differential fission yield measurements, semi-empirical calculations and systematic fission models have been used by nuclear data evaluators [45–52]. Thus, integral measurements that are sensitive to the nuclear data corresponding to fission yields, such as $\bar{\nu}$ and fission neutron energy spectra, are very important for fission yield nuclear data validation and evaluation.

1.9 Simulations

Radiation transport codes can be divided into two categories: deterministic and stochastic. Deterministic neutron transport is predicated on solving the neutron transport equation for the desired unknown value (such as k_{eff} or a reaction rate), using known input parameters. Therefore, deterministic radiation transport codes are only capable of returning average quantities, and are not able to provide a solution to problems that require tracking of non-average quantities. Stochastic neutron transport uses Monte Carlo (MC) methods to track the path and interaction(s) of each particle in the transport simulation. Because MC transport calculates information for each individual particle in the simulation, many non-averaged, event-by-event quantities can be obtained. The computer time required to complete a simulation is often much longer for MC simulations.

The radiation transport code that will be focused on in this work is the Monte Carlo N-Particle (MCNP) code, the precursors of which were originally developed during the Manhattan Project era to simulate neutron diffusion and multiplication in fissioning systems [53]. MCNP can be run in either criticality eigenvalue mode or fixed-source mode. In criticality eigenvalue mode, due to the presence of the fissionable source of neutrons, the neutron transport equation becomes an eigenvalue equation with k_{eff} as the corresponding eigenvalue. The calculation converges on the steady-state behavior of the system by simulating successive generations of neutrons in the system. In fixed-source mode (named fixed-source because, as opposed to eigenvalue calculations, the source term does not change throughout the course of the simulation) a source of particles is defined and the desired number of particles is simulated until all primary and secondary (created by reactions of primary or other secondary particles during the simulation) particles have been captured within the system or have leaked out

of the boundaries of the defined system. Typically tallies are used to obtain the results of interest from fixed-source calculations. Tallies can output various properties of the simulated system, such as the flux of particles within a volume, the energy deposited by particles interacting within a detector material, and many others.

If event-by-event information is desired, the particle track (PTRAC) output must be used. The PTRAC file contains information about all particle interactions that occurred during the MCNP simulation. In order to produce list-mode data the MCNP input file must be run in analog mode, such that the weights of all particles are always unity. Using PTRAC parsing capabilities from the MCNPtools package [54, 55], the time and detector of interaction corresponding to each event can be pulled from the PTRAC file and input into a list-mode data file (LMX file) containing only those two pieces of information. Simulated list-mode can then be processed in the same way as measured list-mode data. It is important to note that because simulated data starts at a specific time t=0, while measured data can originate from events occurring at times t<0, simulated and measured data do disagree at very small times. In order to correct for this discrepancy, the simulation can be run for slightly longer than the desired time, and the first several seconds of the resulting list-mode data is then removed.

The correlated physics of fission can also be accounted for in MC radiation transport simulations [56, 57]. By default, MCNP uses a bounded integer treatment and the data from ENDF to sample the number of neutrons emitted from each simulated fission event. In the bounded integer treatment, the two integers closest to the mean are the only values that are sampled, instead of a complete multiplicity distribution. Random sampling is used to decide which of those two integers are sampled such that the mean value is preserved. The FMULT card, an optional input in MCNP that allows for user definition of spontaneous and induced fission parameters, can be utilized to call either built-in or user-specified multiplicities to replace the bounded integer treatment. The user can also use the FMULT card to call either the Fission Reaction Event Yield Algorithm (FREYA) [58] or the Cascading Gamma-Ray Multiplicity with Fission (CGMF) [59] fission event generating codes to handle fission. The FREYA fission event generator determines the number, energy, and direction of particles emitted for each fission event and gives the results to MCNP for transport. The fission event generator uses fission fragment mass and kinetic energy distributions, unbounded statistical evaporation models, and conservation of energy and momentum to generate the number, energy, and direction of neutrons released by each fission event using the Monte Carlo Weisskopf approach. CGMF generates prompt fission neutrons using the statistical Hauser-Feshbach formalism and gives results to MCNP for transport. PoliMi, a separate MC

transport code, utilizes a few different built-in multiplicity sets, and also models both the anisotropy and multiplicity-dependent energy spectra of neutrons emitted in spontaneous fission.

Chapter 2

Background and Motivation

2.1 Recent subcritical benchmarks

Recently there has also been significant progress on the design and execution of benchmark quality subcritical neutron multiplication measurements for radiation transport code and nuclear data validation. The majority of these experiments have involved a 4.5 kg alpha-phase plutonium sphere (BeRP ball) surrounded by copper and polyethylene [60], tungsten [9], and nickel [61]. Evaluations of the nickel and tungsten measurements have both been accepted into the ICSBEP handbook. The nickel benchmark was the first ICSBEP-accepted evaluation of measurements analyzed with the Hage-Cifarelli formalism based on the Feynman Variance-to-Mean method [62], and was the culmination of many years of collaborative subcritical experiment research [5, 9, 17–22, 61, 63–66]. Although the state-of-the-art has been advancing throughout the years, benchmark measurements have only been done with simple SNM geometries. There has been no protocol before this work on how to best perform, and what can be learned from, measurements on increasingly complex reactor systems, such as zero-power pin-type pool research reactors.

The typical reflected plutonium subcritical benchmark measurement setup involves the BeRP ball surrounded by various thickness of metal reflectors, with multiplicity detectors 50 cm on either side, as shown in Figure 2.1. The BeRP-Ni benchmark geometry consists of the BeRP ball surrounded by various thicknesses of nickel reflectors, ranging from 0 in. to 3.0 in. The BeRP-W benchmark consists of the BeRP ball surrounded by various thicknesses of tungsten reflectors, ranging from 0 in. to 3.0 in. The SCRαP benchmark geometry consists of the BERP ball surrounded by eight different copper thicknesses, seven different combined HDPE-copper thicknesses, and one HDPE-only configuration.

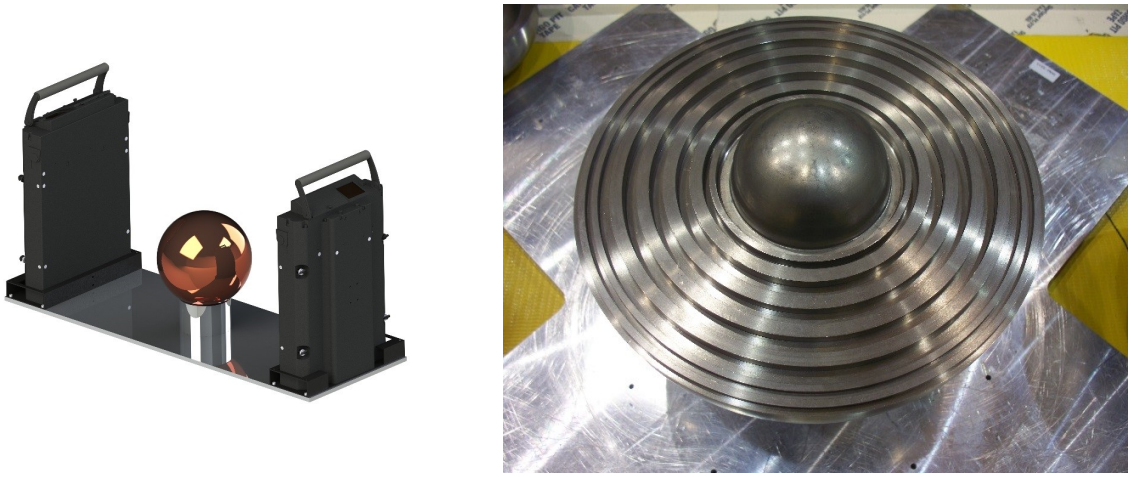

FIGURE 2.1: CAD image of a typical reflected plutonium setup (left), and picture of the BeRP ball within metal reflector shells (right).

Four different types of reflector materials have been included in the subcritical benchmarks which have been performed up to now: Ni, W, Cu, and high-density polyethylene (HDPE). Neutrons born from fission do not lose much energy to collisions with metal nuclides, due to the high mass numbers of these isotopes. HDPE, however, is a very good moderator for neutrons. The neutron elastic scattering cross-sections for the most abundant isotopes of these materials are plotted in Figure 2.2.

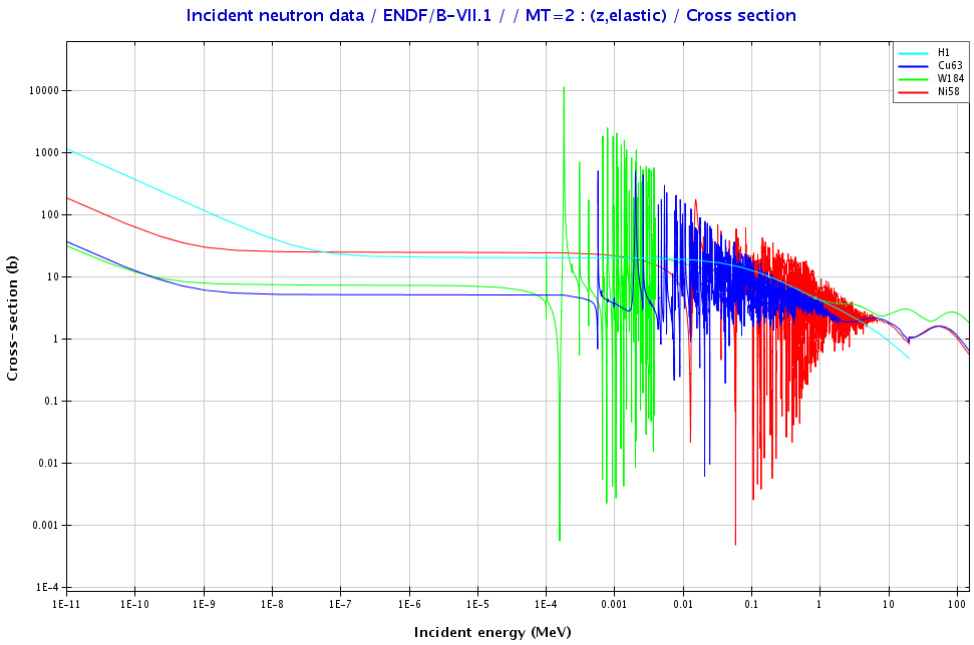

FIGURE 2.2: Reflector material neutron elastic scattering cross-sections.

Although the neutron scattering cross-sections are similar for the metals and hydrogen, neutrons are much more likely to lose a larger percentage of their energy to a hydrogen nucleus than to a metal nucleus. This increased loss of energy is due to conservation of energy and momentum, and the fact that the mass of a hydrogen nucleus is very close to the mass of a neutron, while the metal nuclei have orders of magnitude more mass. HDPE and metal reflection both affect parameters such as the multiplication, average neutron energy, and slowing down time of the system.

Typically a subcritical benchmark is designed to maximize the sensitivity of k_{eff} (and therefore M_L) to a specific cross-section, energy range, and/or isotope of interest. This is to faciliate the validation process of cross-sections of interest using observables obtained from the subcritical benchmark measurements and simulations. Equation 2.1 defines the type of sensitivities that are calculated in MCNP using adjoint transport methods [67]. In this equation $S_{k,x}$ is the sensitivity of k_{eff} to the nuclear data item x_j, corresponding to the isotope j. Prior to the emergence of these capabilities in the last decade or so, all experiments were designed based opon intuition or flux simulations. The new critical and subcritical experiments can utilize these sensitivity calculation capabilities to design experiments which maximize sensitivities

to cross-sections corresponding to nuclides and energy ranges of interest.

$$S_{k,x} = \frac{x^j}{k}\frac{dk}{dx^j} \tag{2.1}$$

2.2 Neutron sources and background in this work

The spontaneous fission (s.f.) rate of the BeRP ball at the time of the BeRP-Ni measurement was 128511 s.f./s. Assuming an average of 2.154 neutrons emitted per spontaneous fission [35], this translates to 276813 n/s emitted by spontaneous fission. The (α,n) reaction rate (and therefore the non-fission neutron emission rate) at the time of the BeRP-Ni measurement was 4122 n/s. It is clear from these numbers that the measured signal in a BeRP measurement is dominated by fission within the SNM.

The effect of room return on both BeRP-Ni and BeRP-W subcritical benchmarks has been investigated as part of the benchmark process and determined to be very small. Including both cases, the largest observed bias in detector count rate obtained from removing the concrete walls, floor, and ceiling from the MCNP model is -4.2% [9, 61]. For the research reactor measurement in this work, however, the measured signal was dominated by the PuBe starter source located above the reactor core (see Appendix A). Thus, background sources of neutrons became even more negligible in the presence of the PuBe starter source. This additional source of neutrons was taken into account as described in detail in the research reactor measurement section of this work.

2.3 ^{3}He detectors

^{3}He detectors are a type of proportional counter, based on the ^{3}He neutron capture reaction shown in Equation 2.2. This reaction creates an oppositely directed proton and triton, with respective energies of 573 keV and 191 keV. Because the cross-section for this reaction is highest at thermal neutron energies (Figure 2.3, from [2]), when detecting fission neutrons ^{3}He detector tubes are usually surrounded by hydrogenous material that serves as a moderator for the incoming fast neutrons. ^{3}He detectors measure neutron count-rate only (no energy information if surrounded by a moderator) and are negligibly sensitive to gamma rays. Since no neutron energy information is provided by this type of detector, detectors that yield energy information (such as the aforementioned scintillation detector) could be a useful addition to neutron multiplicity measurements in which energy information was also desired.

$$^3He + n \rightarrow ^1 H + ^3 H + 764keV \tag{2.2}$$

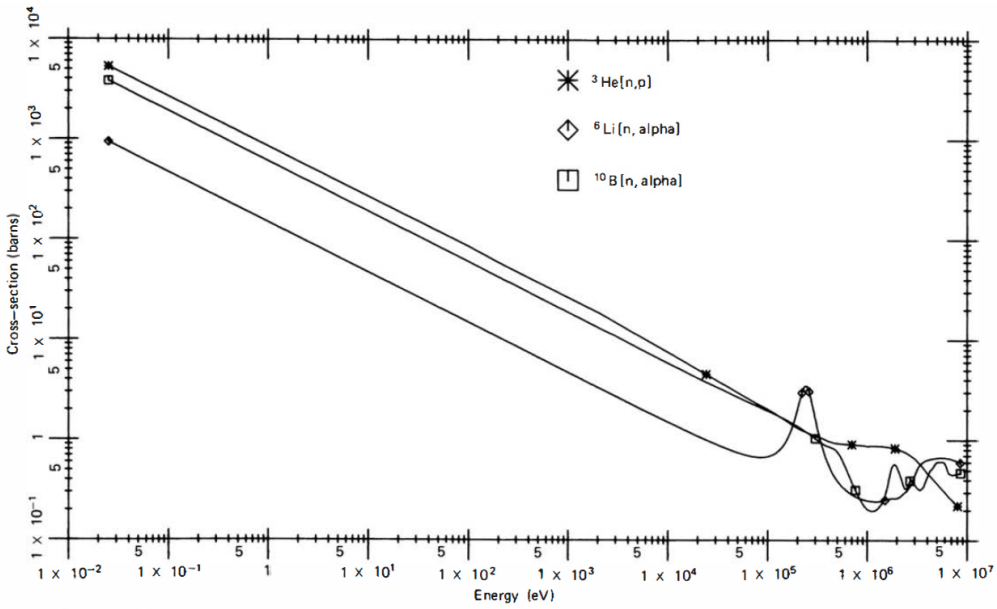

FIGURE 2.3: Cross sections versus neutron energy for some reactions of interest in neutron detection [2].

Typically an array of ^{3}He detectors surrounded by polyethylene moderation is used as a detector system in a subcritical neutron multiplication inference measurement. The ^{3}He multiplicity system primarily used by Los Alamos National Laboratory (LANL) is the NoMAD (Neutron Multiplicity ^{3}He Array Detectors), which is a slightly modified version of the state-of-the-art MC-15 neutron multiplicity counter [68] (itself a successor to the NPOD [69]) and is the current state-of-the-art detection system for obtaining list-mode data from highly multiplying systems for subcritical benchmark measurements. Each NoMAD detector consists of 15 ^{3}He tubes embedded in polyethylene. The thickness of moderator between each tube is optimized for detection efficiency. The slowing down time of a fast fission neutron entering the NoMAD is approximately 40 μs. The overall size and number of tubes contained in the detector system was chosen as a trade-off between increasing efficiency and decreasing portability. Every ^{3}He tube has a pressure of 150 psia (10.13 bars) and active dimensions of 0.97 $\times$ 15 in. (2.46 x 38.1 cm). The counter's fill gas is a mixture of ^{3}He with 2% CO_2 as a

quench gas (in atomic proportion). A removable cadmium shield can be placed on the front of the NoMAD to preferentially capture thermal neutrons if desired.

Representations of the NoMAD geometry, produced using the CAD software Solidworks® and the MCNP plotter, are shown in Figure 2.4

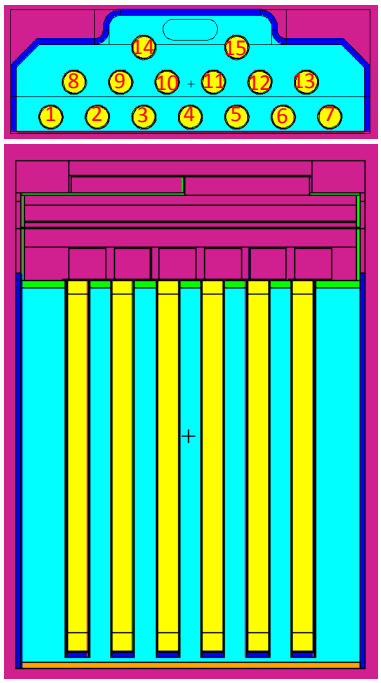

(a) MCNP plotter representation of the NoMAD geometry as seen from the top (upper image) and front (lower image)

(b) CAD representation of the NoMAD geometry

FIGURE 2.4: MCNP plotter and CAD representations of the NoMAD geometry.

2.4 List-mode data

Neutron multiplicity measurements using ^{3}He detector systems record list-mode data, which consists only of the time of neutron detection and the tube in which the detection occurred. For the LANL detector systems, the list-mode data is stored in a "LMX" file as binary data with a text header. The text header gives general information about the measurement and the structure of the binary data, as well as the meaning of non-event flags (clock rollover and end of data) in the binary data. The binary data consists of 8 byte events. The first 4 bytes give the channel information and the last 4 bytes give the time information. When converted properly, the channel data will be a list of 0s or 1s equal to the number of detector channels. If the value is 0, that specific detector did not get an event at that time. If the value is 1, that specific detector did get an event at that time. It is possible (but very unlikely for most systems) to have multiple detector channel values be 1 for the same time stamp. The time information is given in number of time steps since the start of the measurement and in order to get actual time, the time stamp needs to be multiplied by the clock tick length. A clock rollover occurs every time the time stamp reaches 2^{32} time steps. and the first event immediately following the clock rollover will be at 24 time steps. The end of binary data flag indicates the end of the file has been reached and there are no further events. Processing scripts have been developed specifically for this work that can perform useful tasks such as splitting a large LMX file into a number of smaller files, converting the LMX file into a text file of event times, calculating the count rate as a function of time, and removing all events outside a certain desired time window.

The list-mode data can be used for many different types of multiplicity analysis methods; for this work the data was analyzed with the both the Rossi-α method and the Hage-Cifarelli formalism based on the Feynman Variance-to-Mean method, but other methods have been discussed. Much of the following discussion is taken from the information presented in [28].

2.4.1 Rossi-α

In subcritical experiments using moderated ^{3}He detector systems, the neutron lifetime (the inverse of λ) is always bounded by a minimum value, no matter how fast the system is, due to the slowing down time of neutrons in the moderator. This minimum lifetime varies for different detector systems, and is approximately 40 μs for the NoMAD. As the neutron spectrum becomes more soft (due to reflection), the lifetime increases. The bare BeRP ball

has a leakage multiplication value of approximately 3.3, and a neutron lifetime of 43 μs. When 4 inches of HDPE reflection is added these values increase to 9.7 and 277 μs, respectively.

2.4.2 Feynman variance-to-mean

For this work the list-mode data are binned into Feynman histograms according to specified gate widths using the data processing tool Momentum [70]. The most commonly used units in this work for many of the variables presented in this section are listed in Table 2.1.

TABLE 2.1: Most commonly used units for many of the variables used in this work for correlated neutron detection, along with some sample values.

Variable	Units
τ	seconds (s)
$C_n(\tau)$	# of occurrences
$R_1(\tau)$	s^{-1}
$R_2(\tau)$	s^{-1}
λ	s^{-1}
ϵ	unitless
M_L	unitless

The gate width τ used in subcritical benchmark experiments involving the reflected BeRP ball is typically on the order of thousands of microseconds. This is because in order to accurately measure correlated fission neutrons, the gate width used in data processing must be larger than the neutron lifetime. As previously discussed, the neutron lifetime ($\frac{1}{\lambda}$) of these experiments can range from 40 to several hundreds of microseconds. A gate width of thousands of microseconds is therefore large enough to preserve the correlated nature of the measured events, but is still small enough that delayed fission neutrons (emitted on the order of milliseconds after the fission) can be considered part of the background signal. The uncertainties of the observables of interest do vary as a function of gate width but not in a straightforward manner. Many factors contribute to the choice of the value of τ for a specific experiment, as detailed in [71, 72].

2.5 Contributions of this thesis

The purpose of this work is to apply subcritical neutron multiplication inference measurements and simulations to validation of the nuclear data and computational methods currently used to predicatively model SNM experiments. SNM measurements and simulations are integral to nuclear nonproliferation and criticality safety, for applications such as SNM identification and characterization, experiment planning, detection system development, and many others. Predictive radiation transport codes and accurate nuclear data knowledge are necessary for precisely predicting the results of SNM measurements. This work applied subcritical neutron multiplication inference measurements and simulations to validation of the nuclear data and computational methods currently used to predictively model SNM experiments. The work includes a new state-of-the-art neutron multiplication inference benchmark, as well as a novel research reactor neutron multiplication inference measurement resulting in a protocol for future research reactor subcritical benchmarks. The state-of-the-art (SCRαP) subcritical neutron multiplication inference measurement that has been completed shows good comparison between simulated and measured results, and benchmark sensitivity and uncertainty analysis has been conducted. The advanced (CaSPER) subcritical neutron multiplication inference measurement has resulted in an established protocol for future research reactor subcritical neutron multiplication inference benchmarks and is paving the way for novel applications of such measurements to nuclear data and computational methods validation for nuclear nonproliferation and security applications. Several methods of applying subcritical neutron multiplication inference benchmarks to nuclear data and computational methods have been applied. A Bayesian optimization framework has been developed and applied for the first time to subcritical benchmark design. An improved FOM for Feynman histograms has been developed and validated. Various radiation codes that implement the correlated physics of fission have been applied to subcritical benchmarks in a new way, by comparing the performance of the different codes and investigating correlations between nuclear data and observables of interest using the Pearson correlation coefficient. Finally, a genetic algorithm framework has been developed and applied for the first time to nuclear data evaluation. The genetic algorithm is able to intelligently converge on a set of fission neutron multiplicity distribution parameters that yield improved performance of simulated results as compared to the measured benchmark results when applied to the subcritical neutron multiplication inference benchmarks. The genetic algorithm is a framework that can be used to make potential suggestions to nuclear data evaluators using subcritical and/or critical benchmark experiments.

Chapter 3

SCRαP Subcritical Neutron Multiplication Inference Measurement

As previously described, a subcritical benchmark measurement is a high-quality subcritical measurement in which all physical parameters and uncertainties are well characterized to a high degree of accuracy, and which is peer reviewed and compiled with other benchmark experiments into a database such as the ICSBEP handbook. Critical benchmarks are plentiful, but are not sensitive to correlated neutron parameters in the way that the handful of existing subcritical benchmarks are. This chapter and the next chapter of the work encompasses the entire process of an advanced subcritical measurement, from the earliest planning stages to the final analysis and comparison to simulated results. In this chapter the SCRαP measurement, a state-of-the-art subcritical benchmark measurement, is discussed. Additional information can be found in the ICSBEP submission and journal papers related to the SCRαP experiment [72, 73].

3.1 Introduction

Seventeen separate subcritical configurations were measured with an α-phase plutonium sphere reflected by copper and HDPE. These experiments took place at NCERC. Measurements included seventeen experimental configurations that consisted of a bare 4.5 kg alpha-phase plutonium sphere (BeRP ball), as well as the BERP ball surrounded by eight different copper thicknesses, seven different combined HDPE-copper thicknesses, and 1 HDPE-only configuration. The subcritical multiplication was inferred using correlated neutron data from the NoMAD detector system. The seventeen subcritical experimental configurations are considered acceptable as benchmark experiments by the ICSBEP working group, and the SCRαP evaluation will be published in the next version of the ICSBEP handbook.

3.2 Experiment

Seventeen subcritical configurations consisting of either the bare BeRP ball or the BeRP ball reflected by various thicknesses of copper and HDPE were measured. Table 3.1 summarizes the different configurations, and Figure 3.1 shows a representative measurement configuration. Each configuration consists of the BeRP ball reflected by between 0 and 8 0.5" thick shells of either copper or HDPE. Each orange box represents an approximately 0.5 inch thick copper shell, and every gray box represents an approximately 0.5 inch thick HDPE shell. The order from low to high number identifier was based on preliminary design simulations and chosen based on increasing multiplication factor (with configuration 0 having the lowest multiplication factor and configuration 15 having the highest multiplication factor). The one exception is configuration 16: the HDPE-only configuration was added based on additional time during experiment execution and for its predicted benefits.

TABLE 3.1: SCRαP benchmark configurations.

Configuration #	Layer number (each layer is 0.5 inches thick)							
	1	2	3	4	5	6	7	8
0								
1								
2								
3								
4								
5								
6								
7								
8								
9								
10								
11								
12								
13								
14								
15								
16								

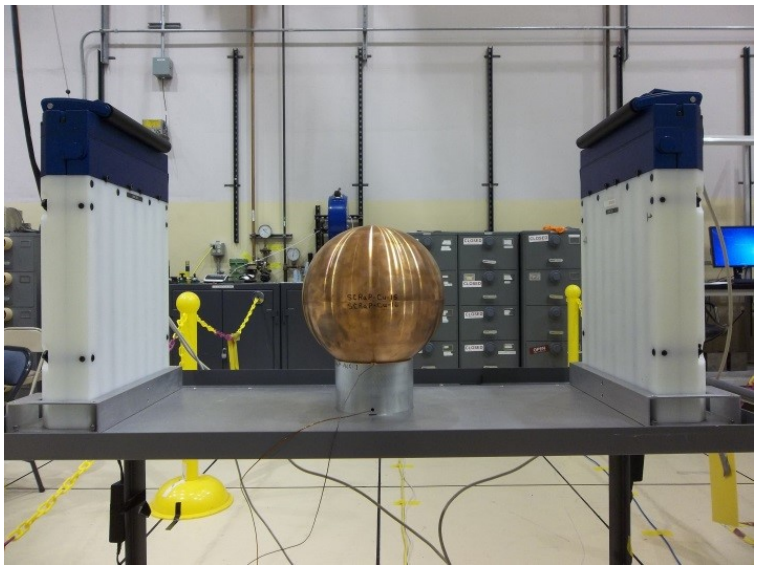

FIGURE 3.1: Representative SCRαP measurement configuration geometry.

For all configurations, an aluminum stand was used. The stands used are specific to the reflector thickness, so as to maintain the same BeRP ball height throughout the experiment. The aluminum stands sit in an indent on the base plate which centers it on the base plate. The detectors were placed in aluminum-holders, which were connected to the base plate and held the detectors in the center of the edges of the base plate at all times. The base plate, base plate adaptors, and detectors were all placed on a carbon steel cart. Two NoMAD neutron detectors were used for the subcritical measurements. These detectors are located on the same cart as the BERP ball. Overviews of the entire experimental setup for the 4-in.-thick copper reflector configuration are shown in Figure 3.2.

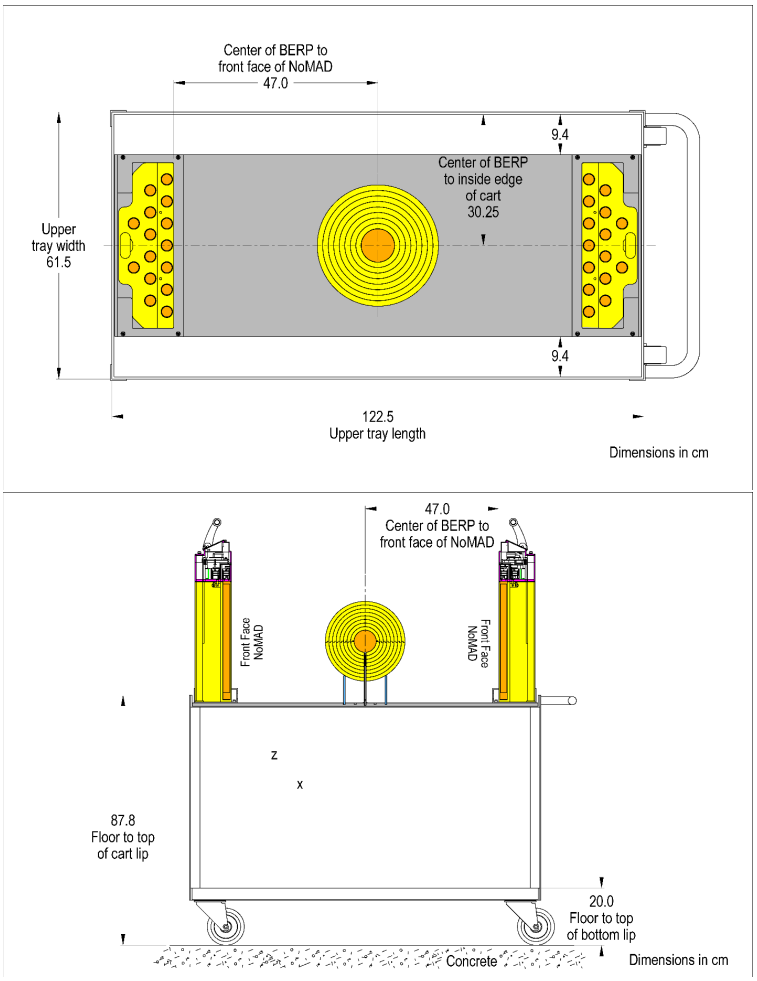

FIGURE 3.2: Overviews of the entire experimental setup as seen from above and from the side.

3.3 Simulations

The detailed benchmark MCNP model includes a detailed description of all elements present in the plutonium sphere's nearby environment, and the concrete in the building. All dimensions are extracted from engineering drawings, measurements from the manufacturer and/or measurements performed during the experiment. Some of the dimensions have been intentionally varied slightly since the actual dimensions measured do not represent physical realities. All of the material definitions in the models are based on very detailed isotopics and impurities reports. Known impurities are retained in the compositions of all materials present. Figures 3.3-3.5 show the geometry of the detailed model for configuration 15.

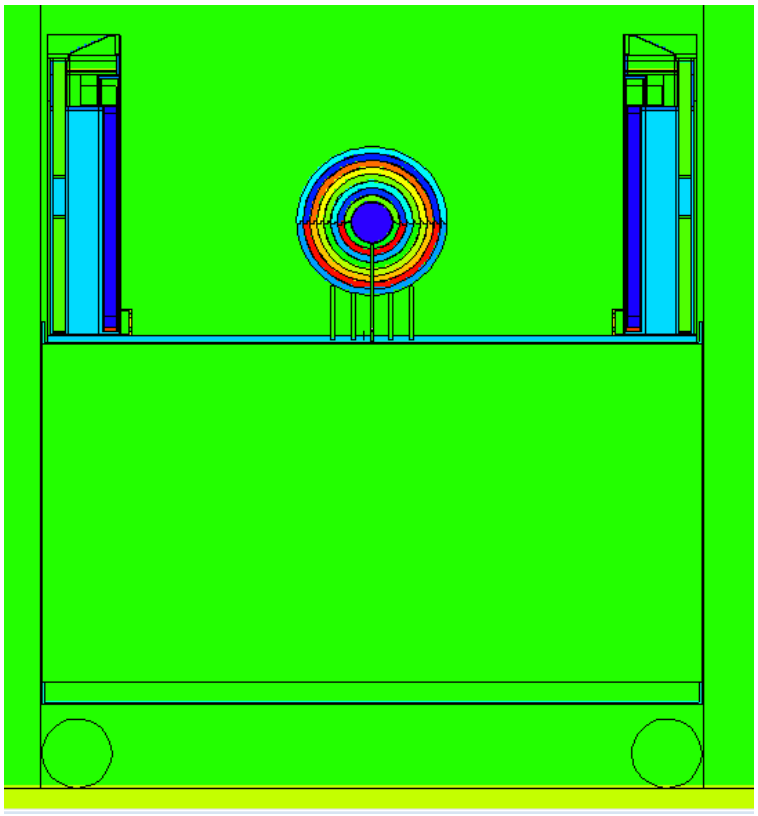

FIGURE 3.3: Detailed MCNP model of configuration 15.

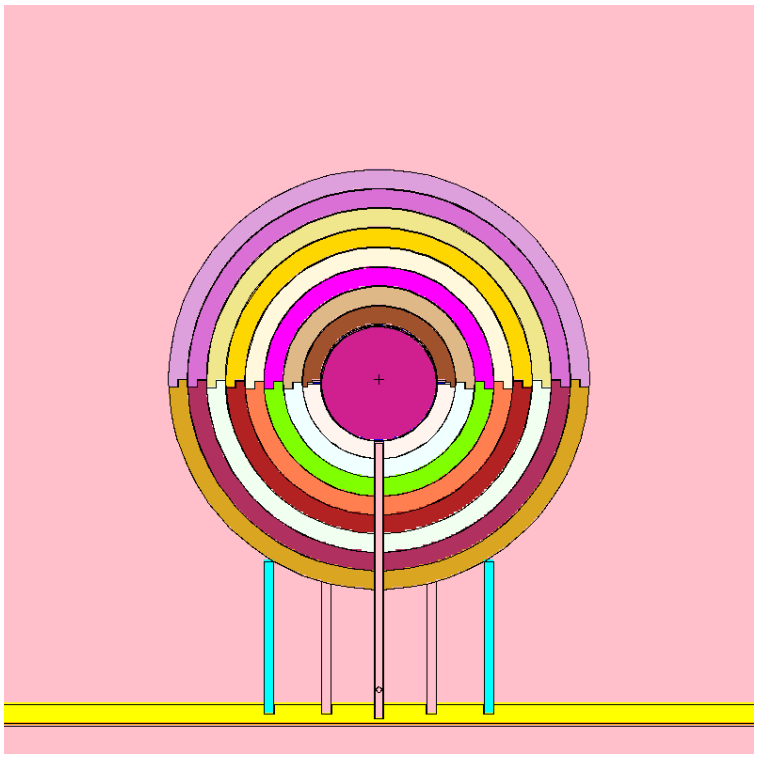

FIGURE 3.4: Detailed MCNP model of configuration 15, focused on the reflected BeRP ball.

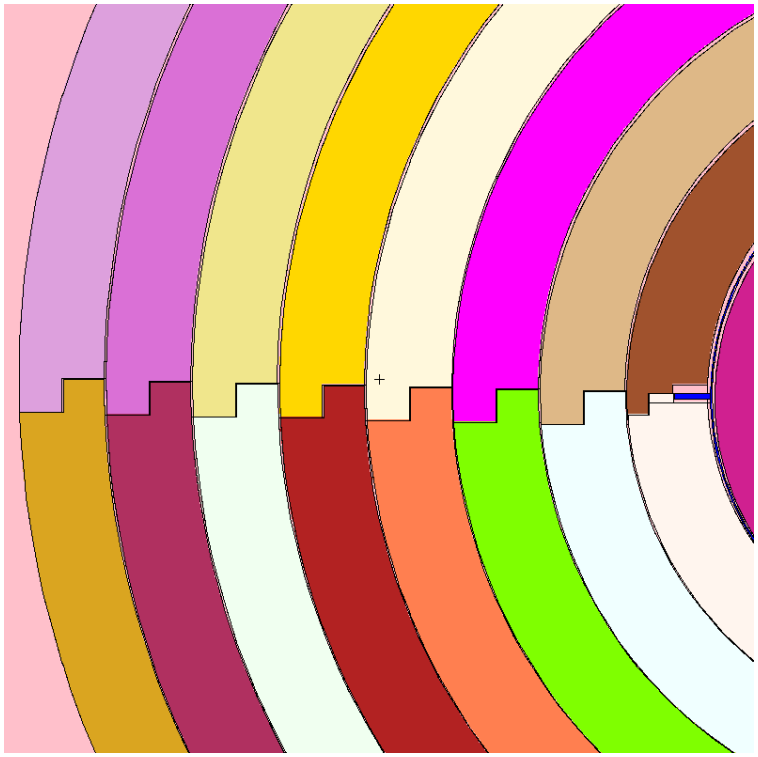

FIGURE 3.5: Detailed MCNP model of configuration 15, focused on the reflector hemishells.

In order to accurately model the correlated physics of fission in the benchmark model, MCNP FMULT cards were used. Table 3.2 lists the various options that were specified in the model. These same options were also used for both previous subcritical benchmark experiments, namely the BeRP-Ni and BeRP-W experiments. This combination of options is generally recommended by the code developers because it best matches the nuclear data. It ensures that MCNP is using the Lestone data and method as it was implemented in MCNP5.

TABLE 3.2: MCNP FMULT card options used for benchmark model.

Option	Value	Meaning
METHOD	0	MCNP5 sine/cosine sampling method
DATA	1	Lestone widths for fission multiplicity distributions
SHIFT	0	Rounds sampled number of neutrons to the nearest integer.

Measured and simulated singles rate R_1, doubles rate R_2, and leakage multiplication M_L results are plotted for all configurations in Figure 3.6. All 3 observables of interest show good agreement between simulated and measured data.

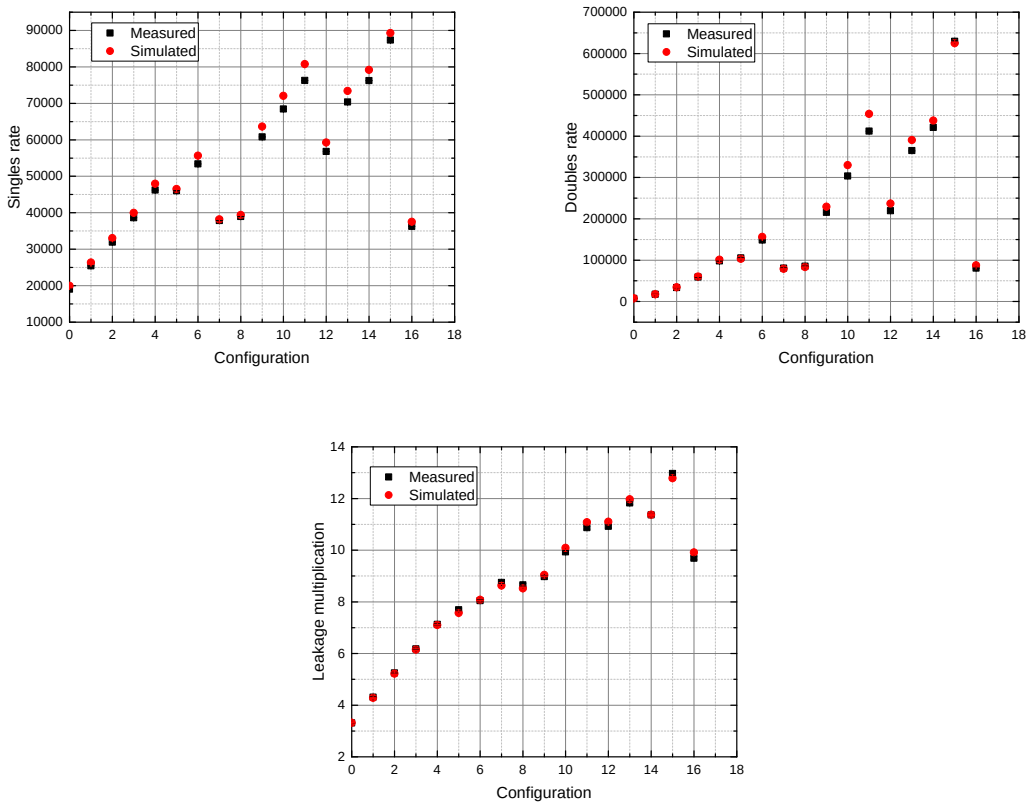

FIGURE 3.6: Measured and simulated singles rate R_1, doubles rate R_2, and leakage multiplication M_L results. All error bars are smaller than the datum point markers.

3.4 Uncertainty analysis

In addition to quantifying all statistical uncertainties, the benchmark also quantifies the effects of all systematic uncertainties on measured quantities. The uncertainties have been divided into five categories: mass measurements, dimensions, positioning, compositions, and description of the NoMAD. The first category includes the material mass uncertainties for the plutonium sphere, the plutonium sphere cladding, the aluminum stand, the aluminum tube, the aluminum base plate, and each copper and polyethylene element. The second category

includes the uncertainties in the geometry of the different components. This category includes the radii of the plutonium sphere, the thickness of the plutonium sphere cladding, each copper and polyethylene layer, the aluminum stand height, the aluminum tube height, and the concrete. Temperature effects which lead to a change in the plutonium sphere dimensions are also included. The third category looks at the uncertainties in the positioning of each subassembly present in the experimental configuration. This category includes the position of the BERP ball (i.e. the full setup) inside the room. It further includes the horizontal (left/right and forward/back) positions of each NoMAD on the base plate, the left/right position of the base plate on the cart, and the aluminum stand and aluminum tube position relative to the two NoMADs. Uncertainties related to the gaps in the copper and polyethylene hemishells are also evaluated in this category. The fourth category includes the uncertainties in the compositions of each material: the α-phase plutonium, the SS-304 (cladding), the copper and polyethylene (reflector elements), the aluminum 6061 (stands, tube and base plate), the aluminum 6063 used for the base plate adaptors, and the concrete (walls and floor). The relative humidity of air in the measurement room, as well as the density/ pressure of the air, is investigated. The effect of additional elements such as the thermocouples are also discussed. The fifth category looks at the uncertainties related to the description of the NoMADs: the ^{3}He tubes composition, length and position; the NoMAD polyethylene body composition and mass; and the surrounding elements.

Tables 3.3 and 3.4 list the effect of the individual uncertainties on the measured quantities for configuration 15, which is an overestimating case because it has the largest multiplication factor. The resulting uncertainties on observables of interest were obtained by using the central difference method to vary each measured quantity. Typically a perturbation of +5 and -5 times the uncertainty was used. The total uncertainty on configuration 15 can be obtained by taking the quadratic sum of all uncorrelated individual standard deviations.

TABLE 3.3: Individual uncertainties on measured quantities for configuration 15.

Source of Uncertainty	R_1 uncertainty (cts/sec)	R_2 uncertainty (cts/sec)	M_L uncertainty
Al Adaptor mass	0.00	0.00	0.000
Al stand mass	0.00	0.00	0.000
Al base plate mass	2.03	133.96	0.002
SS304 cladding mass	0.00	0.00	0.000
Presence of screws	0.00	0.00	0.000
Plutonium sphere mass	21.08	830.78	0.010
Copper reflector mass	102.81	1965.02	0.000
Polyethylene reflector mass	134.40	2916.77	0.017
SS-304 cladding thickness	0.00	0.00	0.000
Concrete thickness	0.00	0.00	0.000
Copper shell thickness	42.66	1557.32	0.017
Polyethylene shell thickness	28.43	981.16	0.000
Plutonium sphere radius	652.43	14263.85	0.088
Temperature Variations	602.34	12830.36	0.071
Plutonium sphere radius (includes both tolerance and temperature variation)	1349.12	30894.12	0.173
Al stand height	0.00	0.00	0.000
Al tube height	10.55	0.00	0.000
Al base plate (position on the table widthwise)	0.00	0.00	0.000
BERP Position inside room lengthwise	0.00	0.00	0.000
BERP Position inside room widthwise	0.00	0.00	0.000
Reflector Shell Gaps	0.00	0.00	0.000

TABLE 3.4: Individual uncertainties on measured quantities for configuration 15.

Source of Uncertainty	R_1 uncertainty (cts/sec)	R_2 uncertainty (cts/sec)	M_L uncertainty
NoMAD (distance from BERP ball lengthwise)	0.00	0.00	0.000
Density of air	11.89	0.00	0.000
Baseplate impurities	0.00	0.00	0.000
SS-304 cladding impurities	0.00	0.00	0.000
Composition of concrete	224.48	5944.91	0.054
Copper impurities: all impurities removed	107.24	2824.39	0.000
Polyethylene impurities: all impurities removed	2091.82	45782.18	0.280
Plutonium assay	11.76	0.00	0.010
Pu impurities	72.37	0.00	0.000
$^{239}Pu/^{240}Pu$ isotopic content	11.59	15.14	0.001
Stand impurities	0.00	0.00	0.000
Presence of Ta and W in Pu alloy	3314.46	71063.02	0.343
Active region length	236.99	3198.59	0.000
Active region position	406.23	15411.92	0.188
CO_2	60.53	0.00	0.000
Dead Time	466.62	16143.14	0.186
^3He gas pressure	238.75	3167.04	0.000
NoMAD back poly mass	11.41	582.49	0.000
NoMAD front poly mass	14.63	696.43	0.016

Tables 3.5-3.8 show simulation results for various nuclear data libraries and fission event generators, as compared to the measured benchmark results.

TABLE 3.5: Simulation Results (MCNP6 - Detailed Model)- ENDF/B-VII.1.

Case	R_1 (cts/s)	σ	(C-E)/E (%)	R_2 (cts/s)	σ	(C-E)/E (%)	M_L	σ	(C-E)/E (%)
0	19695.42	7.58	3.35	7549.43	47.26	3.72	3.40	0.02	2.67
1	26039.94	10.03	2.29	17495.46	84.40	1.13	4.33	0.02	0.52
2	32622.70	12.86	2.17	33940.82	141.18	0.65	5.23	0.02	-0.36
3	39431.30	16.13	2.07	59502.05	225.72	0.95	6.17	0.02	-0.13
4	47352.32	20.15	2.45	100064.26	359.07	1.99	7.11	0.02	-0.29
5	45926.25	19.82	-0.22	98330.29	362.47	-6.78	7.40	0.03	-3.75
6	54962.94	24.43	2.98	154601.63	542.53	4.09	8.07	0.03	0.32
7	37706.83	17.74	-0.40	77676.17	290.23	-3.92	8.58	0.03	-1.94
8	38888.21	18.16	-0.14	81878.41	302.51	-4.11	8.51	0.03	-1.74
9	62861.33	29.14	3.42	227788.00	776.43	5.66	9.02	0.03	0.56
10	71185.21	34.29	4.00	323447.20	1093.99	6.51	9.94	0.03	0.01
11	79781.64	39.86	4.58	445204.96	1487.20	8.02	10.84	0.04	-0.32
12	58537.40	29.03	3.09	233414.36	822.28	6.35	10.57	0.04	-3.24
13	72455.37	36.96	2.99	385405.33	1325.24	5.62	11.35	0.04	-4.03
14	78204.10	39.27	2.60	431911.67	1456.48	2.55	10.94	0.04	-3.77
15	88097.46	46.55	0.87	618173.85	2080.45	-1.78	12.27	0.04	-5.42
16	36990.82	17.58	1.97	80976.63	334.92	0.54	9.25	0.04	-4.50

TABLE 3.6: Simulation Results (MCNP6 - Detailed Model)- ENDF/B-VII.1 with FREYA.

Case	R_1 (cts/s)	σ	(C-E)/E (%)	R_2 (cts/s)	σ	(C-E)/E (%)	M_L	σ	(C-E)/E (%)
0	20194.45	7.63	5.97	7504.69	47.87	3.11	3.24	0.02	-2.05
1	26579.49	10.03	4.41	17252.60	84.00	-0.27	4.13	0.02	-4.20
2	33122.27	12.76	3.73	32959.93	138.34	-2.26	4.96	0.02	-5.54
3	39865.95	15.83	3.20	56318.90	216.50	-4.45	5.75	0.02	-6.89
4	47536.22	19.60	2.85	93279.77	336.69	-4.93	6.61	0.02	-7.21
5	45777.77	19.10	-0.54	89714.94	331.52	-14.95	6.84	0.02	-11.05
6	54802.83	23.44	2.68	140184.73	490.00	-5.62	7.41	0.02	-7.92
7	37343.75	16.95	-1.36	69445.19	260.08	-14.10	7.87	0.03	-10.08
8	38509.22	17.43	-1.12	73976.63	275.76	-13.36	7.88	0.03	-8.98
9	62415.23	27.76	2.69	203820.29	693.99	-5.46	8.24	0.03	-8.18
10	70220.65	32.48	2.59	286791.08	968.40	-5.56	9.10	0.03	-8.40
11	78241.50	37.49	2.56	390022.92	1302.08	-5.37	9.92	0.03	-8.77
12	57702.05	27.52	1.62	206818.80	726.22	-5.77	9.68	0.03	-11.34
13	71292.63	34.86	1.34	339190.92	1156.27	-7.05	10.36	0.03	-12.35
14	76213.62	36.82	-0.01	375955.63	1262.80	-10.74	10.07	0.03	-11.41
15	85479.30	43.18	-2.12	527007.75	1766.00	-16.27	11.16	0.04	-13.96
16	36551.31	16.83	0.76	72651.76	303.44	-9.80	8.54	0.03	-11.80

TABLE 3.7: Simulation Results (MCNP6 - Detailed Model)- ENDF/B-VIII.

Case	R_1 (cts/s)	σ	(C-E)/E (%)	R_2 (cts/s)	σ	(C-E)/E (%)	M_L	σ	(C-E)/E (%)
0	20206.17	7.65	6.03	7609.01	47.87	4.54	3.28	0.02	-1.01
1	26566.56	9.99	4.36	17000.37	83.20	-1.73	4.08	0.02	-5.34
2	32971.04	12.66	3.26	32207.04	135.87	-4.49	4.90	0.02	-6.71
3	39483.15	15.56	2.20	53962.68	208.02	-8.45	5.63	0.02	-8.85
4	46812.63	19.08	1.28	87442.31	317.06	-10.88	6.41	0.02	-10.06
5	45341.81	19.38	-1.49	93302.73	344.15	-11.55	7.22	0.03	-6.12
6	53547.56	22.53	0.33	128038.05	449.99	-13.80	7.11	0.02	-11.63
7	37636.04	17.54	-0.58	75492.95	281.93	-6.62	8.38	0.03	-4.19
8	38405.81	17.30	-1.38	72637.51	269.09	-14.93	7.79	0.03	-10.07
9	60418.60	26.38	-0.60	182125.03	623.28	-15.52	7.88	0.03	-12.16
10	67364.26	30.32	-1.59	246924.21	831.43	-18.69	8.55	0.03	-13.96
11	74375.98	34.54	-2.51	327024.12	1085.32	-20.66	9.24	0.03	-14.99
12	58721.09	27.86	3.41	212148.84	737.48	-3.34	9.60	0.03	-12.14
13	71205.96	34.38	1.22	328683.50	1131.77	-9.93	10.08	0.03	-14.73
14	74208.35	34.88	-2.64	334398.30	1121.30	-20.61	9.48	0.03	-16.60
15	82460.01	40.20	-5.58	452397.69	1503.97	-28.12	10.33	0.03	-20.32
16	37049.11	17.10	2.13	75458.29	311.84	-6.32	8.63	0.03	-10.89

TABLE 3.8: Simulation Results (MCNP6 - Detailed Model)- ENDF/B-VIII with FREYA.

Case	R_1 (cts/s)	σ	(C-E)/E (%)	R_2 (cts/s)	σ	(C-E)/E (%)	M_L	σ	(C-E)/E (%)
0	20206.17	7.65	6.03	7609.01	47.87	4.54	3.28	0.02	-1.01
1	26566.56	9.99	4.36	17000.37	83.20	-1.73	4.08	0.02	-5.34
2	32971.04	12.66	3.26	32207.04	135.87	-4.49	4.90	0.02	-6.71
3	39483.15	15.56	2.20	53962.68	208.02	-8.45	5.63	0.02	-8.85
4	46812.63	19.08	1.28	87442.31	317.06	-10.88	6.41	0.02	-10.06
5	45610.27	18.94	-0.91	87869.39	322.46	-16.70	6.75	0.02	-12.14
6	53547.56	22.53	0.33	128038.05	449.99	-13.80	7.11	0.02	-11.63
7	37729.08	17.09	-0.34	70696.80	262.28	-12.55	7.85	0.03	-10.30
8	38405.81	17.30	-1.38	72637.51	269.09	-14.93	7.79	0.03	-10.07
9	60418.60	26.38	-0.60	182125.03	623.28	-15.52	7.88	0.03	-12.16
10	67364.26	30.32	-1.59	246924.21	831.43	-18.69	8.55	0.03	-13.96
11	74375.98	34.54	-2.51	327024.12	1085.32	-20.66	9.24	0.03	-14.99
12	58721.09	27.86	3.41	212148.84	737.48	-3.34	9.60	0.03	-12.14
13	71205.96	34.38	1.22	328683.50	1131.77	-9.93	10.08	0.03	-14.73
14	74208.35	34.88	-2.64	334398.30	1121.30	-20.61	9.48	0.03	-16.60
15	82460.01	40.20	-5.58	452397.69	1503.97	-28.12	10.33	0.03	-20.32
16	37049.11	17.10	2.13	75458.29	311.84	-6.32	8.63	0.03	-10.89

Figures 3.7-3.9 display the data from Tables 3.5-3.8 in plot form, graphically comparing the simulation results for various nuclear data libraries and fission event generators to the measured benchmark results.

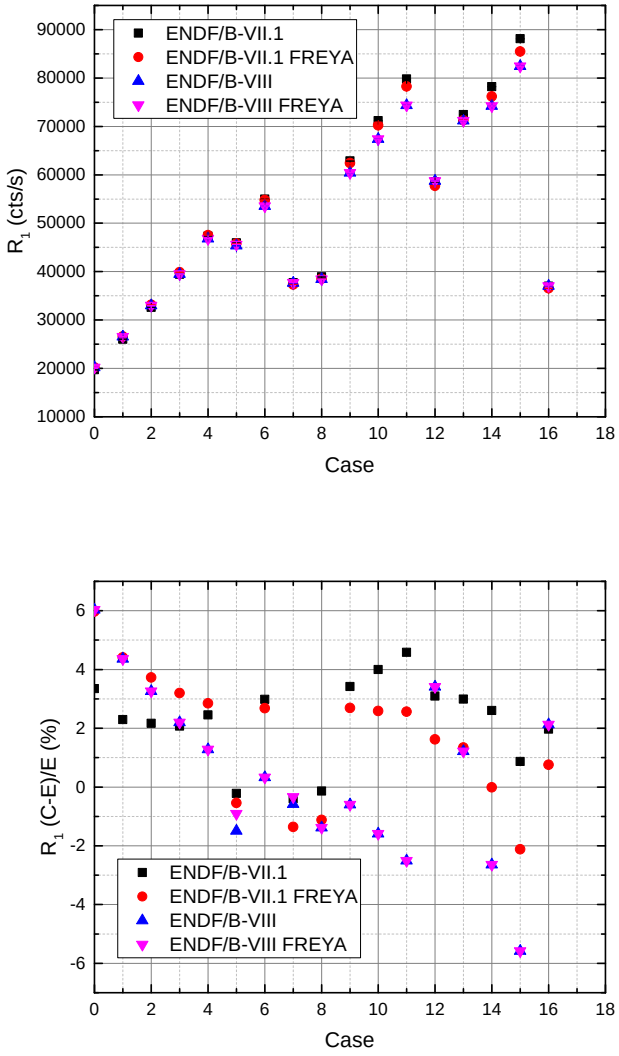

FIGURE 3.7: Singles (R_1) results when simulated with ENDF/B-VII.1, ENDF/B-VII.1 with FREYA, ENDF/B-VIII, and ENDF/B-VIII with FREYA. (C-E)/E values are also included.

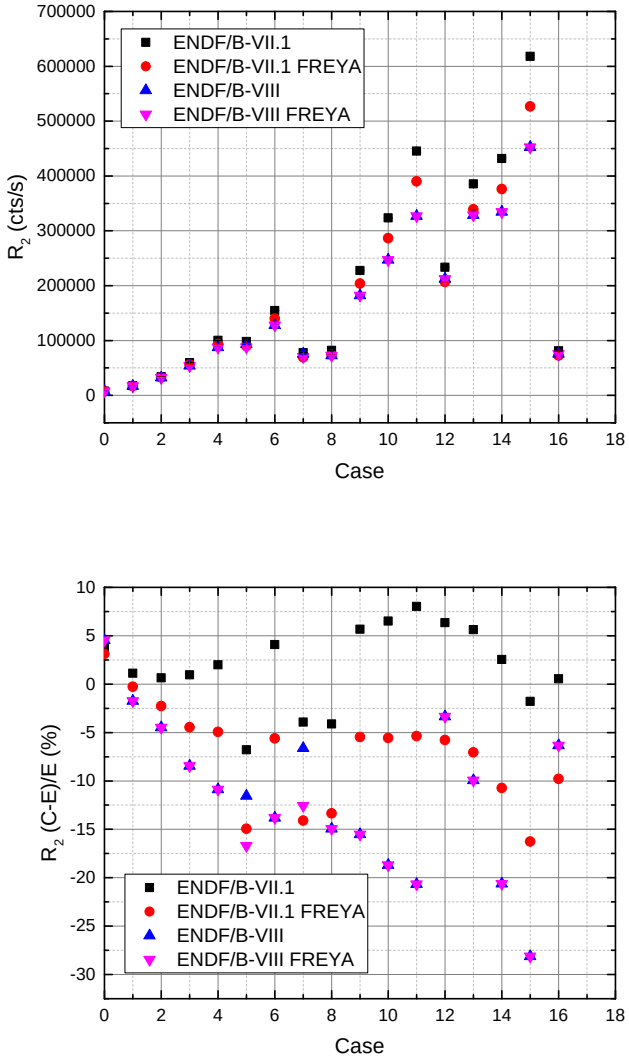

FIGURE 3.8: Doubles (R_2) results when simulated with ENDF/B-VII.1, ENDF/B-VII.1 with FREYA, ENDF/B-VIII, and ENDF/B-VIII with FREYA. (C-E)/E values are also included.

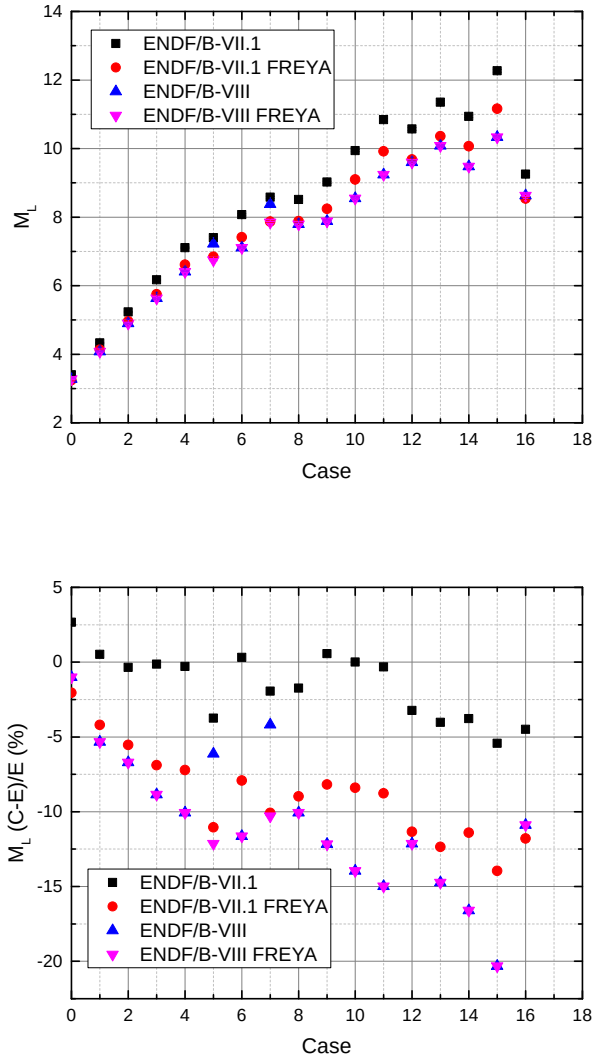

FIGURE 3.9: Leakage multiplication (M_L) results when simulated with ENDF/B-VII.1, ENDF/B-VII.1 with FREYA, ENDF/B-VIII, and ENDF/B-VIII with FREYA. (C-E)/E values are also included.

Chapter 4

CaSPER Subcritical Neutron Multiplication Inference Measurement

In this chapter the Critical and Subcritical 0-Power Experiment at Rensselaer (CaSPER) measurement, a novel advanced subcritical measurement, is discussed. The discussion is based off the conference proceeding and journal paper related to the CaSPER experiment [74, 75].

4.1 Introduction

The Critical and Subcritical 0-Power Experiment at Rensselaer (CaSPER) measurement campaign was designed to establish a protocol for neutron multiplicity measurements on research reactors as the next step in advanced subcritical neutron multiplication inference measurements. Such measurements can help identify deficiencies and quantify uncertainties in nuclear data, as well as validate predictive radiation transport simulation capabilities related to subcritical neutron multiplication inference techniques. CaSPER includes integral experimental configurations at different achieved reactivity states which have been measured at the Walthousen Reactor Critical Facility (RCF) [76] at Rensselaer Polytechnic Institute (RPI). The RCF achieves different reactivity states by varying the control rod (CR) and water height in the reactor core. It is a benefit that the system is able to reach a wide range of multiplication states, by using both fine and coarse reactivity control in the form of CR and water height, respectively. It is also useful to know the possible reactivity states ahead of time, through the use of reactivity worth curves. The diversity of the CaSPER configurations are unique in contrast to previous subcritical benchmark measurements in that they are the first neutron multiplication inference measurements on a zero-power pool-type reactor which offers spatial complexity, different materials (fuel, moderator, CR material, etc.), and system-specific neutron cross-section sensitivities (various energy ranges and neutron reaction contributions).

4.2 Advancing state-of-the-art using a 0-power reactor

Nominally, a 0-power reactor is the ideal type of pool-type reactor for conducting neutron multiplicity measurements. A substantial benefit of a 0-power reactor is the ability to directly adjust fuel rod arrangement as desired. The detector system can be placed in close proximity to the core without the disadvantage of possible radiation damage to the detector system electronics or materials. Additionally, the detector system is much less likely to be overwhelmed in the relatively lower neutron flux of a 0-power reactor. Due to the absence of noticeable burn-up, the fuel inside a 0-power reactor is typically very well characterized as compared to fuel from reactors with significant burn-up. The fuel rods also do not become distorted (i.e. cracking, swelling, or melting) from burn-up while residing in a 0-power reactor (distortion occurs when the heat from fission reactions causes the fuel to melt and fuse into distorted geometries). In addition to changing the fuel composition and geometry, the high burn-up of some research reactors can preclude entering the core for direct manipulation of experiment equipment. Due to the buildup of fission products, the gamma ray flux inside the reactor core can become quite significant. Although ^{3}He tubes are relatively insensitive to gamma rays, a large flux may significantly increase the noise signal even in ^{3}He detectors [77]. Specific to a 0-power pin-type reactor, the symmetry of typical fuel rod arrangement (rather than the fuel plates used within some reactors) is beneficial to neutron multiplicity measurements. A 0-power reactor best matches the criterion in neutron multiplicity measurements of understanding the dimensions and components of the system to be measured as well as possible.

4.3 Experiment design

The CaSPER measurements at the RPI-RCF were designed to include distinct configurations at various reactivity states ranging from subcritical to above delayed critical. Nine different configurations were achieved by varying the control rod and water height in the reactor core. The RCF core has low-enriched uranium (LEU) fuel in the form of SPERT-type F-1 fuel pins at an enrichment level of 4.81% U-235 by weight [76]. Fuel pins are encased in stainless steel cladding and boron-impregnated iron rods serve as CR's. When the tank is filled, the water serves as a moderator. The water tank containing the core is large enough to accommodate a sizable detector system(s), including the standard LANL ^{3}He portable neutron multiplicity detector systems which were retrofitted for water submersion.

The detector system used in CaSPER is the NOMAD. Because the neutrons inside a water-

moderated reactor are predominantly thermal, the removable cadmium shield was not utilized for the CaSPER measurements. In order to protect the NoMAD during submersion under water and to hold it in place, $\frac{1}{16}$in. thick aluminum housing and ratchet straps were used.

A photograph from the measurement campaign is shown in Figure 4.1. This photo shows 2 NoMAD systems, although only a single system was used for these measurements. In addition, the aluminum housing and ratchet straps are not shown. The distance between the ^{252}Cf source, located at the center of the core in place of the center fuel pin, and the NoMAD is 48.5 cm. The vertical center of the NoMAD is level with the vertical center of the core. The ^{252}Cf source information is given in Table 4.1. Both the initial assay activity and the calculated activity at the time of the CaSPER campaign are shown.

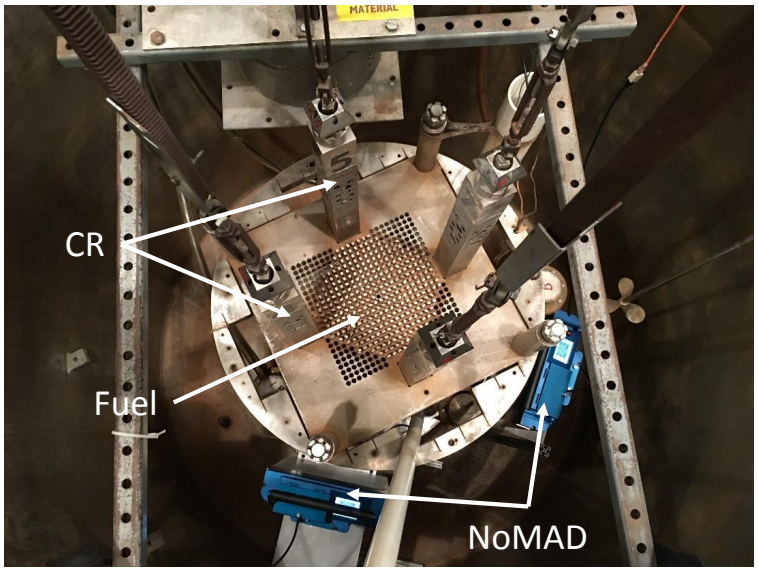

FIGURE 4.1: Photograph of the CaSPER measurement campaign at the RPI-RCF with the water drained from the core tank.

TABLE 4.1: ^{252}Cf source information.

Date	6/1/2006	7/25/2016
Activity (Bq)	1.54E7 (+/- 5.6%)	1.07E6
Strength (n/s)	1.79E6	1.25E5

During the design phase of the experiment, the MCNP model did not include the RCF PuBe source in its above-core shielding, as it was expected that its contribution would be negligible. Simulations were run with different ^{252}Cf source-detector distances, source strengths, and water and CR heights, with the goal of optimizing both the detector system count rates and the goodness of the doubles fits (quantified by the χ^2 value). The optimum count rate was considered to be between 1E3 and 1E5 s^{-1}, which represents a balance between the need for good statistical uncertainties and detector limitations. Based on these criteria it was determined that the optimized CaSPER configuration consisted of the NoMAD detector system at a distance of 35 cm from the center of the RCF core, with the ^{252}Cf source replacing the center fuel pin, and varying water and CR heights. However, the layout of the RCF core added some physical restrictions, and the NoMAD distance was changed to 48.5 cm. A parametric study was conducted to determine if the RPI-RCF water tank size would allow for placement of the NoMAD outside of the tank. The position of the NoMAD in the CaSPER MCNP model, at a water height of 67 in. and control rods fully withdrawn, was changed from inside the reactor core tank, to just outside the tank. The tank radius in the MCNP model was then set to be 30, 40, and 50 cm, while keeping the NoMAD position to be just outside the tank. Count rates were obtained at these distances and an exponential fit was used to extrapolate the data out to a tank radius of 100 cm. Extrapolation of a fit was used to generate the data at 60-100 cm because of the extensive computation time that would have been required to obtain simulated data at those tank radii. Equation 4.1 shows the exponential fit, and all results are listed in Table 4.2. An exponential fit was used both because exponential attenuation of neutrons in the water is expected to outweigh the reduction in flux due to the $\frac{1}{distance^2}$ reduction in solid angle, and because an exponential fit followed the data trend well.

$$y = 8 \times 10^7 e^{-0.185x} \tag{4.1}$$

TABLE 4.2: NoMAD count rate as a function of reactor core tank radius. The date for radii of 30-50 cm are from simulations, while the data for radii of 60-100 cm are from the extrapolated fit of the simulated data.

Tank radius (cm)	Singles rate (s^{-1})
30	3.27E+05
40	4.33E+04
50	8.13E+03
60	1.21E+03
70	1.90E+02
80	2.99E+01
90	4.70E+00
100	7.39E-01

Because the results of the parametric study indicate that the RCF water tank is too large for a high enough neutron signal to be obtained from outside of the tank, this detector system placement was not investigated further. The final experiment design included Monte Carlo simulations of the full system: neutron multiplicity detector, ^{252}Cf source which was included to increase the number of fissions and associated count rate for statistical adequacy, the PuBe starter source that is always located in a shielding container above the core, and the reactor configuration (fuel/rods/water). Ratchet straps were not included in the model because it was assumed they would have negligible impact on the observables of interest. The standard simulation model is shown in Figure 4.2. The PuBe source spectrum used in the model was taken from Anderson and Neff [78].

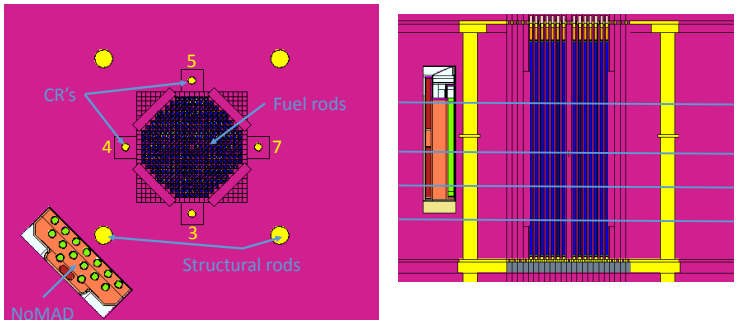

FIGURE 4.2: MCNP plotter representation of the CaSPER geometry as seen from above and the side. The ^{252}Cf source is located in the center of the fuel region and the CR numbers are shown. The light blue lines show the water level in relation to the NoMAD at 24, 30, 36, and 44 inch water heights.

4.4 Experiment execution

The RCF core configuration at the time of the CaSPER experiment was an octagonal lattice of 332 fuel pins, separated by a pitch of 1.63 cm. The center 333$^{\text{rd}}$ fuel pin was removed and the ^{252}Cf source was put in its place. The CR height can vary from 0 in., full insertion, to 36 in., full removal. During reactor operations in which the CR height is above 0 in., the water height is allowed vary between 19.5 in. and 67 in. The equipment used in the measurements includes the NoMAD detector, along with the aluminum housing and aluminum stands used to keep the detector water tight and in position within the tank, as well as lead bricks strapped to the bottom of the NoMAD housing to prevent flotation. A summary of the completed measurement configurations, excluding efficiency measurements, is presented in Table 4.3. The completed efficiency measurements, the purpose of which are to calculate absolute detector efficiency by taking the ratio of the detected count rate to the ^{252}Cf source strength in a non-multiplying system, are identical to the configurations listed in Table 4.3 but with all of the fuel pins removed from the core.

TABLE 4.3: Completed measurement configurations.

Configuration #	Water height	CR3 height	CR4 height	CR5 height	CR7 height	Intended reactivity
1	24 in.	36 in.	36 in.	36 in.	36 in.	-
2	30 in.	36 in.	36 in.	36 in.	36 in.	-
3	36 in.	36 in.	36 in.	36 in.	36 in.	-
4	44 in.	36 in.	36 in.	36 in.	36 in.	-
5	67 in.	0 in.	0 in.	0 in.	0 in.	-
6	67 in.	16 in.	16 in.	16 in.	16 in.	-$1.00
7	67 in.	20 in.	20 in.	20 in.	20 in.	-$0.50
8	67 in.	25 in.	25 in.	25 in.	25 in.	Delayed critical
9	67 in.	36 in.	36 in.	21 in.	21 in.	Delayed critical

Using the method presented in Equations 1.8-1.16, efficiency is required to calculate leakage multiplication. Ideally efficiency would have been calculated from the no-fuel "efficiency measurements" in which no fission is occurring and therefore the true absolute efficiency is measured. However, due to the large contribution of the above-core RCF PuBe starter source to the measured signal, this method is no longer valid. Several different possible methods were investigated and rejected, including taking a measurement of the CaSPER ^{252}Cf source at a 48.5 cm source-detector distance (the same distance as in the actual CaSPER measurements) to determine efficiency, and defining the ratio of the singles rate with fuel to the rate without fuel as M_L. The method that was chosen is explained in Appendix B.

4.5 Results

The measured data are a novel set of subcritical neutron multiplicity data that involves new and more complex spatial, material, and energy regimes. Normalized count rates per detector tube are plotted in Figures 4.3 and 4.4 for each completed measurement configuration. These data show the normalized count rate observed in each of the 15 ^{3}He tubes that make up the NoMAD detection system. Simulated results are also plotted for comparison, and figure of merit (FOM) values quantifying the deviations are listed in Table 4.4. The values are calculated according to Equation 4.2 [79]. In Equation 4.2, N represents the total number of bins in the histogram. S_i and E_i are the values of the i^{th} normalized bins in the simulated and experimental data, respectively. The variances of the i^{th} bins in the simulated and

experimental data are represented by $\sigma^2(S_i)$ and $\sigma^2(E_i)$, respectively. The ideal FOM value is 1, representing a deviation between simulated and experimental histogram results that is equal to the combined uncertainties.

$$FOM = \frac{1}{N_{bins}} \sum_{i=1}^{N_{bins}} \frac{(S_i - E_i)^2}{\sigma^2(S_i) + \sigma^2(E_i)} \tag{4.2}$$

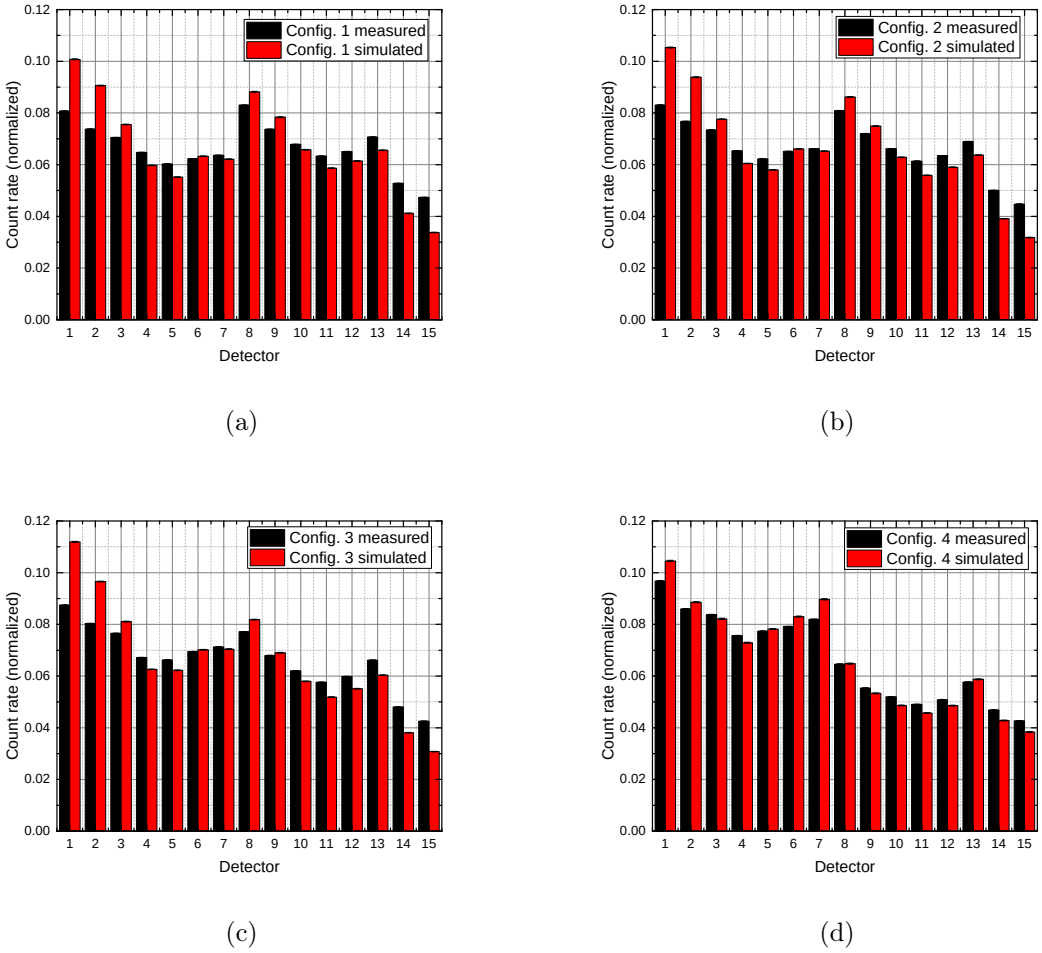

FIGURE 4.3: Normalized count rates per ^{3}He tube for configurations 1-4.

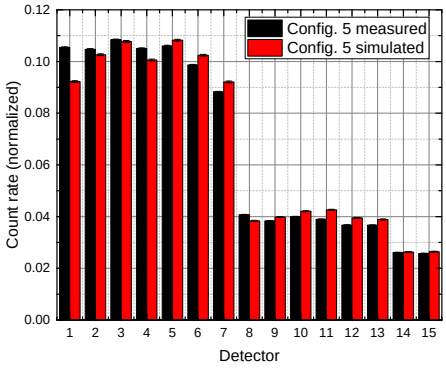

(a)

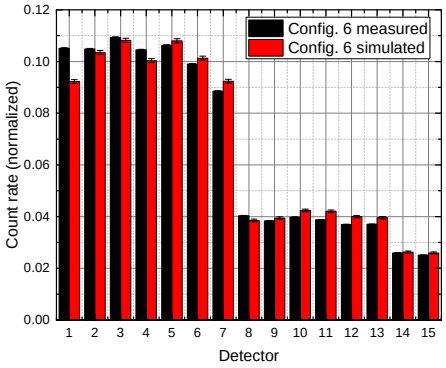

(b)

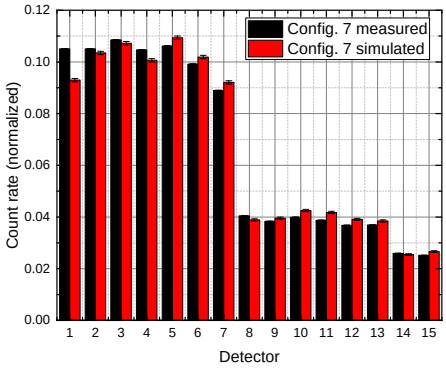

(c)

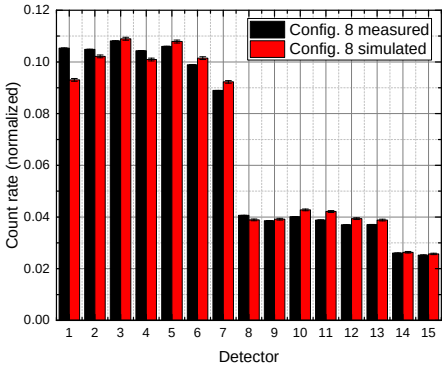

(d)

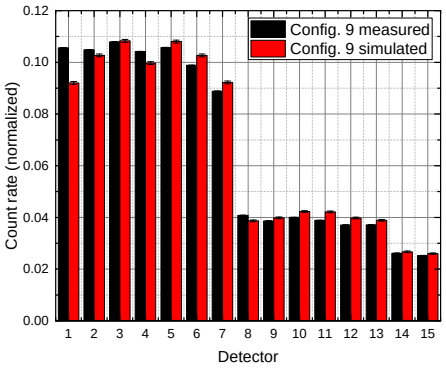

(e)

FIGURE 4.4: Normalized count rates per ^{3}He tube for configurations 5-9.

TABLE 4.4: FOM values for simulated and measured count rates per detector tube comparisons.

Configuration	FOM
1	69876
2	79135
3	66822
4	5717
5	3109
6	645
7	533
8	944
9	1094

From visual inspection, it is clear that there is generally good agreement between simulated and experimental normalized count rates per ^{3}He tube. According to the FOM values, best agreement (defined as a FOM value closer to unity) is shown for the highest water height configurations, namely configurations 6-9 (67 in.). This effect is most likely due to the fact that these configurations are less affected by the PuBe source, because of the water shielding neutrons from the PuBe source as well as the increase in neutrons coming from the core at the higher multiplication. The asymmetry in the count rate distributions for configurations 1-4 is caused by contributions from the non-centrally located PuBe starter source for the RCF. If the PuBe source were not present the outer tube pairs (1 and 7, as well as 8 and 13) would be expected to have similar count rates to each other. However, because the PuBe source is located towards the side of the MC15 containing tubes 1 and 8, these tubes display much higher count rates than tubes 7 and 13.

The RCF PuBe starter source, which is located above the core within a layer of paraffin wax shielding, was not well characterized at the time of the CaSPER measurement. Neither the source strength nor the diameter of the hole containing the source inside the wax shielding was well known. A series of simulations was therefore performed in order to ascertain the PuBe strength and shielding specifications that gave the best match to the CaSPER measurements. The details are summarized in Appendix A.

Measured and simulated row ratios, the ratio of the number of counts in the front row (tubes 1-7 in Figure 2.4) of the NoMAD to the number of counts in the middle row (tubes 8-13) of the NoMAD, are plotted in Figure 4.5 as a function of water height. As the neutron spectrum becomes softer, the row ratio increases. This increase in row ratio is expected because lower energy neutrons require less moderation in the polyethylene before reaching the energy range at which they can be detected by the ^{3}He tubes. Therefore, at lower energies the neutrons are more likely to interact with the front rather than the middle row of ^{3}He tubes.

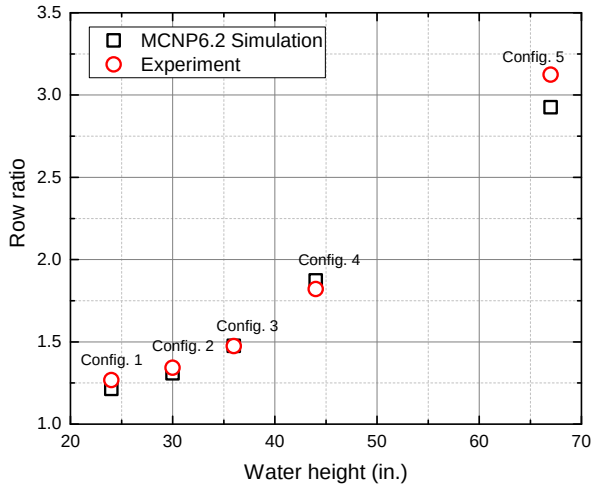

FIGURE 4.5: Row ratio vs. water height.

Measured and simulated Feynman histograms for various water and CR heights are shown in Figures 4.6-4.9. Poisson distributions constructed using the mean of each measured histogram are plotted as well. A measurement of a non-multiplying system would be expected to produce a Poisson-shaped Feynman histogram; the deviation from Poisson is correlated with the multiplication of a system. A list of FOM values for the Feynman histograms is shown in Table 4.5. It should be noted that the FOM in Equation 4.2 does not account for the fact that the uncertainties corresponding to the larger multiplet bins are inherently larger than those of the smaller multiplet bins. Therefore, this type of FOM puts more weight on differences between smaller multiplet bins. A new proposed FOM (Equation 5.4) that will be applied to future experimental results is discussed later in this work.

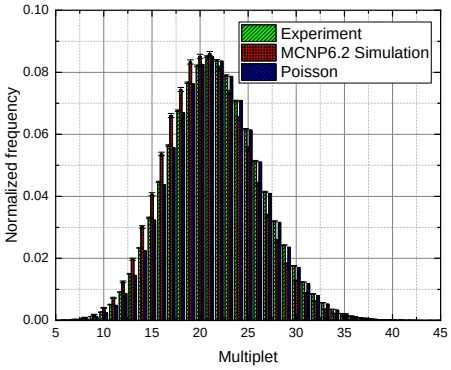

(a) 24 in., Configuration 1.

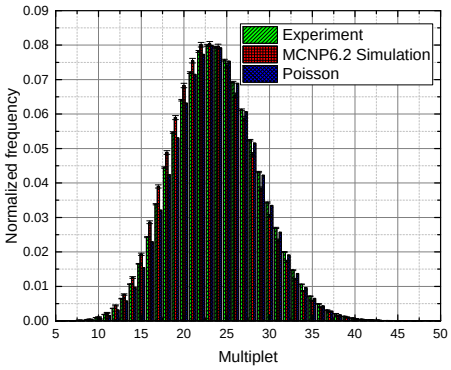

(b) 30 in., Configuration 2.

FIGURE 4.6: Feynman histograms for various water heights.

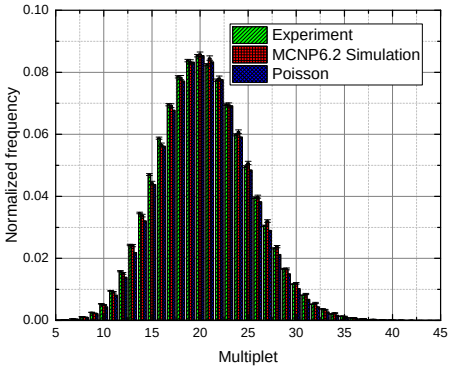

(a) 36 in., Configuration 3.

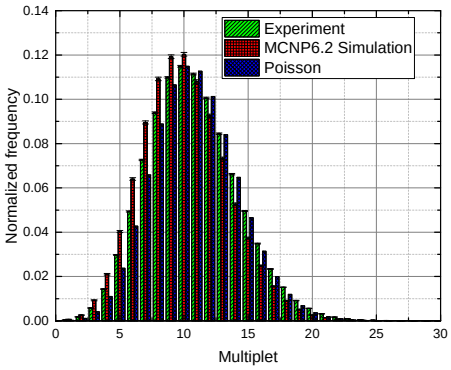

(b) 44 in., Configuration 4.

FIGURE 4.7: Feynman histograms for various water heights.

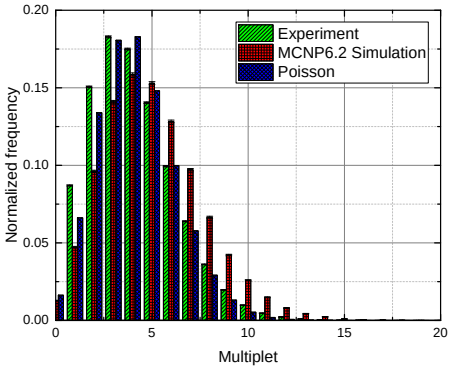

(a) 0 in., Configuration 5.

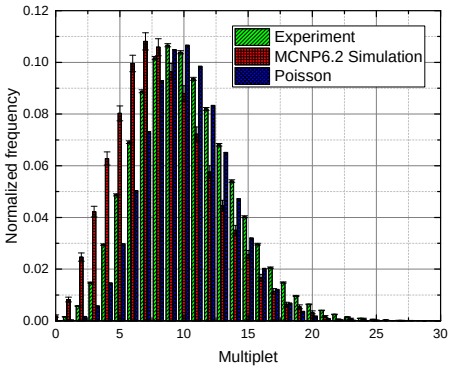

(b) 16 in., Configuration 6.

FIGURE 4.8: Feynman histograms for various CR heights.

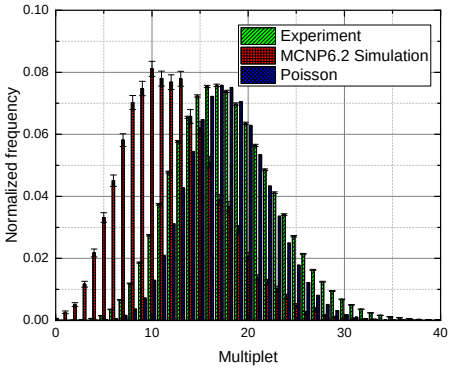

(a) 20 in., Configuration 7.

FIGURE 4.9: Feynman histograms for 20 in. CR height.

TABLE 4.5: FOM values for simulated and measured Feynman histogram comparisons.

Configuration	FOM
1	3975
2	1372
3	119
4	6834
5	20358
6	1845
7	21364

The Feynman histograms show an interesting trend with increasing water height. Initially, the histogram begins to shift to higher multiplets. At a certain turning point at which increasing shielding outweighs increasing multiplicity, the histograms begin to shift back to lower multiplets. It is expected that measured and simulated histograms deviate more at the highest water heights, due to the increased multiplication. This expectation is based on the fact that as multiplication increases the variance (width) of the histogram is also increasing. At high multiplication neutrons are more likely to be detected in small bursts over

short periods of time. Because multiplication is proportional to the deviation from Poisson statistics, the Feynman histograms at higher multiplication also show more deviation from Poisson. The FOM values show that 44 in. water height does indeed show more deviation between simulated and measured histograms than any of the lower water height configurations. The data at 36 in. water height show the best agreement according to the FOM values as expected due to the fact that the RCF PuBe source configuration optimization (Appendix A) was conducted using simulations of the 36 in. water height configuration. This configuration was chosen because it is a mid-level water height and therefore the most representative of all of the measured configurations. To simplify the PuBe source model optimization process, only this representative configuration was used.

Figure 4.10 shows plots of Y_2 versus gate width (see Equation 1.11). These plots were used to determine the optimal gate width to obtain singles, doubles, leakage multiplication, and Feynman histogram results. Ideally a gate width at which all Y_2 plots have reached an asymptote is chosen, because this gate width yields the "true" count rates. A gate width of $\tau = 3368\,\mu s$ was chosen. Although not all configurations have reached an asymptote at this gate width, data processing limitations did not allow for a larger gate width to be chosen. Because comparisons between simulated and measured results are of primary interest, and both simulated and measured results were taken at the same gate width, this is not a concern. It is interesting to note that Y_2 reaches a larger asymptote at a longer gate width as water height increases. Although this behavior could be caused by other factors, in the case of the CaSPER measurement the larger asymptote is most likely due to the increase in multiplication, while the longer gate width is due to the increase in moderation.

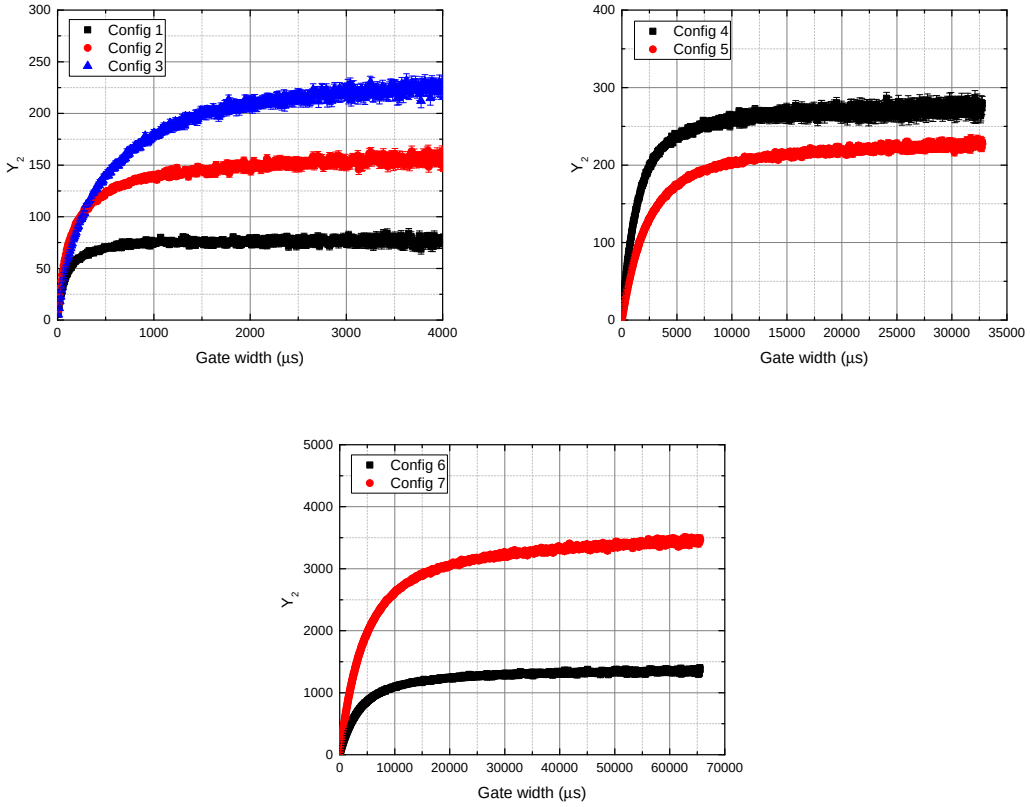

FIGURE 4.10: Y_2 vs. gate width for various configurations.

Measured and simulated (MCNP6.2) singles and doubles rates are plotted in Figure 4.11 as functions of water height, in Figure 4.12 as functions of control rod height, and in Figure 4.13 for the delayed critical configurations.

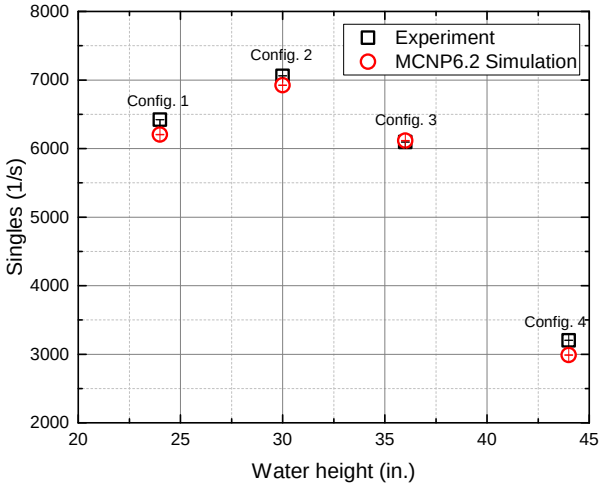

(a)

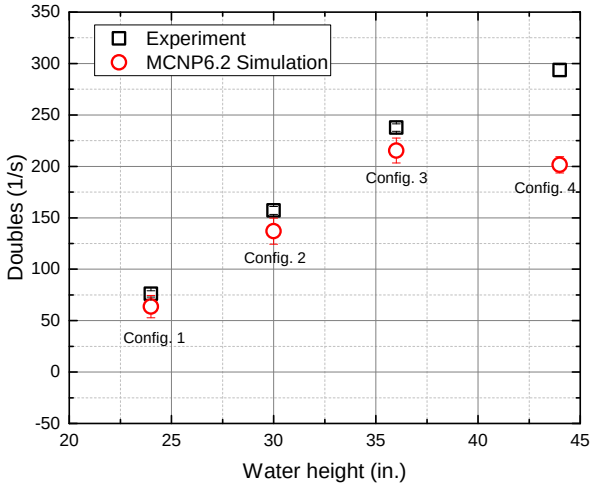

(b)

FIGURE 4.11: R_1 and R_2 as functions of water height. The R_1 trend illustrates the trade-off between shielding and multiplication in a water moderated system.

The trends shown in Figure 4.11 are the result of the trade-off between increasing multiplication and shielding with increasing water height. As the water height is increased from lower levels, both the singles (R_1) and doubles (R_2) rates increase due to increasing multiplication.

However, as the water begins to shield the detector from the core (at 30 in. the water has just begun covering the bottom of the NoMAD), the singles rate decreases. This decrease in singles occurs because the increased shielding is now overcoming the increasing multiplication and fewer neutrons are reaching the detector. The doubles rate does not seem to decrease within the range of water heights measured, however. This is most likely due to the fact that the doubles rate depends more heavily on multiplication, as compared to the singles rate. A true doubles event can only come from fission, and the fission rate is directly related to multiplication, while singles events can occur in any system regardless of the multiplication. Additionally, the correlated neutrons are emitted at fast energies and require moderation to reach the energy range in which the NoMAD is sensitive to neutrons.

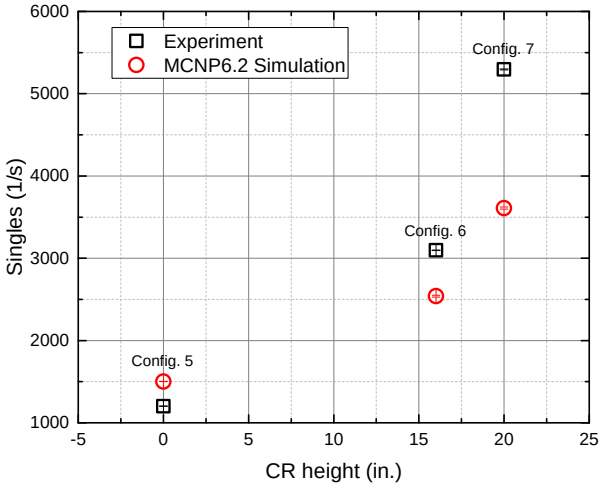

(a)

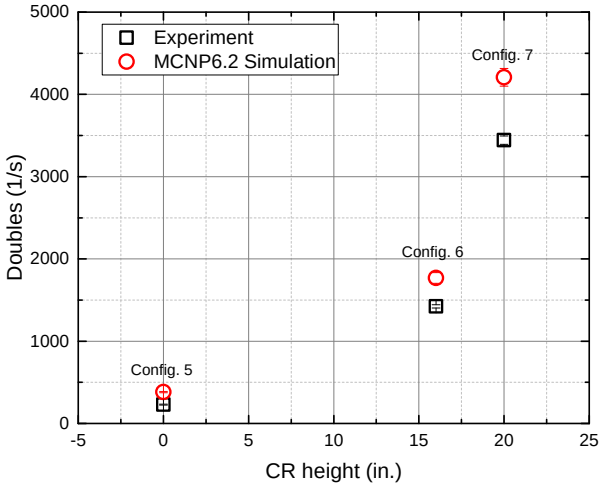

(b)

FIGURE 4.12: R_1 and R_2 as functions of CR height, for a water height of 67 in.

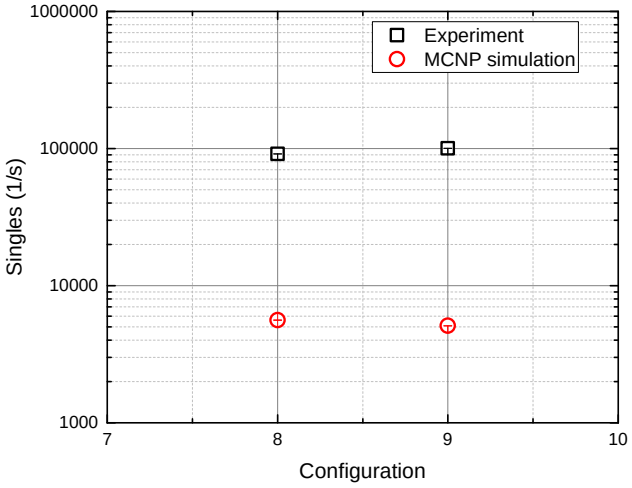

(a)

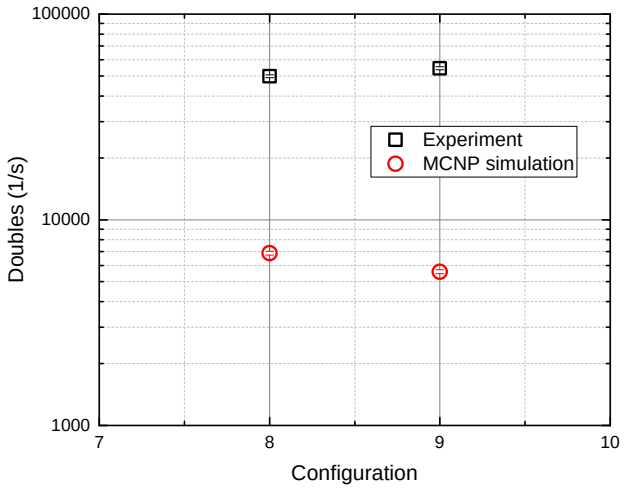

(b)

FIGURE 4.13: R_1 and R_2 for the delayed critical configurations.

Increasing CR height (removing CR's from the core) increases multiplication without increasing shielding. Therefore, it is expected that Figure 4.12 shows trends of purely increasing singles and doubles rates with increasing CR height. Because multiplication is very high for configurations 5-9, small discrepancies in the model will lead to large differences in

simulated and measured singles and doubles rates. The measured results for the delayed critical configurations in Figure 4.13 are an order of magnitude larger than the simulated results. The magnitude discrepancy is most likely due to the exponential increase in neutron population that occurred when the reactor was briefly brought to a delayed supercritical state during the approach to critical procedure. The neutron population remained at this elevated level during the subsequent measurements at delayed critical, and because the supercritical excursion was not modeled in MCNP, this behavior was not included in the simulation. It is interesting to note that both simulated and experimental results are very similar between the two delayed critical configurations, even though the CR setup was different for each.

Neutron lifetime, the inverse of the prompt decay constant, was obtained from fits of the measured Rossi data. Rossi data plots are shown in Figures 4.17 and 4.18. Alternatively, lifetime could have been obtained from fits of the Y_2 plots. However, the residuals (differences between the actual and predicted values of a regression model) trends displayed much worse behavior than the corresponding Rossi residuals. See Figure 4.16 for a representative example. It is much preferable to have residual values center around zero with no increasing or decreasing trends, as in the Rossi residual plot. Neutron lifetime, $\frac{1}{\lambda}$, and leakage multiplication, M_L, are plotted versus water and CR heights in Figures 4.14 and 4.15. The method used to calculate ϵ, and therefore M_L, is discussed in Appendix B. Only measured Rossi data and lifetime fits were obtained, and these measured lifetimes were used to calculate simulated doubles and leakage multiplication results.

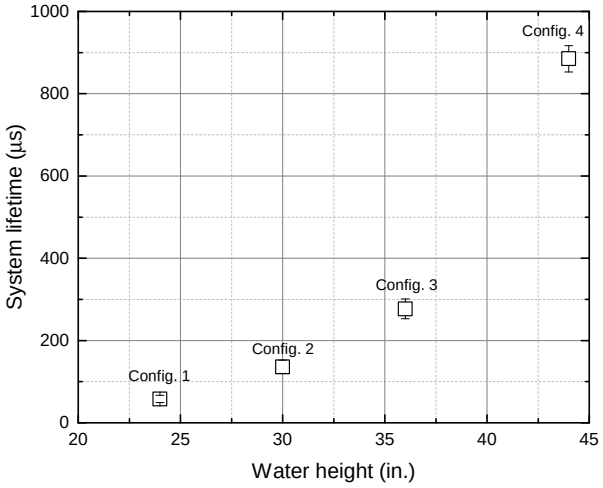

(a)

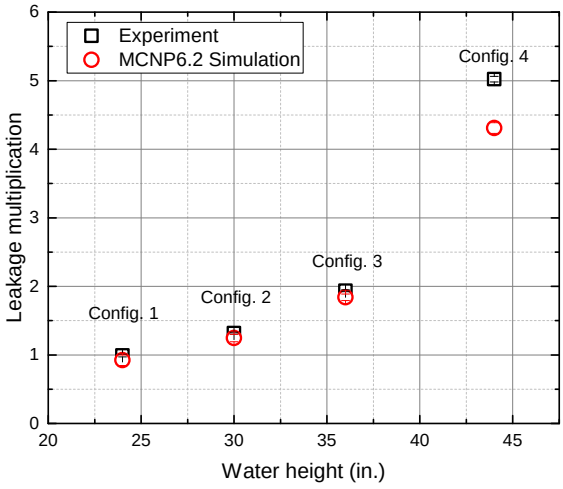

(b)

FIGURE 4.14: Neutron lifetime and multiplication as functions of water height.

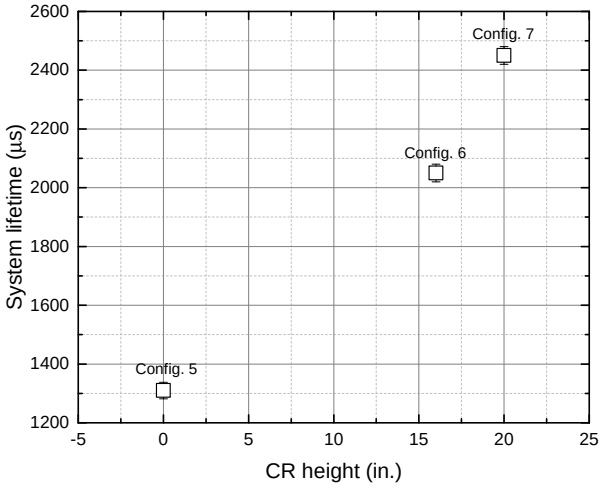

(a)

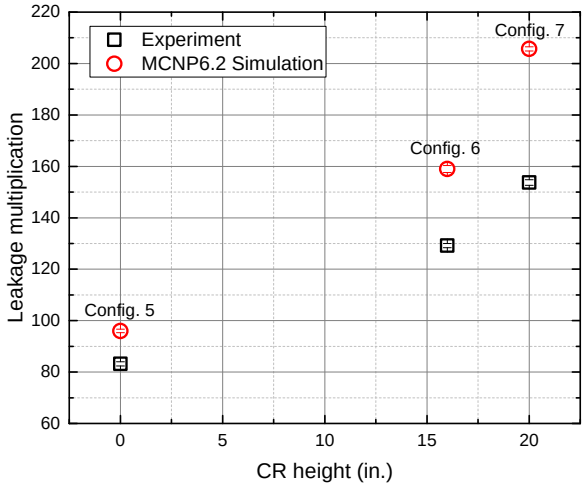

(b)

FIGURE 4.15: Neutron lifetime and multiplication as functions of CR height.

Both neutron lifetime and leakage multiplication increase with increasing water and CR height, as expected. The increase in neutron lifetime is due to the increased time the neutrons surrounded by water spend in the slowing down range. It is interesting to note that neutron lifetime and leakage multiplication follow similar trends as a function of water height. This

behavior has been previously observed for thermal uranium systems [66].

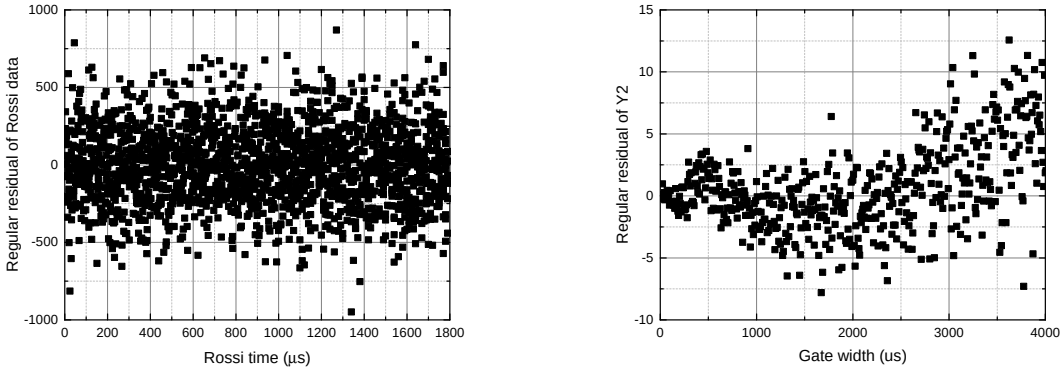

(a) (b)

FIGURE 4.16: Regular residual plots for Rossi and Y_2 fits at 36 in. water height, using double decay constant fits. The Rossi residual shows a much more desirable trend as compared to a single decay constant fit.

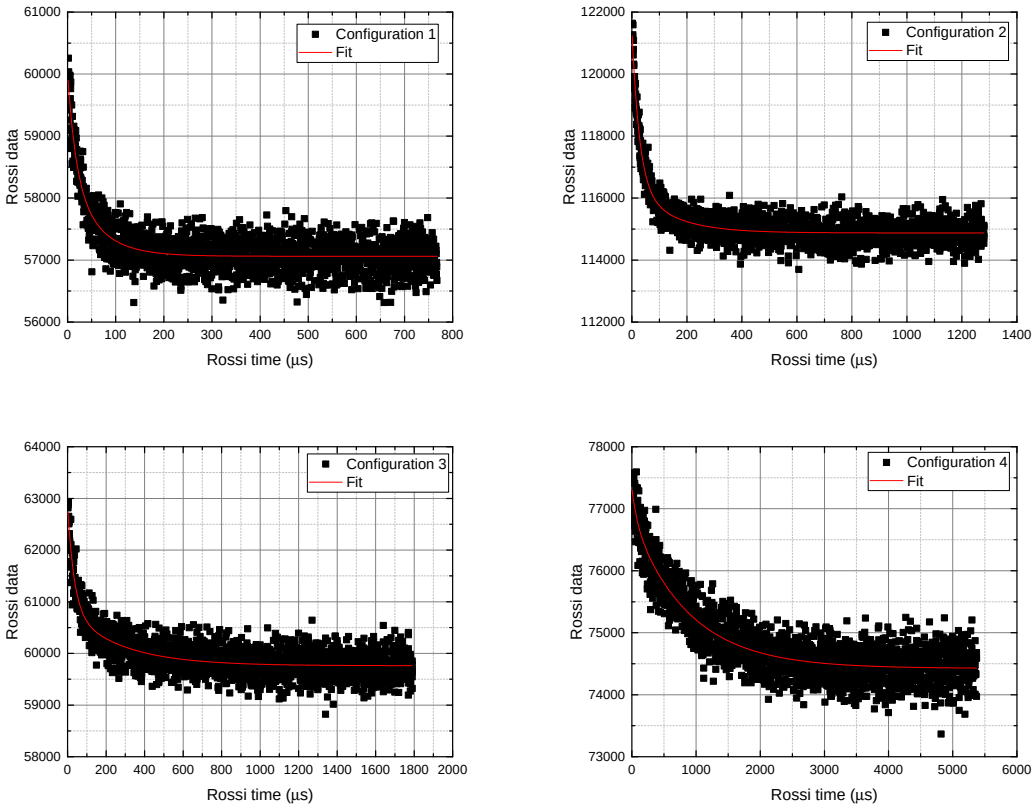

FIGURE 4.17: Rossi data vs. Rossi time for measured configurations 1-4. Double exponential fits were used.

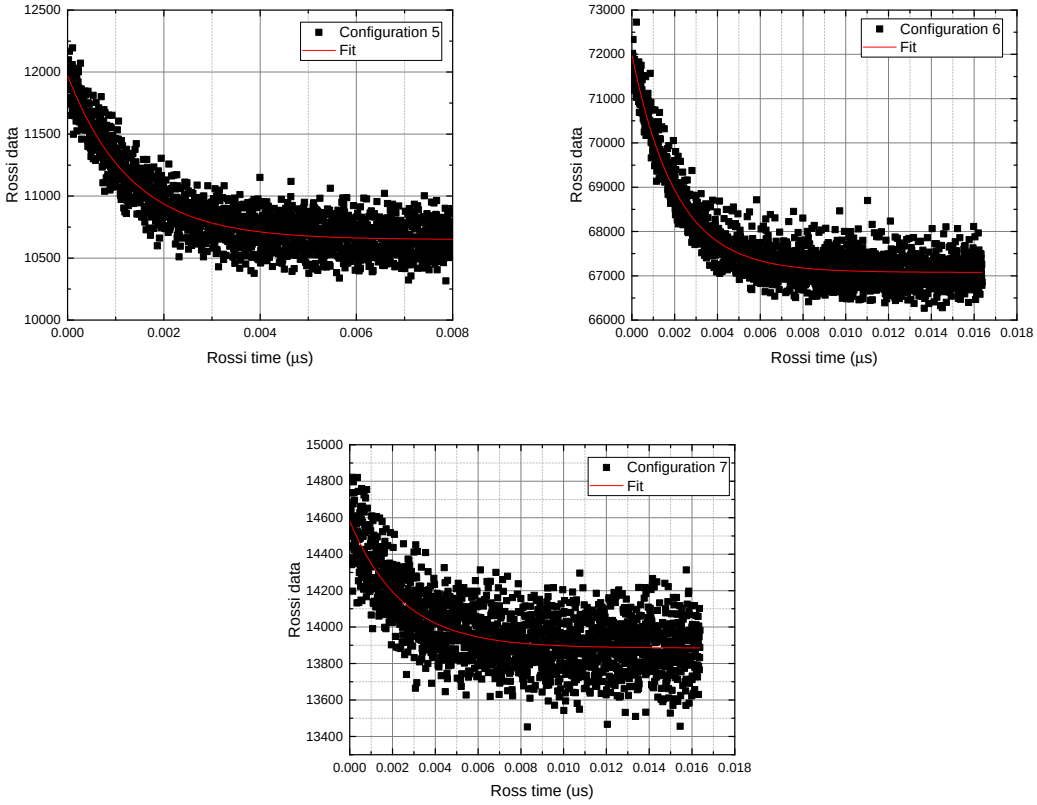

FIGURE 4.18: Rossi data vs. Rossi time for measured configurations 5-7. Single exponential fits were used.

In order to separate the multiplying system and detector lifetimes, double rather than single exponential fits were used to fit the Rossi data for configurations 1-4. For the other configurations, the detector lifetime is small enough compared to the system lifetime that only a single exponential fit is required.

Because of the difficulties determining efficiency and leakage multiplication in the CaSPER measurement, an efficiency-independent ratio (Equation 4.3) [80, 81] is also plotted in Figure 4.19. It is encouraging that this efficiency-independent parameter compares well between simulated and measured results.

$$S_{m2} = \frac{R_2}{R_1^2} \tag{4.3}$$

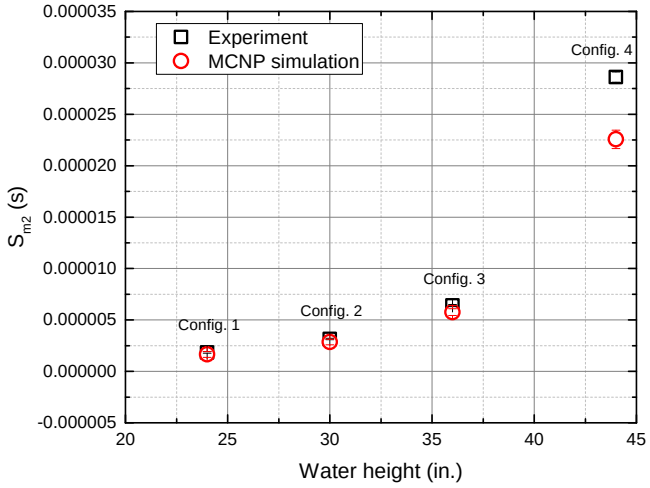

FIGURE 4.19: Efficiency-independent ratio plotted for simulated and measured data.

4.6 Physical uncertainties

In order to determine the sensitivity of simulated results to physical parameter uncertainties (systematic uncertainties), perturbation analysis was carried out for various physical parameters of interest. For each parameter of interest, the parameter was varied by an amount equal to 5 times its uncertainty. This variation was performed using the model of configuration 3 from Table 4.3. The resulting changes in singles and doubles rates, per standard deviation change in the physical parameter, are listed in Table 4.6.

TABLE 4.6: Change in observables, per standard deviation perturbation of the parameter of interest, obtained using configuration 3.

Physical parameter	Standard deviation	Singles sensitivity	Doubles sensitivity
Water height	1 in.	91 s^{-1}	7 s^{-1}
CR height	1 in.	2 s^{-1}	1 s^{-1}
NoMAD distance	2 cm	252 s^{-1}	25 s^{-1}
^{252}Cf strength	1860 s.f./s	112 s^{-1}	9 s^{-1}
PuBe strength	1.4E6 n/s	404 s^{-1}	26 s^{-1}

It is apparent that singles and doubles rates are most sensitive to changes in PuBe strength and NoMAD distance, followed by ^{252}Cf strength and water height, and are very insensitive to changes in CR height. It is expected for the results to be much more sensitive to changes in coarse (water) than fine (CR's) reactivity control. However, it should be noted that the uncertainty analysis was carried out in a fairly insensitive region of the CR reactivity worth curve. If configuration 6 or 7 were used instead of configuration 3, the sensitivities to CR height would be expected to be larger. The fact that changes in PuBe strength have the largest effect on the observables once again highlights the fact that the RCF PuBe source was unwisely neglected during the design phase of the CaSPER campaign.

It should also be noted that not all possible physical uncertainties were investigated. There are uncertainties associated with the exact fuel composition and density, water temperature, CR boron content, etc. However, these parameters are expected to have smaller sensitivities than the the investigated parameters. Because this work is meant to be a starting point for future measurements rather than a benchmark itself, an exhaustive uncertainty analysis was not carried out. Due to the presence of an above-core starter source that is not well characterized, a benchmark of the CaSPER measurements would be impossible.

4.7 Research reactor protocol

The Critical and Subcritical 0-Power Experiment at Rensselaer (CaSPER) campaign was designed and executed to establish a protocol for advanced subcritical research reactor measurements. For past subcritical benchmarks [5, 9, 61], protocol has consisted of measuring a multiplying system (historically symmetric) with ^{3}He multiplicity detectors around 50 cm away on either side of the system. Measurements were taken both with a bare multiplying system and with symmetric metallic reflectors. Data analysis was conducted using the Hage-Cifarelli formalism based on the Feynman Variance-to-Mean method. Even with various reflector materials, the neutron spectra remained predominantly epithermal. This protocol does not particularly apply to a pool-type research reactor measurement campaign. A multiplying pool-type research reactor system is not symmetric, a large amount of water reflection is used in place of metal reflectors, the neutron spectra span a range between fast and thermal at different water heights, etc. Many lessons were learned throughout the execution of the CaSPER measurements, that helped contribute to a modified protocol, and will be expounded upon here for the benefit of future experimenters.

For the RCF, the water temperature is just over 80°F, and the fuel reaches the same temperature as the water in steady state. 80°F is very close to room temperature. Because

water density and nuclear data may vary at different temperatures, nuclear data libraries evaluations exist at temperatures other than room temperature. However, the closest evaluations are either below 0°F or in the hundreds of °F. Therefore, the evaluation at room temperature was used in this work. For future benchmark-quality pool-type research reactor measurements, however, the temperature of the moderating water in the reactor core may need to be taken account.

Additionally, one must be aware of the trade-off between shielding and multiplication in a water moderated system. This trade-off is shown in the trends of singles and doubles rates as functions of water height. In Figure 4.11, R_1 first increases as a function of water height, reaches a turning point, and then begins decreasing with further increases in water height. While this turning point is not reached in the CaSPER measurement for R_2, perhaps future experimenters will be able to further observe and predict this behavior.

Practically, an extremely robust watertight system must be made available to protect the neutron multiplicity detector from water damage inside a water moderated reactor core if the detector is placed directly in the core. Additional material (i.e., Pb blocks, straps) may be required to lock the detection system into place and keep it from floating or otherwise deviating from the desired measurement position. In the CaSPER measurement, ratchet straps were used to tie the NoMAD detector housing and a layer of Pb bricks to an aluminum stand that held the detection system in place inside core. However, the detector system does not always have to be placed directly inside the core in pool-type research reactor measurements. If the core is small enough that the water does not attenuate the neutron flux significantly, the detector system can be placed outside the core. The detector system can also be placed on a stand above the core. For CaSPER, the reactor core was too large to allow for an acceptably large signal outside the core (parametric study results indicate that this would have been possible if the reactor tank radius had been less than 60 cm). In addition, both the direct upward neutron streaming from the ^{252}Cf source in the center of the fuel rods and the presence of the above-core PuBe source caused the above-core detector system placement option to be rejected. Sources contained in and around the reactor that are normally neglected by reactor operators (i.e., a PuBe startup source) cannot be neglected in the case of neutron multiplicity measurements. Indeed, potential contributions from neglected external radiation sources have been an Achilles heel for many experimentalists; for example, in the case of bubble fusion, one of the main sources of contention was whether or not the sources of neutrons had been properly characterized [82].

In addition to comparing configurations at the same reactivity with differing control rod heights (configurations 8 and 9), it would be interesting to obtain the same reactivity from different water and control rod height combinations to determine if changing both the fine (control rod) and coarse (water) reactivity controls would compare better or worse than changing only the fine reactivity control. It is interesting to note that, according to Figure 4.14, leakage multiplication and system neutron lifetime follow similar trends as a function of water height. This trend has been observed in previous thermal subcritical measurements involving enriched uranium. It is also important to note that the extremely large discrepancies between simulated and measured results at delayed critical, as seen in Figure 4.13, were likely caused by a previous excursion into a delayed supercritical state. As previously discussed, an exponential increase in neutron population occurred when the reactor was briefly brought to a delayed supercritical state during the approach to critical procedure. The neutron population remained at this elevated level during the subsequent measurements at delayed critical, and because the supercritical excursion was not modeled in MCNP, this behavior was not exhibited in the simulation. In future critical measurements, this discrepancy can be avoided by bringing the reactor down to a subcritical state, after the approach to critical process, to allow the neutron population to die down. The reactor can then be brought back up to a critical state without the increase in neutron population caused by the supercritical excursion.

Table 4.6 shows that the observables in this experiment are most sensitive to changes in NoMAD distance and RCF PuBe source strength. Conversely, singles and doubles rates are not very sensitive to changes in control rod height. Therefore, for subcritical research reactor measurements of this type it is most desirable to be able to very accurately measure both the core-detector distance and the characteristics of any strong in-core starter source. However, larger uncertainties on fine reactivity control are allowable when operating in a generally insensitive region of the fine reactivity control worth curves.

Part of the protocol determined during the CaSPER measurements is related to data analysis. Applying a FOM (Equation 4.2) to comparisons between simulated and measured Feynman histograms (Table 4.5) is a useful method for quantifying the deviation between simulated and measured histogram results, such as that are seen in Figures 4.6 and 4.8, rather than simply using qualitative inspection. The FOM also proves useful when applied to comparisons between simulated and measured counts-per-tube plots (Table 4.4), especially for determining an optimal match between simulated and measured results (see Appendix A). Several issues arose in determining both the prompt neutron decay constant and the absolute detector

efficiency required to calculate leakage multiplication. Although the Hage-Cifarelli formalism based on the Feynman Variance-to-Mean method can take into account contributions from (α, n) sources, there is no provision for (α, n) sources that aren't coincident with the fission source (see Appendix B for how this difficulty was addressed). Both the Y_2 and the Rossi fitting method were used to determine the prompt neutron decay constants for configurations 1-4. In order to separate the multiplying system and detector lifetimes, double rather than single exponential fits were used in both cases. In typical fast SNM subcritical measurements, the detector lifetime is longer than the multiplying system lifetime. For CaSPER, the experimenters consider the system to include everything inside the reactor tank. In this case, the system lifetime is much longer than the detector lifetime and results can be calculated, using the system lifetime, at large enough gate widths that the detector lifetime has died out. By comparing residual plots of Y_2 and Rossi fits (Figure 4.16), it was determined that Rossi alpha fitting is a better method to obtain neutron lifetime in highly reflected and moderated systems, such as research reactors. Measured doubles rates were calculated at $\tau = 32\ \mu s$, before the detector lifetime had died out, and at $\tau = 3368\ \mu s$, after the detector lifetime had died out, as shown in Figure 4.20. It seems that in this case the detector lifetime has a small effect on the results. This small effect is most likely due to the fact that for such a thermal system, the system neutron lifetime is very long compared to the detector lifetime, and therefore the detector lifetime can be neglected even at short times (small gate widths).

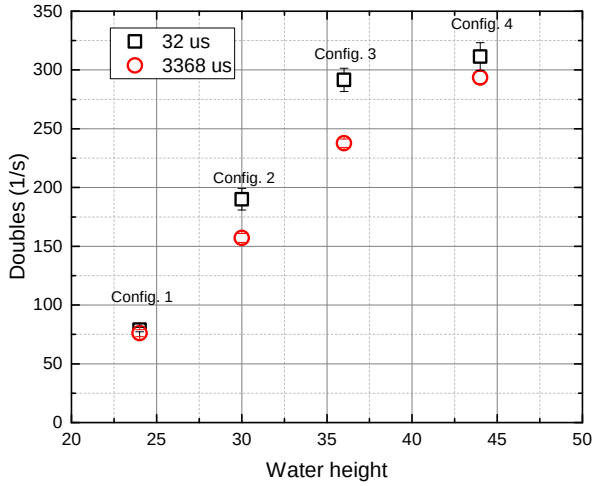

FIGURE 4.20: Measured R_2 results before ($\tau = 32\ \mu s$) and after ($\tau = 3368\ \mu s$) the detector lifetime dies out.

4.8 Application of research reactor protocol

As the next step following the establishment of a research reactor protocol by the CaSPER measurement, a series of advanced subcritical benchmark measurements at the zero-power Sandia National Laboratory (SNL) 7uPCX research reactor has been proposed. Ultimately the RPI research reactor experiments did not lead to a quality benchmark data set due to the previously mentioned presence of a legacy above-core starter Pu-Be source that could not be fully removed (procedurally or physically), and was not well characterized. Such a starter source will not be an issue for the proposed benchmark measurement at SNL, because any startup source can be removed and would be well known. Similar to the measurements at RPI, larger discrepancies between simulations and measurements at configurations with higher multiplication, especially at and near delayed critical, are expected. Figure 4.21 shows the geometry of the preliminary MCNP model that was created for the purpose of testing the feasibility of a measurement at the 7uPCX reactor with the LANL NoMAD detectors. The preliminary simulation results yield a singles and doubles rate of 6.0E3 and 1.95E5 s^{-1}, respectively. These are reasonable count rates, and the SNL benchmark measurement is considered both feasible and a promising application of the research reactor protocol established by the CaSPER measurement.

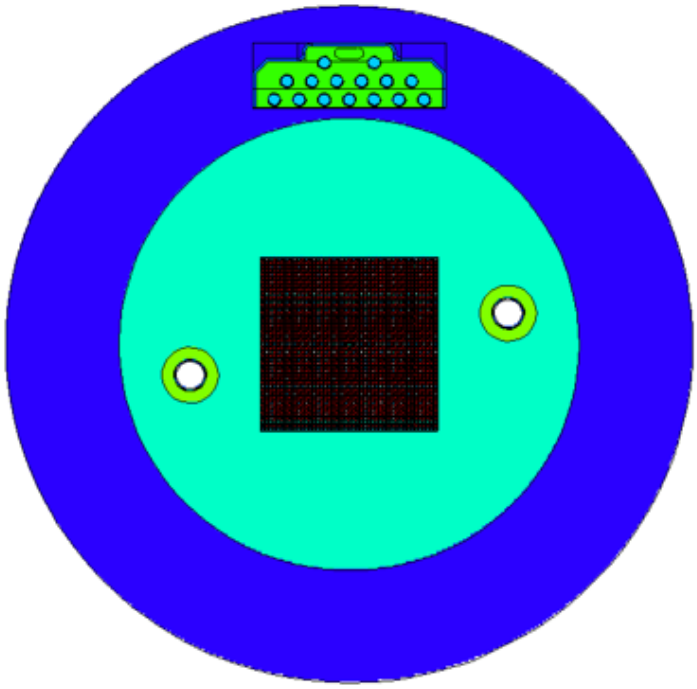

FIGURE 4.21: Preliminary MCNP model of the 7uPCX reactor with a NoMAD detector placed just outside the reactor tank.

In addition, a series of neutron clustering measurements were conducted at the RCF using the lessons learned from the CaSPER measurement [83]. This neutron clustering measurement was made possible because of the better understanding of count rates within the reactor, the lessons learned from submerging a detector system in a reactor water tank, and the existing detailed reactor and detector system MCNP model created for the CaSPER measurement. The simulations and design process of the clustering measurements were based off of the existing CaSPER model.

Chapter 5

Design and Analysis of Subcritical Experiments

Benchmark measurements are trusted to provide accurate comparisons between experimental and simulated data, for nuclear data and radiation transport code validation purposes. This portion of the work demonstrates how we can apply the previously discussed subcritical neutron multiplication measurements and simulations to better validate relevant nuclear data and radiation transport computational methods currently used for nuclear nonproliferation and safety applications. A Bayesian optimization algorithm framework has been applied to the design of subcritical neutron multiplication inference benchmarks. An improved FOM for quantitative comparison of Feynman histograms has been developed for application to nuclear data and computational methods validation.

5.1 Bayesian Optimization of Benchmark Design

Much of the following discussion is taken from the conference proceeding on the topic [84].

5.1.1 Description

A Bayesian optimization algorithm for benchmark experiment design has been developed in MATLAB. The source code is included in Appendix H. The purpose of the algorithm is to optimize a limited number of physical measurement parameters, using the Bayesian optimization sampling method to reduce the number of design simulations and computation time required to determine the optimal measurement configuration. Specifically for subcritical neutron multiplication inference measurements involving a 4.5 kg alpha-phase plutonium sphere (BeRP ball) ball, the design process typically involves maximizing the sensitivity of the effective multiplication factor, k_{eff}, to a certain cross-section, or set of cross-sections, of interest [9, 61]. The most recent BeRP benchmark also included HDPE reflection, in addition to Cu metal reflection, in multiple configurations [85]. The purpose of the HDPE is to increase the range of achievable multiplication states, and also serves to greatly increase

the sensitivity of the multiplication to various metal isotopes. The Bayesian optimization algorithm can be applied to quickly determine the configuration(s) at which the sensitivity to a specific cross-section(s) is maximized, by using the Bayesian sampling method to converge on the point of maximum sensitivity over a wide range of HDPE reflection thickness and positions (within the combined HDPE and metal reflection layer) within a minimal number of simulations.

Practically the Bayesian optimization method is applied by first choosing a few points, preferably equally spaced along the unknown sensitivity curve, to sample. In this work, "sampling" involves running a KSEN calculation in MCNP to determine the sensitivity of k_{eff} to the cross-section of interest. Then Gaussian process (GP) fitting is used to fit a curve and associated uncertainties to the sampled points. Finally, a utility function, which trades off between exploration (sampling points with large uncertainty) and exploitation (sampling points with large mean), is used to determine the next point to sample. This process repeats until a point is found at which the mean plus the uncertainty of the sensitivity curve at that point is greater than the sum of mean and uncertainty for all other points on the curve. The benefit of this method is that the maximum of the sensitivity curve can be converged upon intelligently, without having to brute-force sample the entire sensitivity curve.

5.1.2 Testing and validation

The Bayesian optimization algorithm has been tested and shown to quickly converge upon optimized configurations for both the already completed SCRαP benchmark, and the proposed future BeRP-Mo (BeRP reflected by molybdenum) benchmark. First, the algorithm was applied to a specific portion of the SCRαP design process. The goal was to determine the configuration at which the sensitivity of k_{eff} to the ^{63}Cu cross-section in the intermediate energy range (for this purpose defined as 0.625 eV - 100 keV) is maximized, over a total possible BeRP reflection thickness of 4", and using a combination of HDPE and Cu thicknesses. The first step of the goal was reached by, beginning with 4" of all Cu reflection, using the Bayesian optimization algorithm to determine the inches of reflection of Cu which, if replaced by HDPE (assuming the HDPE composes the inner layer, followed by an outer layer of Cu), yields the maximum sensitivity. The GP-fitted sensitivity curve output by the algorithm, along with the actual curve that was created with the brute-force method, and the points sampled before convergence was reached, is shown in Figure 5.1. The algorithm required only 15 sampled points to converge, compared to the 99 points generated by the brute-force method. The algorithm output an optimized HDPE thickness of 0.4", yielding a maximum KSEN output of 0.018. In order to be more consistent with the SCRαP benchmark, which

included only 0.5" thick shells of HDPE and Cu, the optimized HDPE thickness was rounded up to 0.5" for the next step in the Bayesian optimization design process.

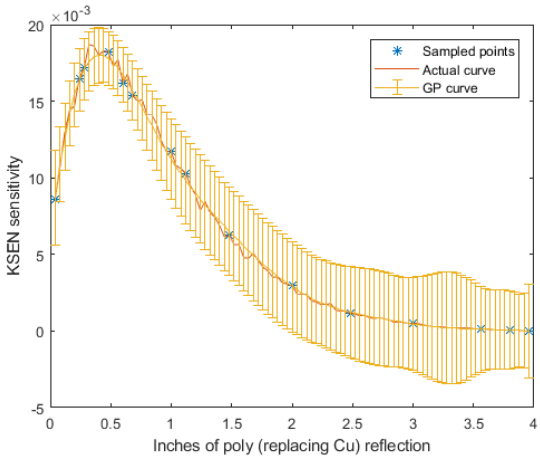

FIGURE 5.1: Sensitivity curve of k_{eff} to ^{63}Cu intermediate energy region cross-section, as output by the Bayesian optimization algorithm.

The second step involved, using the optimum HDPE thickness of 0.5", applying the Bayesian optimization algorithm to determine the optimal (at which the desired sensitivity is maximized) position of the 0.5" thick HDPE shell within the total 4" reflection thickness. The GP-fitted sensitivity curve output by the algorithm, along with the actual curve that was created with the brute-force method, and the points sampled before convergence was reached, is shown in Figure 5.2. The algorithm required only 8 sampled points to converge, compared to the 69 points generated by the brute-force method. The algorithm output an optimized HDPE position of 0" from the BeRP ball, yielding a maximum KSEN output of 0.018.

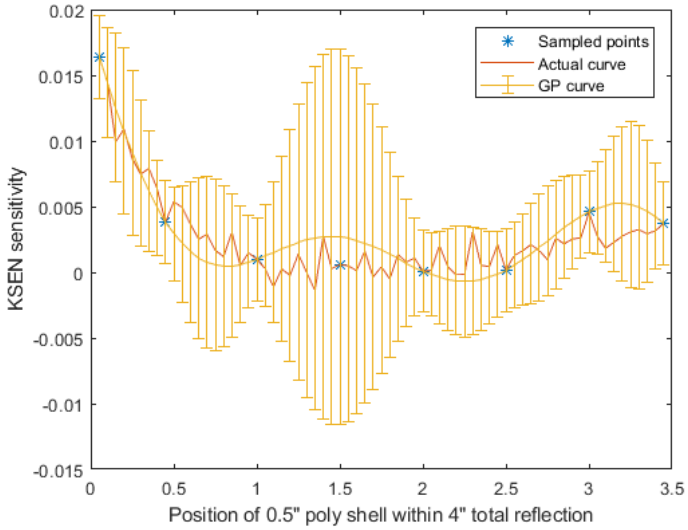

FIGURE 5.2: Sensitivity curve of k_{eff} to ^{63}Cu intermediate energy region cross-section, as output by the Bayesian optimization algorithm.

Therefore, the result of the application of the Bayesian optimization algorithm to SCRαP design is a configuration involving the BeRP ball reflected by an inner layer of 0.5" of HDPE, followed by an outer layer of 3.5" of Cu. This configuration is identical to configuration 15 of the benchmark, yields the same maximum sensitivity of 0.018 that was reported in the design process [60], and required only 23 KSEN runs as opposed to the 168 runs that would have been required to obtain the same information using the brute-force method.

Second, the algorithm was more extensively applied to the design of the future BeRP-Mo benchmark. Natural Mo is composed of 7 different isotopes: ^{92}Mo, ^{94}Mo, ^{95}Mo, ^{96}Mo, ^{97}Mo, ^{98}Mo, and ^{100}Mo. The Bayesian optimization algorithm was used to determine configurations, involving varying thicknesses of HDPE and Mo reflection summing to a combined reflection of 6", at which the sensitivities to the total cross-section for each Mo isotope in the intermediate energy region is maximized. Again, the first step was determining the optimum thickness of HDPE (assuming an inner layer of HDPE, followed by an outer layer of Mo) for each isotope. The GP-fitted sensitivity curves output by the algorithm, along with the actual curves that were created with the brute-force method, and the points sampled before convergence was reached, are shown in Figures 5.3-5.5. The algorithm required an average of only 15 sampled points per isotope to converge, compared to the 100 points generated for each isotope by the

brute-force method. For each isotope the algorithm output an optimized HDPE thickness between 0.4" and 0.52", yielding maximum KSEN outputs between 0.0009 and 0.0059. Again for simplicity the HDPE thickness was rounded to 0.5" for all isotopes for the next step in the Bayesian optimization design process.

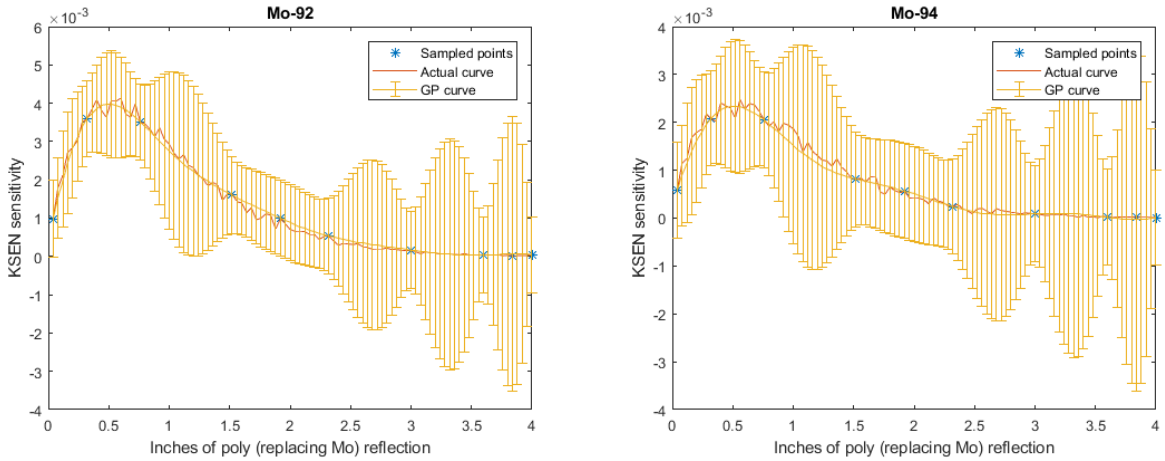

FIGURE 5.3: Sensitivity curve of k_{eff} to various Mo isotope intermediate energy region cross-sections, as output by the Bayesian optimization algorithm

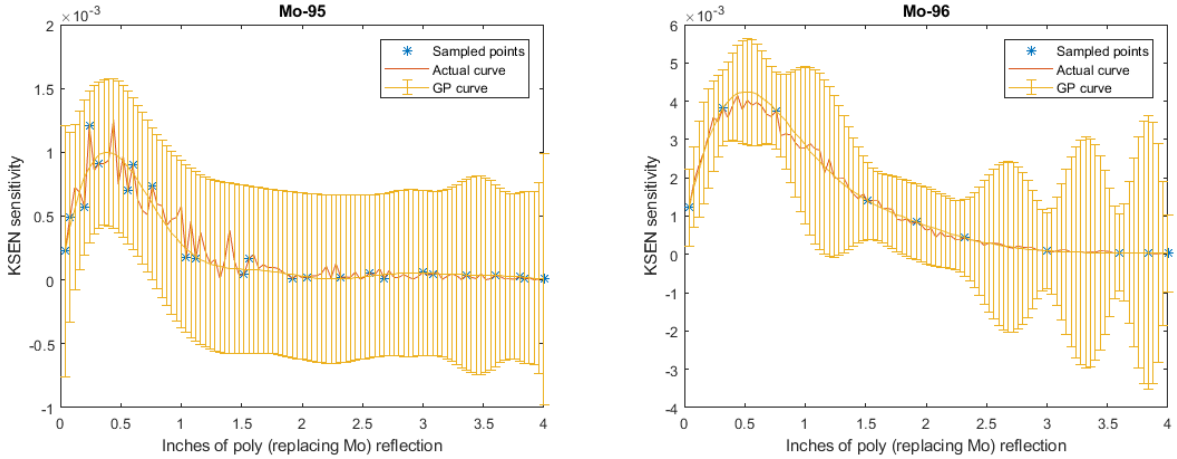

FIGURE 5.4: Sensitivity curve of k_{eff} to various Mo isotope intermediate energy region cross-sections, as output by the Bayesian optimization algorithm

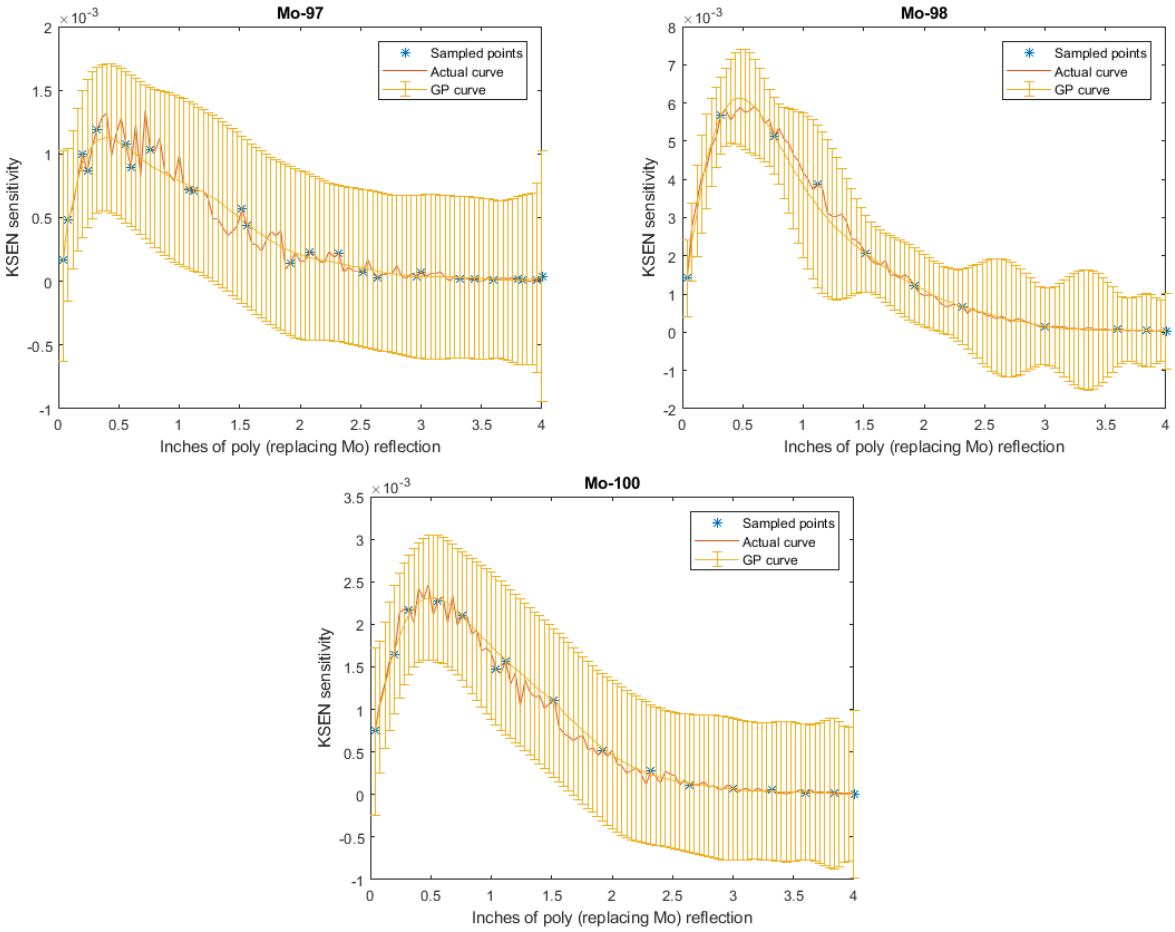

FIGURE 5.5: Sensitivity curve of k_{eff} to various Mo isotope intermediate energy region cross-sections, as output by the Bayesian optimization algorithm

The second step again involved, using the optimum HDPE thickness of 0.5", applying the Bayesian optimization algorithm to determine the optimal position of the 0.5" thick HDPE shell within the total 6" reflection thickness. The GP-fitted sensitivity curves output by the algorithm, along with the actual curves that were created with the brute-force method, and the points sampled before convergence was reached, are shown in Figures 5.6-5.8. The algorithm required an average of only 16 sampled points per isotope to converge, compared to the 137 points generated for each isotope by the brute-force method. For each isotope the algorithm output an optimized HDPE position of either 0.04" (isotopes 92, 94, 96, 98, and 100), 1.52" (isotope 95), or 1.92" (isotope 97) away from the BeRP ball, yielding maximum KSEN outputs between 0.0016 and 0.0059.

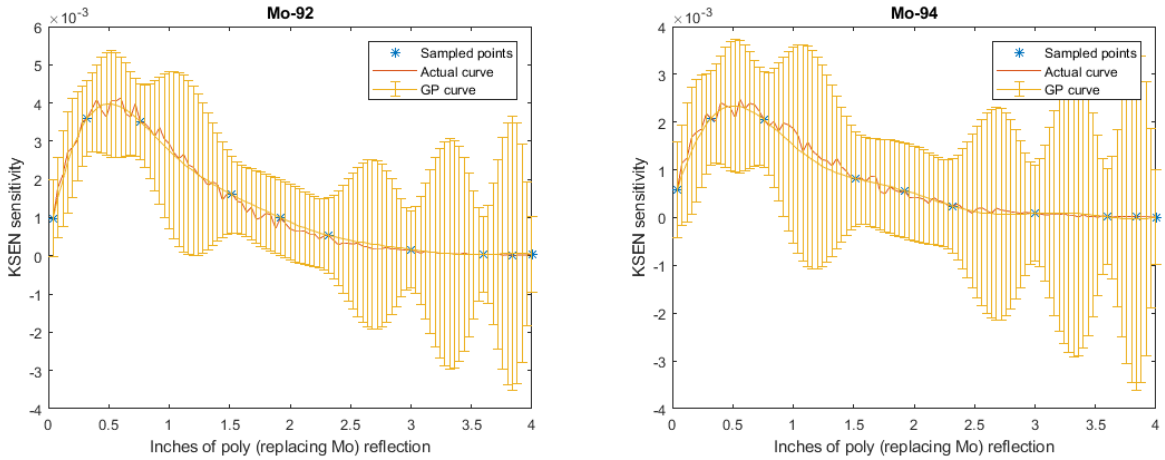

FIGURE 5.6: Sensitivity curve of k_{eff} to various Mo isotope intermediate energy region cross-sections, as output by the Bayesian optimization algorithm

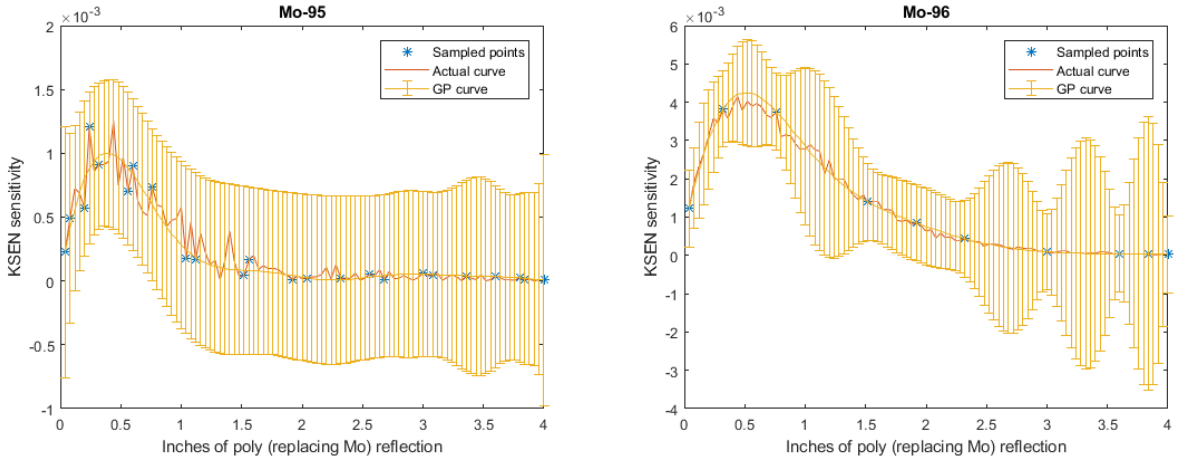

FIGURE 5.7: Sensitivity curve of k_{eff} to various Mo isotope intermediate energy region cross-sections, as output by the Bayesian optimization algorithm

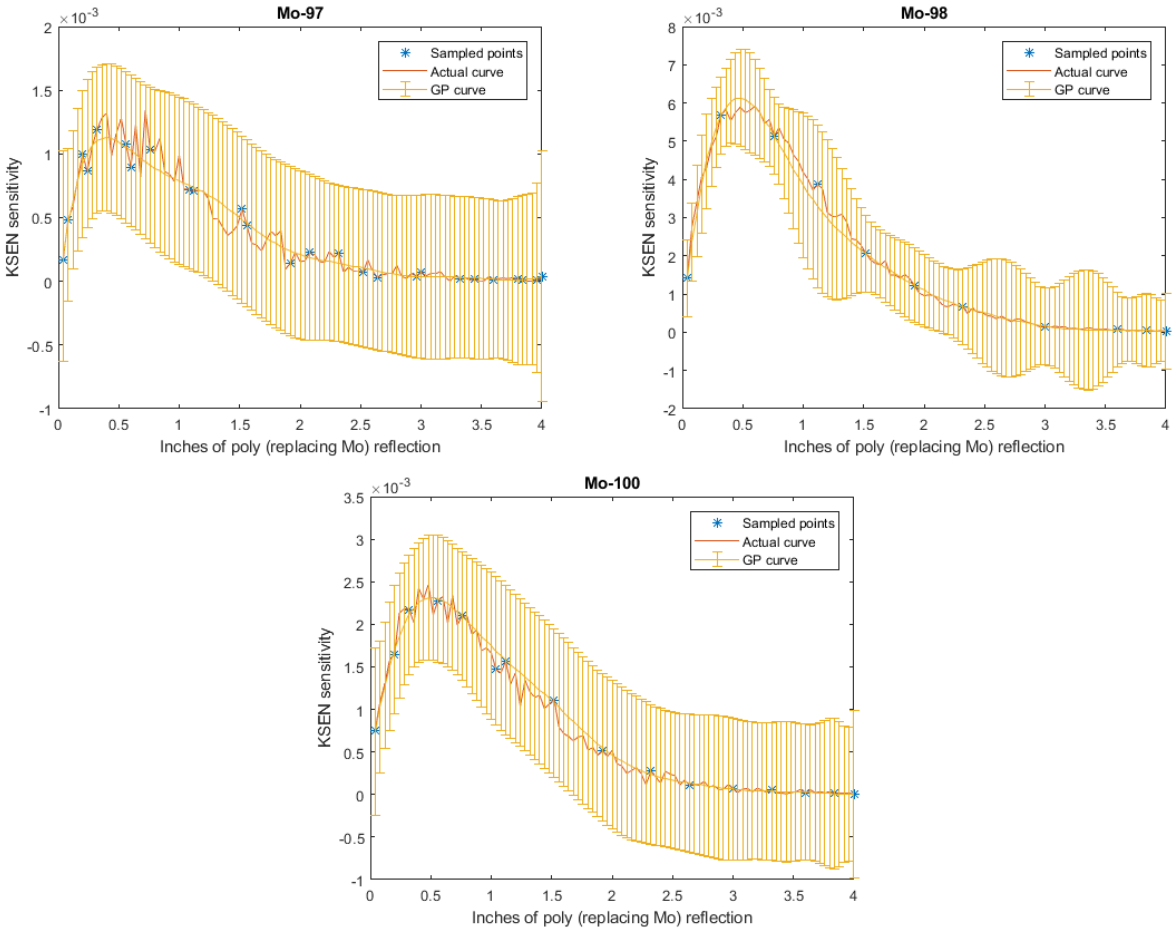

FIGURE 5.8: Sensitivity curve of k_{eff} to various Mo isotope intermediate energy region cross-sections, as output by the Bayesian optimization algorithm

Therefore, the result of the application of the Bayesian optimization algorithm to the proposed BeRP-Mo design is a combination of 3 different configurations. Configuration 1 is the BeRP ball reflected by 0.5" of HDPE, followed by 5.5" of Mo, and maximizes the sensitivity to ^{92}Mo, ^{94}Mo, ^{96}Mo, ^{98}Mo, and ^{100}Mo. Configuration 2 is the BeRP ball reflected by 1.5" of Mo, followed by 0.5" of HDPE, and then 4" of Mo, and maximizes the sensitivity to ^{95}Mo. Configuration 3 is the BeRP ball reflected by 2" of Mo, followed by 0.5" of HDPE, and then 3.5" of Mo, and maximizes the sensitivity to ^{97}Mo. Converging on these 3 configurations required only 217 KSEN runs as opposed to the 1659 runs that would have been required to obtain the same information using the brute-force method. The 2 examples of design of the SCRαP and BeRP-Mo benchmarks are good proof of the applicability of the Bayesian

optimization method to experiment design.

5.2 Improved Figure of Merit for Feynman Histograms

The goal of creating a figure of merit for Feynman histograms is to provide a quantitative comparison of measured and simulated histograms, for radiation transport code and nuclear data validation. To date, no one has rigorously evaluated or established a suitable FOM to quantify the degree of discrepancy between two Feynman histograms. Much of the following discussion is taken from the conference proceeding on the topic [86].

5.2.1 Old equation

Typically a FOM that takes into account the differences between each bin of the histograms, as compared to the magnitude of the combination of the corresponding uncertainties, is used, as previously presented in Equation 4.2.

Because the uncertainties corresponding to the larger multiplet bins are inherently larger than those of the smaller multiplet bins, this type of FOM puts more weight on differences between smaller multiplet bins. The new proposed FOM also takes into account sensitivity of leakage multiplication (which is most sensitive to higher multiplet bins) to each bin in the histogram. As previously mentioned, the ideal FOM value is 1, representing a discrepancy between simulated and measured histograms that is equal to the combined associated uncertainty.

5.2.2 Sensitivity calculation

Leakage multiplication is related to the deviation of the histogram from a Poisson distribution, as shown in Figure 5.9. The sensitivities of leakage multiplication to each bin in the Feynman histogram were calculated using standard uncertainty propagation techniques such as the chain rule (Equation 5.1) and the chain rule for partial derivatives (Equation 5.2). To create the new proposed FOM equation, the sensitivities are normalized and added as an additional factor to the past FOM. The formula for the sensitivities is presented in Equation 5.3 and the new FOM is shown in Equation 5.4. Because the sensitivities are normalized and sum to unity, the ideal value of the FOM is still unity. It should be noted that the notation used for the number of events in the n^{th} bin of a Feynman histogram (C_n) and the values used to calculated leakage multiplication (C_1, C_2, and C_3) are unrelated.

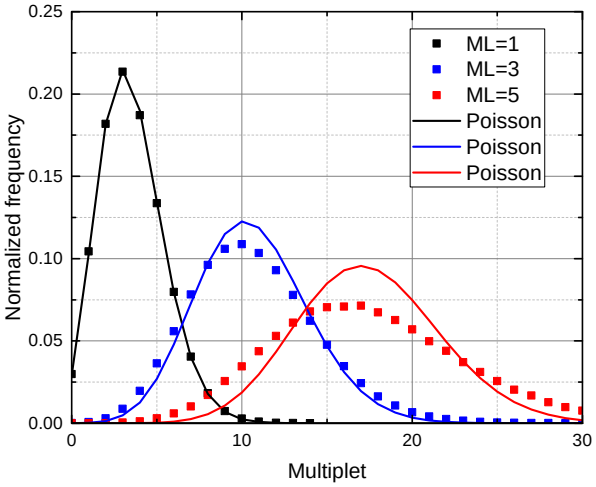

FIGURE 5.9: Relation between leakage multiplication and the deviation of the Feynman histogram from a Poisson distribution.

$$\frac{dy}{dx_n} = \frac{dy}{dx_1} * \frac{dx_1}{dx_2} * \frac{dx_2}{dx_3} * ... \frac{dx_{n-1}}{dx_n} \tag{5.1}$$

$$\frac{dy}{dx_n} = \frac{\partial y}{\partial x_1} * \frac{dx_1}{dx_n} + \frac{\partial y}{\partial x_2} * \frac{dx_2}{dx_n} + ... \frac{\partial y}{\partial x_{n-1}} * \frac{dx_{n-1}}{dx_n} \tag{5.2}$$

$$\frac{dM_L}{dC_n} = \frac{\nu_{s1}}{\tau \epsilon R_1 \sum_{n=1}^{N_{bins}} [C_n] \sqrt{C_2^2 - 4C_1C_3}} \left[-\frac{R_2}{R_1}(n - m_1) - \frac{1}{\omega_2}\left(-m_2 + m_1^2 - m_1 n + \frac{1}{2}n^2 - \frac{1}{2}n \right) \right] \tag{5.3}$$

$$FOM = \frac{1}{N_{bins}} \sum_{i=1}^{N_{bins}} \frac{(S_i - E_i)^2}{\sigma^2(S_i) + \sigma^2(E_i)} \left| \frac{dM_L}{dC_i} \right|_{norm} \tag{5.4}$$

5.2.3 Validation of new equation

For validation purposes, a fabricated test case involving a sphere of pure Pu-240 and Pu-239 was used. This test case was chosen to approximate the BeRP ball. Table 5.1 lists the input parameters used to create the test case, and Figure 5.10 shows the resulting Feynman histogram.

TABLE 5.1: Test case parameters.

Parameter	Value
Fission rate	130423 s^{-1}
Detector efficiency	0.012
Tube dead time	4.0 μs
Neutron lifetime	40.0 μs
Count time	300 s
Reported M_L	3.0

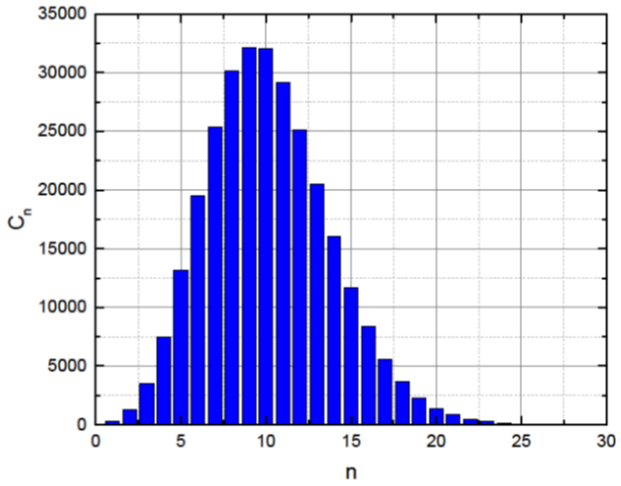

FIGURE 5.10: Test case Feynman histogram.

Each multiplet bin of the test case Feynman histogram was perturbed 0.5% in either direction, in order to obtain a set of central difference theorem sensitivities with which to compare the sensitivities calculated using Equation 5.3. As shown in Figure 5.11, the calculated sensitivities exactly match those obtained with the central difference theorem.

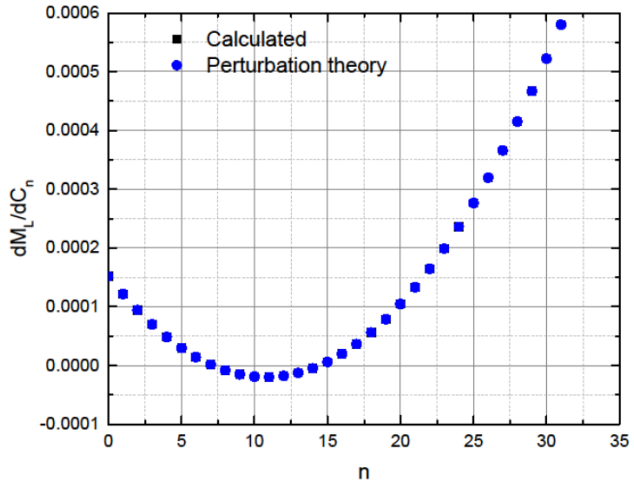

FIGURE 5.11: Sensitivities of leakage multiplication to each bin in the Feynman histogram, obtained using both Equation 5.3 and the central difference theorem.

Each multiplet bin of the test case Feynman histogram was then perturbed such that $(E_n - S_n)^2 = \sigma^2(E_n) + \sigma^2(S_n)$, while each bin of interest was successively perturbed such that $(E_n - S_n)^2 = 10(\sigma^2(E_n) + \sigma^2(S_n))$. As shown in Figure 5.12, the old FOM is not affected by which multiplet bin is perturbed by 10 times the combined uncertainties, but only by how much it is perturbed. The new FOM, however, follows the trend of sensitivity of M_L to the perturbed multiplet bins. This improved FOM will provide a better quantitative comparison between measured and simulated Feynman histograms for radiation transport code and nuclear data validation applications.

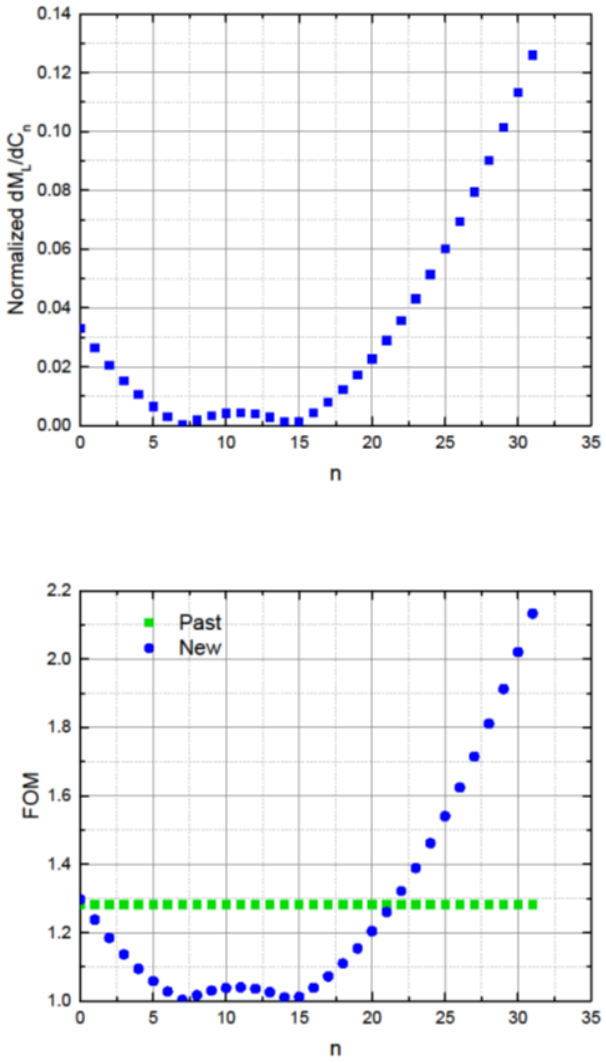

FIGURE 5.12: Trends of FOM's versus perturbed multiplet bin.

Chapter 6

Nuclear Data and Computational Methods

A genetic algorithm framework has been applied to nuclear data evaluation based on subcritical neutron multiplication inference benchmarks. A proof-of-concept demonstration was completed that results in some potential nuclear data adjustment suggestions for nuclear data evaluators. Simulations of LANL ICSBEP benchmark-quality reflected plutonium (BeRP) ball subcritical measurements have been conducted using various radiation transport codes that take into account the correlated physics of fission neutrons. Comparisons of both the results and the underlying neutron multiplicity models applied by the codes have been investigated, as well as new methods of applying comparisons of these subcritical neutron multiplication inference measurements and the associated simulations to nuclear data and computational methods validation.

6.1 Validation of the Performance of Correlated Physics of Fission Codes

Historically, radiation transport codes have uncorrelated fission emissions. In reality, both spontaneous and induced fissions release particles that are correlated in time, energy, angle, and multiplicity. For this work, the gate width is chosen such that only prompt fission neutrons are of interest, and the authors do not consider the physics of gamma production in fission. Because of their large impact on correlated neutron results, this work also compares underlying fission neutron multiplicity distributions utilized by the different codes. The goal of this portion of the work is to apply subcritical ICSBEP benchmarks to comparisons of measured correlated neutron observables, and simulated observables generated by various MC radiation transport codes that take into account various parts of the correlated physics of fission neutrons. Such comparisons will offer a type of validation that has never before been considered in nuclear data evaluation. In addition, this work investigates the effects of the different multiplicity distributions used by various MC codes on correlated neutron observables of interest and is based off of the journal publication on the topic [57].

6.1.1 Implementation of fission in transport codes

The MC radiation transport codes that this work currently compares include MCNP [53], MCNP/FREYA [87, 88], MCNP/CGMF [59], and PoliMi [89, 90]. The first few of these codes are specific releases of or options contained in the Monte Carlo N-Particle (MCNP) code, the precursors of which were originally developed during the Manhattan Project era to simulate neutron diffusion and multiplication in fissioning systems [53]. Diffusion and multiplication depend on average quantities only, and do not require modeling of the correlated physics of fission. Therefore, the correlated physics of fission was irrelevant for the Monte Carlo transport code developers at that time, and average parameters such as $\bar{\nu}$ were sufficient to simulate the fission process. However, with the increasing interest in nuclear security, safeguards, and nonproliferation, experimenters are desiring extremely accurate predictive modeling of SNM measurements. SNM has correlated fission emissions, and therefore average event treatment is not always sufficient for these applications. This work investigates various codes that are able to handle correlated fission quantities of interest, such as spontaneous and induced fission multiplicity distributions.

By default, MCNP uses a bounded integer treatment and the $\overline{\nu}$ data from ENDF (in this work, ENDF/B-VII.1 was used) to sample the number of neutrons emitted from each simulated fission event. In the bounded integer treatment, the two integers bounding $\bar{\nu}$ are the only values of ν that are sampled, instead of a complete multiplicity distribution. The FMULT card, an optional input in MCNP that allows for user definition of spontaneous and induced fission parameters, can be utilized to call either built-in or user-specified multiplicities to replace the bounded integer treatment [91]. The user can also use the FMULT card to call either the Fission Reaction Event Yield Algorithm (FREYA) or the Cascading Gamma-Ray Multiplicity with Fission (CGMF) fission event generating codes to handle fission. The FREYA fission event generator determines the number, energy, and direction of particles emitted for each fission event and gives the results to MCNP for transport. The fission event generator uses fission fragment mass and kinetic energy distributions, unbounded statistical evaporation models, and conservation of energy and momentum to generate the number, energy, and direction of neutrons released by each fission event using the Monte Carlo Weisskopf approach. The Weisskopf approach repeatedly samples emitted neutron parameters from the Weisskopf distribution, until the remaining fission fragment excitation energy is below a specified threshold. This fission fragment then releases the remaining excitation energy in the form of fission gamma rays. Equations 6.1-6.3 describes the sampling process of emitted neutrons. Equation 6.1 is used to calculate the maximum temperature of

the evaporated neutron from the Q-value for neutron emission (Q_n) and the level-density parameter of the fission fragment nucleus (a_d). The neutron kinetic energy (ϵ_n) is then sampled from Equation 6.2. Finally, the new excitation energy of the fission fragment is recalculated using Equation 6.3, and the process repeats until E_d^* falls below the specified excitation energy threshold [58, 87, 88, 92].

$$a_d T_{max}^2 = Q_n \tag{6.1}$$

$$f_n(\epsilon_n) \sim \epsilon_n exp\left(\frac{-\epsilon_n}{T_{max}}\right) \tag{6.2}$$

$$E_d^* = Q_n - \epsilon_n \tag{6.3}$$

CGMF generates prompt fission neutrons using the statistical Hauser-Feshbach formalism [59, 93], which is the primary difference between FREYA and CGMF, and gives results to MCNP for transport. The Hauser-Feshbach approach accounts for the competition between neutrons and gamma rays emitted during the fission process. It is therefore technically a more complete fission model, but significantly increases computational time. Equation 6.4 is used to sample the emitted neutron kinetic energies, and makes use of transmission coefficients (T_n) calculated using optical models. In this equation $\rho(Z, A-1, E-\epsilon_n-S_n)$ is the level density of the fission fragment nucleus after the neutron is emitted (Z is the atomic number, and A-1 is the new atomic mass), using the remaining available excitation energy (the original excitation energy E, minus the emitted neutron kinetic energy ϵ_n and the neutron separation energy S_n) [59, 87].

$$P(\epsilon_n)\, dE \propto T_n(\epsilon_n)\, \rho(Z, A-1, E-\epsilon_n-S_n) \tag{6.4}$$

PoliMi utilizes a few different built-in multiplicity sets, and also models both the anisotropy and multiplicity-dependent energy spectra of neutrons emitted in spontaneous fission. The user is able to choose which spontaneous and induced fission built-in multiplicity distributions to use, and whether or not to turn on the modeling of anisotropy in spontaneous fission sources [40, 41, 94].

6.1.2 Reflected plutonium benchmark experiments

In recent years Los Alamos National Laboratory (LANL) has performed several reflected plutonium benchmark experiments [9, 69, 85, 95]. In this study, performance of the different codes is compared using various plutonium metal benchmark cases. The growing database of subcritical neutron multiplication inference benchmark experiments includes recent benchmark experiments with the BeRP ball surrounded by copper [85], tungsten [9], and nickel [69]. Evaluations of the measurements were the first ICSBEP-accepted evaluations of measurements using the Feynman Variance-to-Mean method. These measurements were the culmination of many years of subcritical experiment research, including measurements in 2009 by Sandia National Laboratory [22, 96] which showed a marked sensitivity of subcritical leakage multiplication to the full ^{239}Pu induced fission multiplicity distribution, and indicated the possible existence of nuclear data deficiencies [5].

The available BeRP benchmark MCNP models have been adjusted to be compatible with the other codes while maintaining the original measurement geometries. The measured benchmark results are also available for comparison. The typical reflected plutonium subcritical benchmark measurement setup involves the BeRP ball surrounded by various thickness of metal reflectors, with multiplicity detectors 50 cm on either side, as shown in Figure 6.3. The BeRP-Ni benchmark geometry consists of the BeRP ball surrounded by various thicknesses of nickel reflectors, ranging from 0 in. to 3.0 in., with an NPOD detector system 50 cm away on either side, as shown in Figure 6.1. The BeRP-W benchmark consists of the BeRP ball surrounded by various thicknesses of tungsten reflectors, ranging from 0 in. to 3.0 in., with an NPOD detector system 50 cm away on either side, as shown in Figure 6.2. The NPOD consists of 15 ^{3}He neutron detectors inside a polyethylene moderator, and is a predecessor to the currently used NoMAD [9, 68, 69].

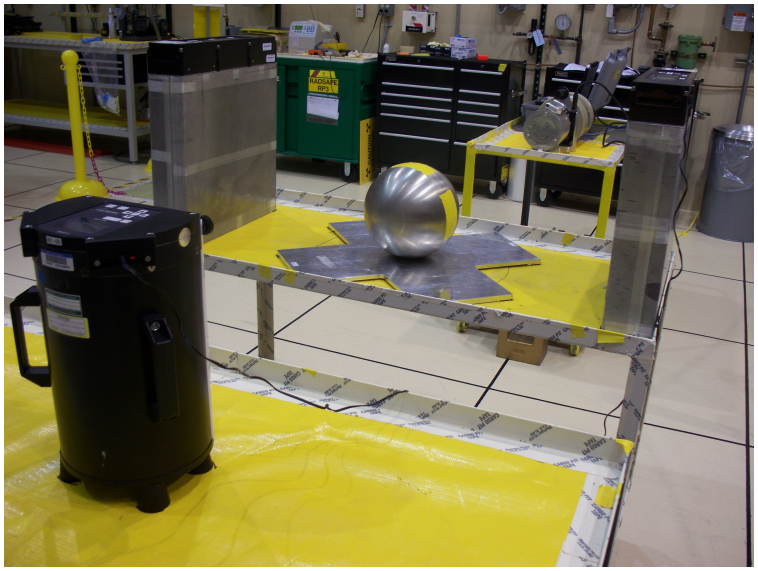

FIGURE 6.1: Picture of the BeRP-Ni benchmark experiment being conducted at NCERC.

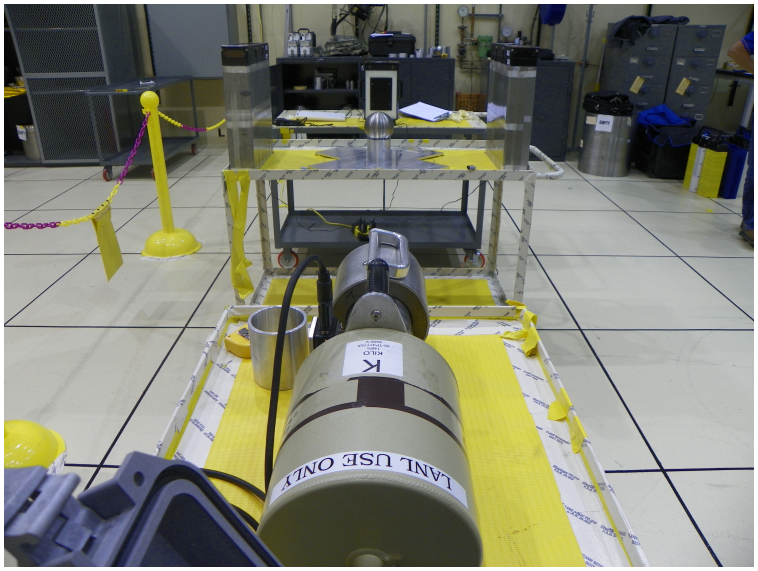

FIGURE 6.2: Picture of the BeRP-W benchmark experiment being conducted at NCERC.

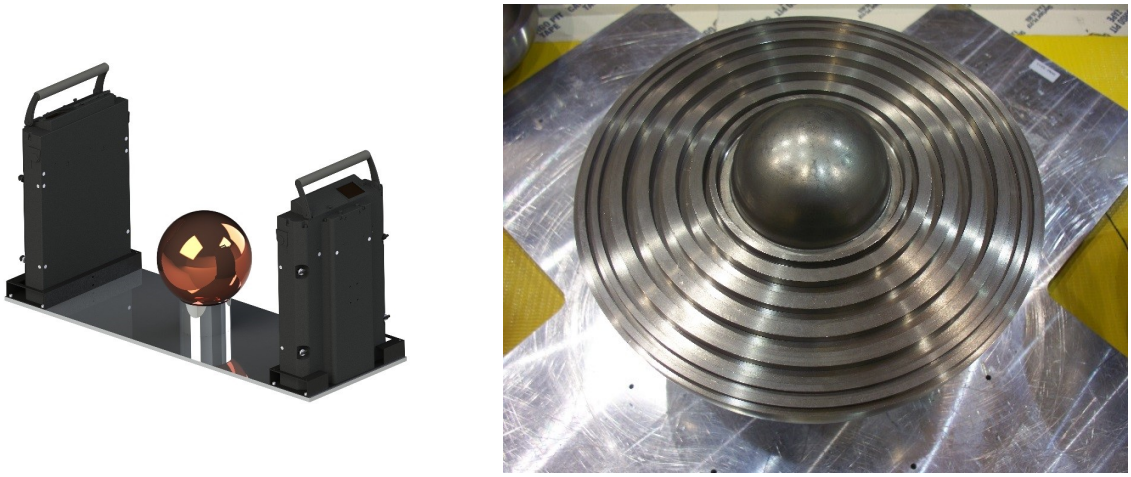

FIGURE 6.3: CAD image of a typical reflected plutonium setup (left), and picture of the BeRP ball within metal reflector shells (right).

6.1.3 Multiplicity distributions

The ^{239}Pu induced fission and ^{240}Pu spontaneous fission multiplicity distributions $P(\nu)$ used by all of the codes are investigated for comparison purposes. Because this work focuses on BeRP ball experiments, all induced fissions are assumed to be of ^{239}Pu, and all spontaneous fissions of ^{240}Pu. This assumption is valid because, at the time of both the BeRP-Ni and BeRP-W experiments, the ^{239}Pu and ^{240}Pu atomic fractions in the BeRP ball were 9.260E-01 and 5.838E-02, respectively, with the next largest actinide atomic fraction being 2.527E-03 (^{241}Am). In addition, the percentage of spontaneous fission neutrons coming from ^{240}Pu was calculated to be 98.5% [9, 69]. The singles, doubles, and Feynman histogram results are expected to be sensitive to differences in the underlying multiplicity distributions. User-defined MCNP and PoliMi distributions are obtained from Lestone [8], Santi [40], and Terrell [41]. Multiplicity distributions are specified as either a cumulative distribution function (CDF) or as a Gaussian mean ($\bar{\nu}$) and width (σ). If the distribution is given as a CDF, the probability distribution function (PDF) and mean and width are solved for. If the distribution is given as a Gaussian mean and width, the PDF is calculated. In the case of induced fission multiplicity distributions for MCNP and PoliMi, the means are obtained as a function of incident neutron energy from the nuclear data library ENDF/B-VII.1 and only the widths come from the above references. MCNP/FREYA and MCNP/CGMF $P(\nu)$, which are produced by the fission event generator of the code rather than being pulled from

a pre-existing multiplicity distribution, are extracted from the PTRAC file. The PTRAC file gives the individual ν for each fission, from which a frequency distribution is formed. The Gaussian mean and width are calculated from the frequency distribution, which is treated as a PDF.

The spontaneous and induced fission (at 2 MeV incident neutron energy) multiplicity distributions for each code were obtained from Lestone, Santi, and Terrell [8, 40, 41], as well as the ENDF/B-VII.1 library and the PTRAC output file. Figure 6.4 shows plots of the multiplicity distributions, with tabular versions of the data given in Table 6.1. 2 MeV was chosen as a representative energy for induced fission due to the fact that the average energy of neutrons causing fission in the bare BeRP system is 1.98 MeV [69]. To obtain an isolated 2 MeV induced fission multiplicity distribution for MCNP/FREYA and MCNP/CGMF, PTRAC files resulting from simulations of an isotropic 2 MeV neutron source hitting a thin film of pure ^{239}Pu were used.

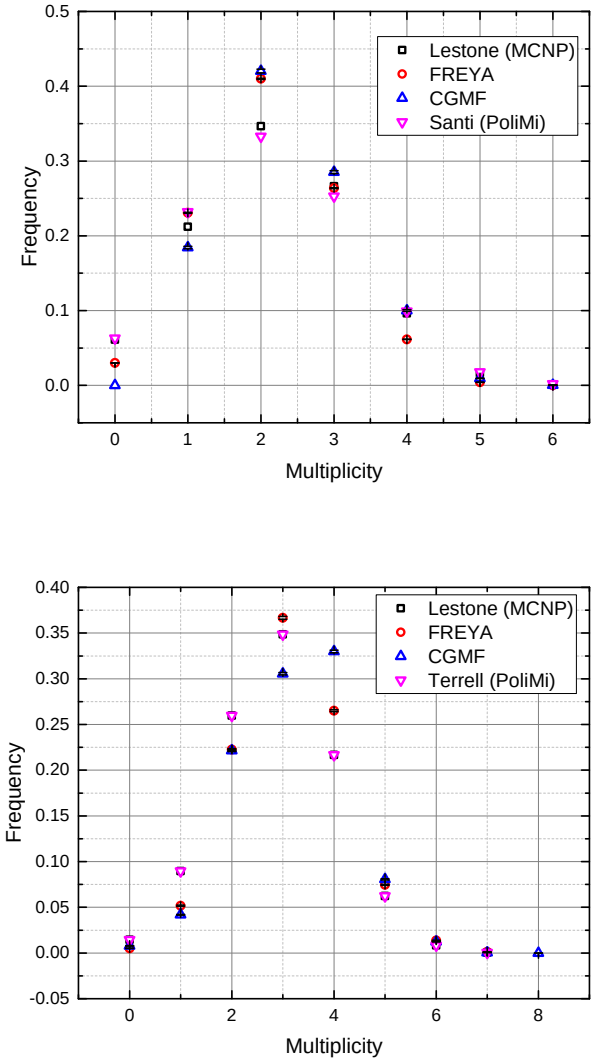

FIGURE 6.4: ^{240}Pu spontaneous fission (left) and^{239}Pu induced fission at 2 MeV incident neutron energy (right) multiplicity distributions utilized by the various codes

TABLE 6.1: ^{240}Pu spontaneous fission (SF) and ^{239}Pu induced fission (IF) multiplicity distribution parameters utilized by the various codes.

Code	SF $\bar{\nu}$	SF σ	IF $\bar{\nu}$	IF σ
MCNP	2.151 (Lestone)	1.151 (Lestone)	3.178 (ENDF)	1.140 (Lestone)
MCNP/FREYA	2.109	0.942	3.128	1.057
MCNP/CGMF	2.225	0.949	3.202	1.191
PoliMi	2.093 (Santi)	1.199 (Santi)	3.178 (ENDF)	1.140 (Terrell)

Table 6.1 shows that the first moment the spontaneous fission multiplicity distribution is significantly higher for CGMF compared to all of the other codes, while the first moment of the induced fission multiplicity distribution is significantly lower for FREYA. In addition, the standard deviation of the spontaneous fission multiplicity distributions are much higher for Lestone and Santi than for the fission event generators (FREYA and CGMF), while the standard deviations of the induced fission multiplicity distribution are more clustered together. Differences in $P(\nu)$ are likely a cause of discrepancies in Feynman histograms and doubles rates. Singles rates are expected to change only with the mean of the multiplicity distribution, $\bar{\nu}$, rather than with both the mean and the width (standard deviation), σ. This behavior is expected because the singles and doubles rates depend on the first and second factorial moments of the binned list-mode data, respectively.

6.1.4 Effect of neutron multiplicity distribution assumptions

As previously mentioned, the width σ of the induced fission multiplicity distribution, $P(\nu)$, is typically assumed to remain constant with incident neutron energy. However, in reality it does vary slightly with energy. As will be elaborated upon in the description of the machine learning algorithm for nuclear data evaluation developed as part of this work, the sensitivities of various subcritical neutron multiplication inference observables of interest were calculated by perturbing the induced fission multiplicity distribution width as defined in the MCNP FMULT card. The sensitivities for R_1, R_2, and M_L for the BeRP-Ni benchmark are plotted in Figure 6.5.

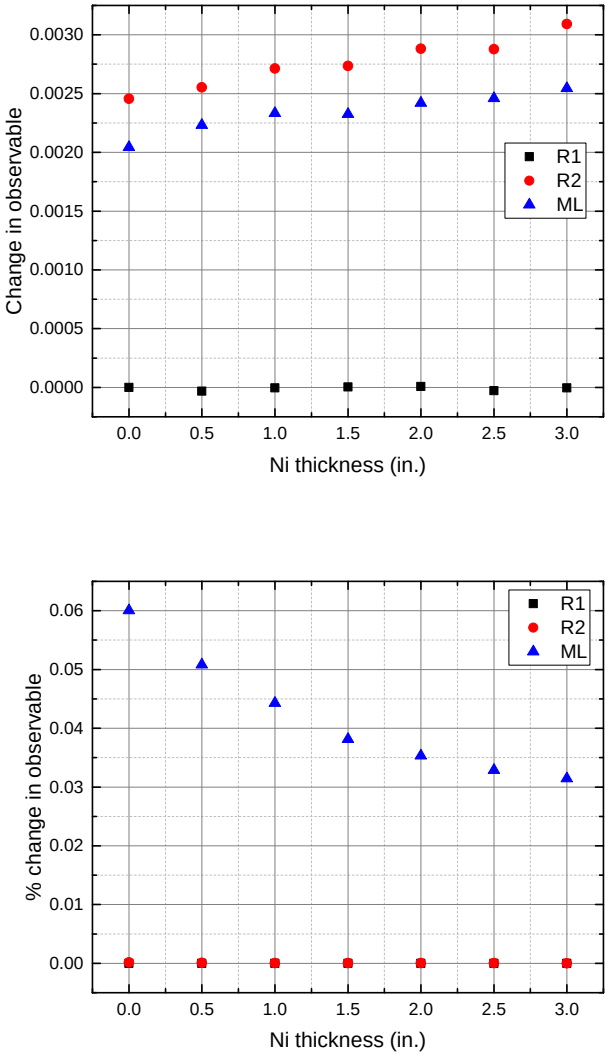

FIGURE 6.5: Absolute and relative changes in observables of interest as a result of a 1% perturbation in the width of the induced fission multiplicity distribution, using a reference width of 1.140.

Figure 6.6 shows the variation of induced fission σ as a function of incident neutron energy for a few representative energies, which were obtained by fitting a Gaussian to the $P(\nu)$ distributions tabulated for ^{239}Pu in the new ENDF/B-VIII.0 release description [1].

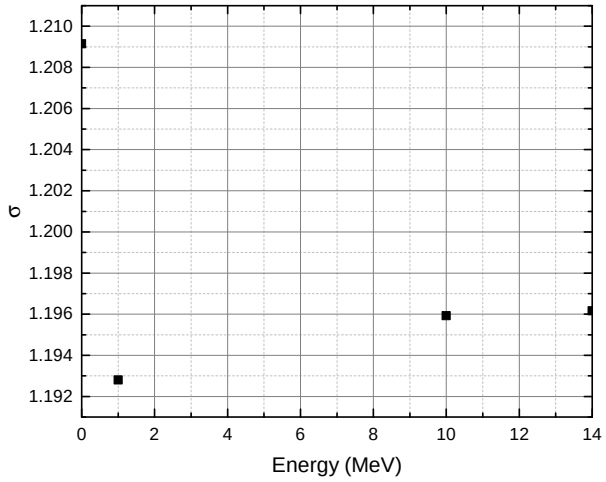

FIGURE 6.6: Variation of induced fission σ as a function of incident neutron energy.

Assuming, based on the data plotted in Figure 6.6, that the maximum σ over the incident neutron energy range up to 14 MeV will be 1.2091, the effect on the variation in induced fission multiplicity distribution width over this wide range of energies on the observables of interest can be estimated. Using the sensitivities plotted in Figure 6.5 and the reference value of 1.140, the percent changes in observables of interest resulting from a deviation to the maximum σ value were calculated for the BeRP-Ni benchmark configurations. These are plotted in Figure 6.7. All values in Figure 6.7 are below 0.004% and are therefore considered to be negligible.

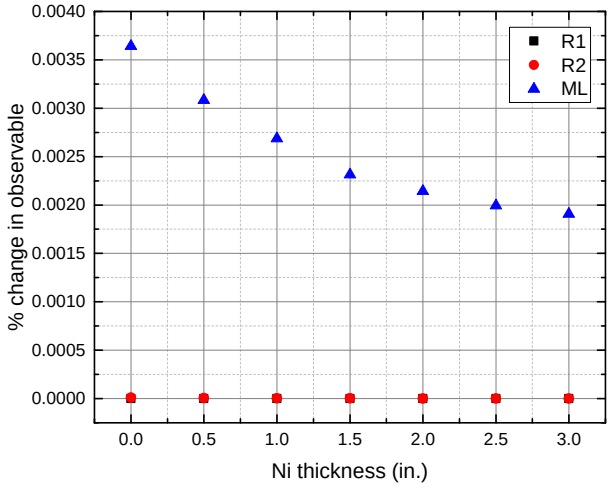

FIGURE 6.7: Percent changes in observables of interest resulting from a deviation to the maximum σ value given in ENDF/B-VIII.0.

6.1.5 Uncertainty and correlation analysis

Uncertainties associated with the multiplicity distributions obtained from simulation output files are calculated using Poisson counting statistics (because radioactive decay is a Poissonian process, the predicted standard deviation can be calculated as the square root of the experimental mean [2]). The uncertainty associated with each possible number of neutrons emitted during fission is equal to the square root of the number of times the given number of neutrons was emitted in the simulation. Feynman histogram uncertainties are also calculated using Poisson counting statistics. The uncertainty associated with each bin in the histogram is equal to the square root of the number of multiplets in the given bin. Reference [35] contains equations for the uncertainties in R_1, R_2, and M_L. All uncertainties for other derived quantities (such as (C-E)/E) are calculated using standard uncertainty propagation, according to Equation 6.5.

$$\sigma_z^2 = \left(\frac{\delta z}{\delta x}\right)^2 \sigma_x^2 + \left(\frac{\delta z}{\delta y}\right)^2 \sigma_y^2 + ... \tag{6.5}$$

In order to investigate the existence of correlation between different observables and nuclear

data items of interest, the Pearson correlation coefficient was used. Equation 6.6 is used to calculate the sample Pearson correlation coefficient. If $r = -1$, $r = 0$, or $r = 1$, then x and y are considered to be completely anti-correlated, completely uncorrelated, or completely correlated, respectively. As applied to this work, each sample consists of a single observable and single nuclear data item for a single configuration of a single benchmark experiment, across all of the different radiation transport codes being compared.

$$r = \frac{\sum_{i=1}^{n}(x_i - \bar{x})(y_i - \bar{y})}{\sqrt{\sum_{i=1}^{n}(x_i - \bar{x})^2}\sqrt{\sum_{i=1}^{n}(y_i - \bar{y})^2}} \tag{6.6}$$

As applied to this work, in Equation 6.6, n is the number of codes being compared, x_i is the value of a single observable of interest for the i$^{\text{th}}$ code, y_i is the value of a single nuclear data item of interest for the i$^{\text{th}}$ code, $\bar{x}$ is the mean of all values of x, and $\bar{y}$ is the mean of all values of y. Because this work includes 3 observables of interest (R_1, R_2, and M_L), 4 nuclear data items of interest (SF and IF $\bar{\nu}$ and σ), and 8 different configurations of the BeRP-W benchmark, 96 values of r exist.

6.1.6 Results

Figure 6.8 shows induced fission multiplicity distributions for a few representative configurations of the BeRP-W benchmark for MCNP, MCNP/FREYA, MCNP/CGMF, and PoliMi. Appendix C contains multiplicity distributions for all other BeRP-W configurations. The induced fission multiplicity distributions include all incident neutron energies and are obtained from the PTRAC output files for MCNP based codes, and the collision output file for PoliMi. The multiplicity distribution mean ($\bar{\nu}$) and width (σ) values in Table 6.2 were obtained using the statistical definitions of mean and standard deviation. Error bars are present in all results plots, but may be too small to be visible.

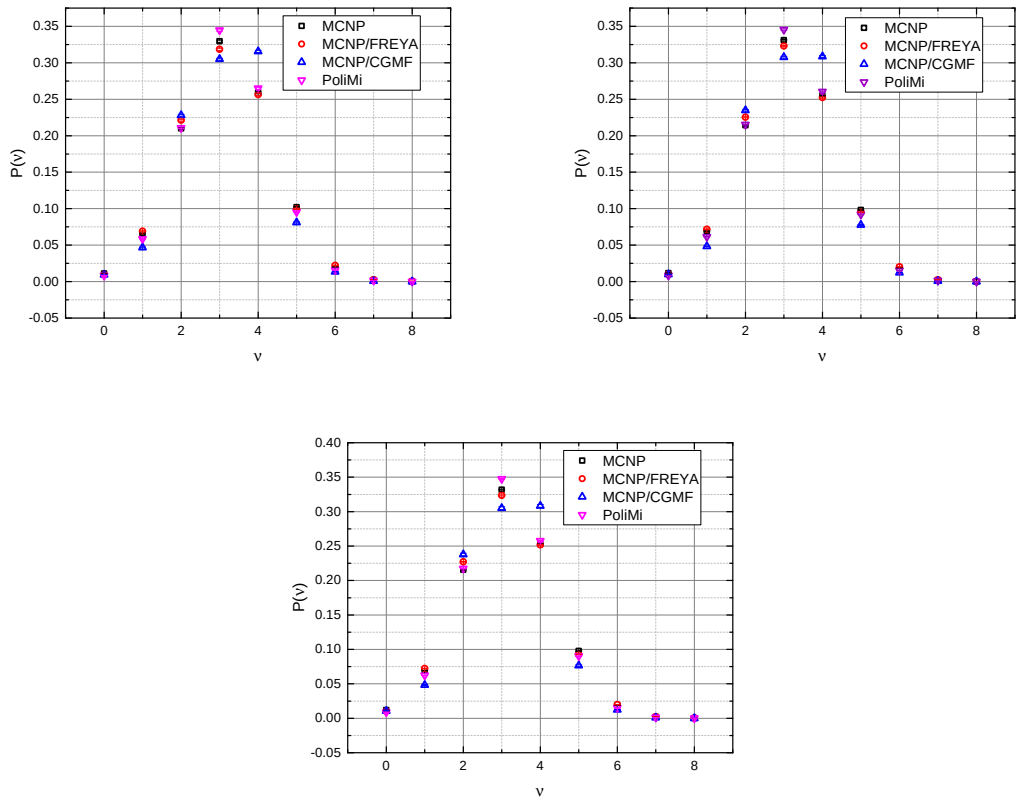

FIGURE 6.8: ^{239}Pu induced fission multiplicity distributions for 0 (left), 1.5 (middle), and 3.0 (right) in. W thickness.

TABLE 6.2: ^{239}Pu induced fission multiplicity distribution parameters for 0, 1.5, and 3.0 in. W thickness.

Code	$\bar{\nu}$	σ	$\bar{\nu}$	σ	$\bar{\nu}$	σ
W thickness (in.)	0	0	1.5	1.5	3.0	3.0
MCNP	3.16	1.43	3.13	1.43	3.12	1.43
MCNP/FREYA	3.15	1.47	3.12	1.45	3.10	1.44
MCNP/CGMF	3.17	1.25	3.14	1.24	3.14	1.25
PoliMi	3.16	1.31	3.13	1.31	3.12	1.31

As expected, the widths of the MCNP and PoliMi distributions do not change for different energies (reflector thicknesses). Overall, the means decrease slightly with decreasing energy, as do the widths for MCNP6/FREYA and MCNP6/CGMF. The multiplicity distributions do not vary much for the different reflector thicknesses because the neutron energy spectrum remains quite fast for all configurations. Between codes $P(\nu)$ is quite similar, with most discrepancies being located towards the center of the distribution.

Feynman histograms, singles rates R_1, doubles rates R_2, and leakage multiplication M_L are compared between the various codes for all BeRP-Ni and BeRP-W benchmark configurations. All results are calculated using a gate width of $\tau = 1000\,\mu s$.

Figure 6.9 shows Feynman histograms for a few representative BeRP-Ni configurations. Appendix D contains Feynman histograms for all other BeRP-Ni configurations. All histograms are plotted on the same axes to make trends as a function of reflector thickness easier to observe. Measured results are also shown for comparison. Tables 6.3 present FOM values, calculated according to Equation 5.4 [86], to quantify the discrepancy between the measured and various simulated Feynman histograms.

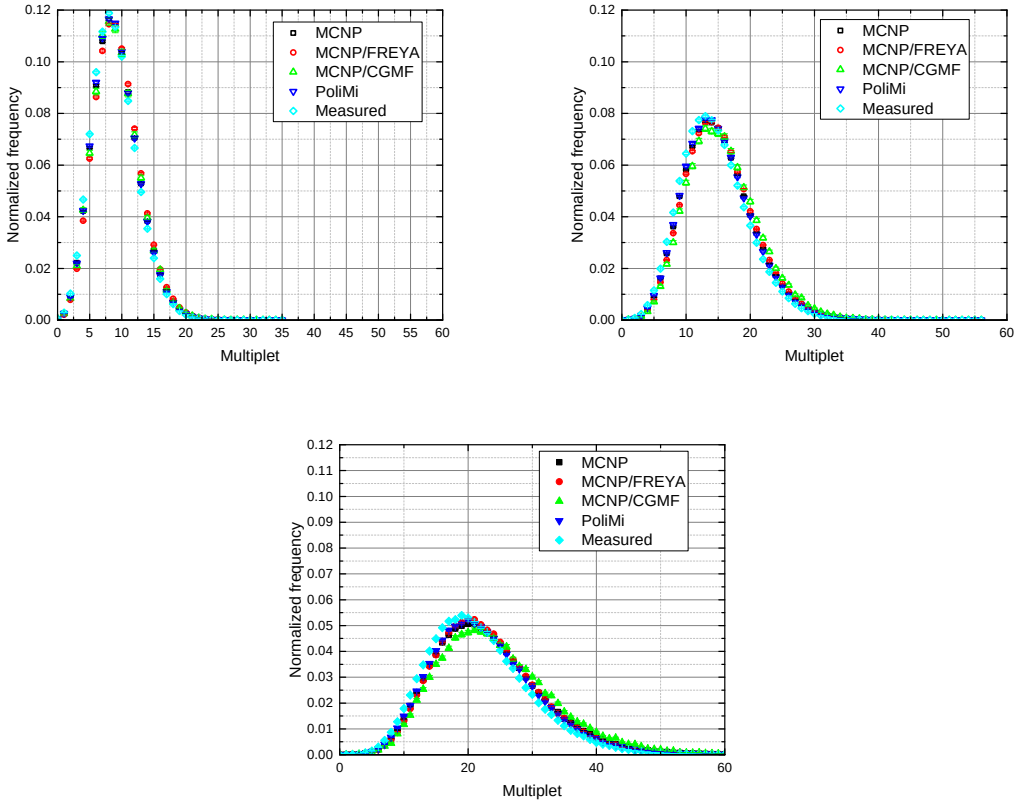

FIGURE 6.9: Feynman histograms for 0 (left), 1.5 (middle), and 3.0 (right) in. Ni thickness.

TABLE 6.3: FOM values for the various simulated Feynman histograms, as compared to the measured histogram, for 0, 1.5, and 3.0 in. Ni thickness.

Code	0 in. Ni thickness	1.5 in. Ni thickness	3.0 Ni thickness
MCNP	24	39	38
MCNP/FREYA	82	55	32
MCNP/CGMF	5.9	24	24
PoliMi	19	25	24

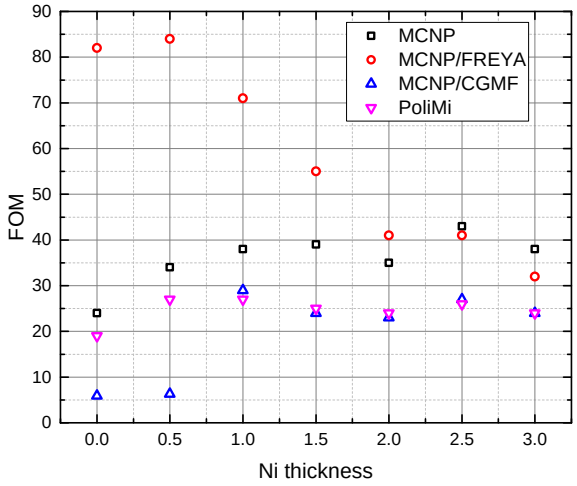

FIGURE 6.10: Feynman histogram FOM values for all codes and all Ni thicknesses.

The tabulated FOM values, which Figure 6.10 shows in plot form, indicate that according to this metric MCNP/CGMF performs the best for almost all nickel thicknesses (for the 1 in. reflected configuration MCNP/CGMF shows slightly worse performance than PoliMi). PoliMi shows the next best performance, followed by MCNP. Finally, MCNP/FREYA shows the worst performance according to this FOM, especially at smaller (0-1.5 in.) reflector thicknesses. The MCNP/FREYA FOM values show a clear downward trend between 0.5 and 2.0 in. nickel thickness.

Figures 6.11 and 6.12 are plots of singles and doubles rates.

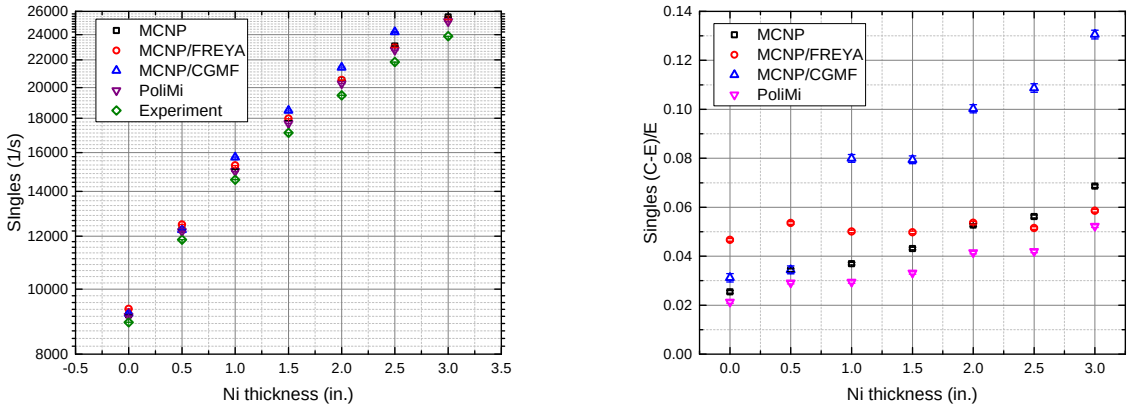

FIGURE 6.11: Singles rates for all BeRP-Ni configurations.

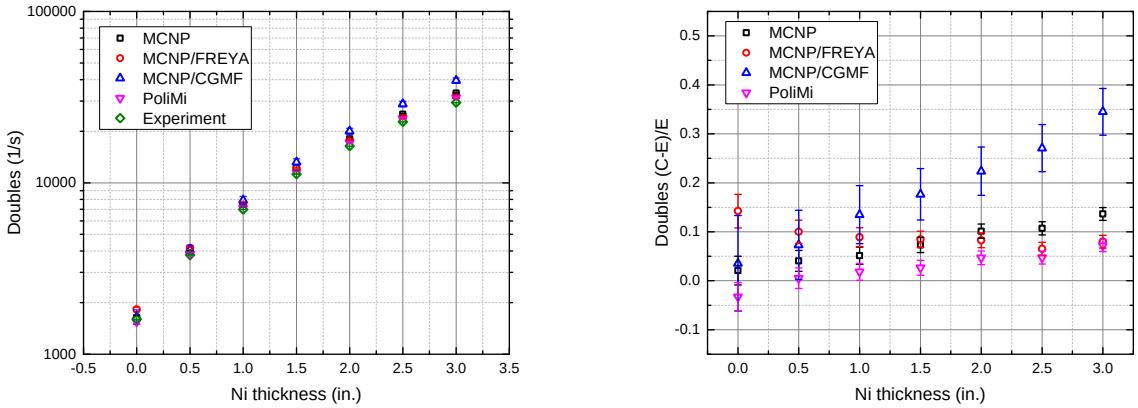

FIGURE 6.12: Doubles rates for all BeRP-Ni configurations.

Overall, PoliMi seems to show the best match to experimental singles and doubles results, while MCNP/CGMF shows the most deviation from experimental results. MCNP performance seems to worsen as a function of nickel thickness, while MCNP/FREYA shows the opposite trend.

Figure 6.13 plots leakage multiplication for the various BeRP-Ni configurations.

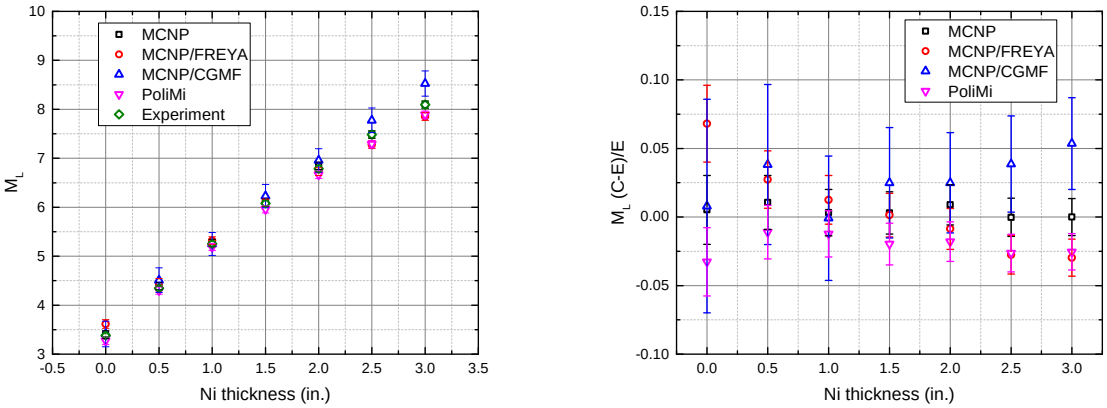

FIGURE 6.13: Leakage multiplication for all BeRP-Ni configurations.

Unlike with singles and doubles rates, MCNP shows the best agreement with leakage multiplication. PoliMi shows a consistent under-bias in leakage multiplication, while MCNP/CGMF shows a consistent over-bias. MCNP/FREYA performance seems to improve with increasing nickel thickness, and then begin to worsen again after 1.5 in. of nickel reflection.

Figure 6.14 shows Feynman histograms for a few representative BeRP-W configurations. Appendix D contains Feynman histograms for all other BeRP-W configurations. All histograms are plotted on the same axes to make trends as a function of reflector thickness easier to observe. Measured results are also shown for comparison. Table 6.4 presents FOM values to quantify the discrepancy between the measured and various simulated Feynman histograms.

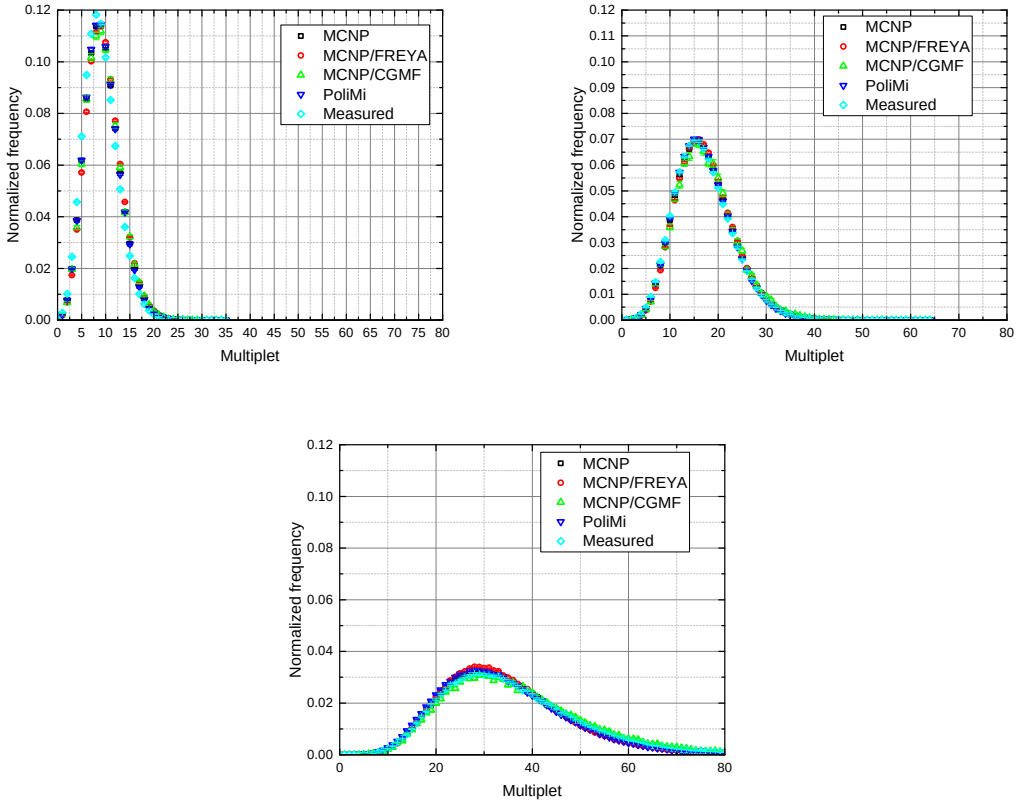

FIGURE 6.14: Feynman histograms for 0 (left), 1.5 (middle), and 3.0 (right) in. W thickness.

TABLE 6.4: FOM values for the various simulated Feynman histograms, as compared to the measured histogram, for 0, 1.5, and 3.0 in. W thickness.

Code	0 in. W thickness	1.5 in. W thickness	3.0 in. W thickness
MCNP	88	1.8	1.1
MCNP/FREYA	190	4.9	5.8
MCNP/CGMF	19	3.0	2.5
PoliMi	78	1.8	4.8

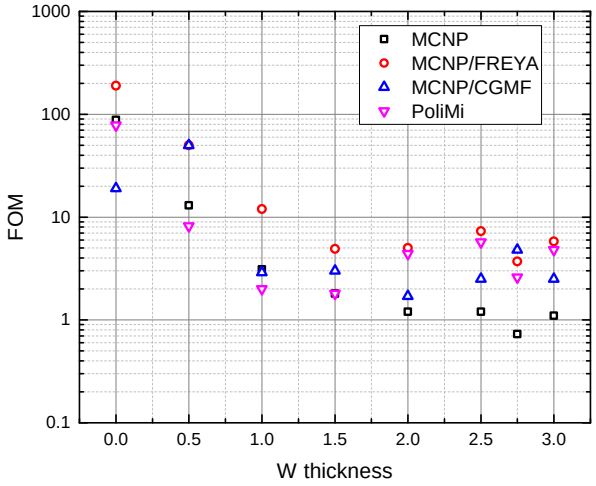

FIGURE 6.15: Feynman histogram FOM values for all codes and all W thicknesses.

Except for the poorer code performance for the small reflector thickness configurations, the tabulated FOM values, which Figure 6.15 shows in plot form, are quite good (<10) and very close together. For 1.5-3 in. W reflector thickness, MCNP shows the best performance, followed by PoliMi for 1.5-2 in. W thickness and MCNP/CGMF for 2.5-3 in. W thickness. MCNP/FREYA shows the worst performance, according to this FOM, for all configurations.

Figures 6.16 and 6.17 are plots of singles and doubles rates.

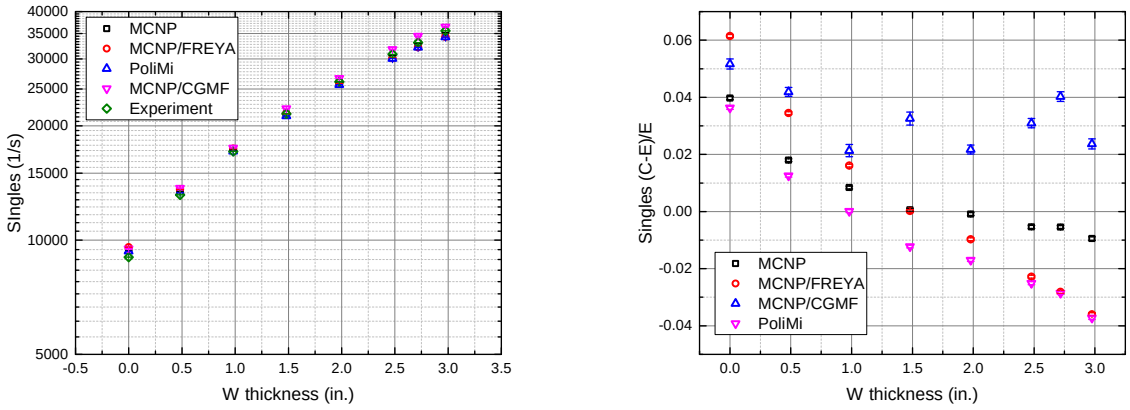

FIGURE 6.16: Singles rates for all BeRP-W configurations.

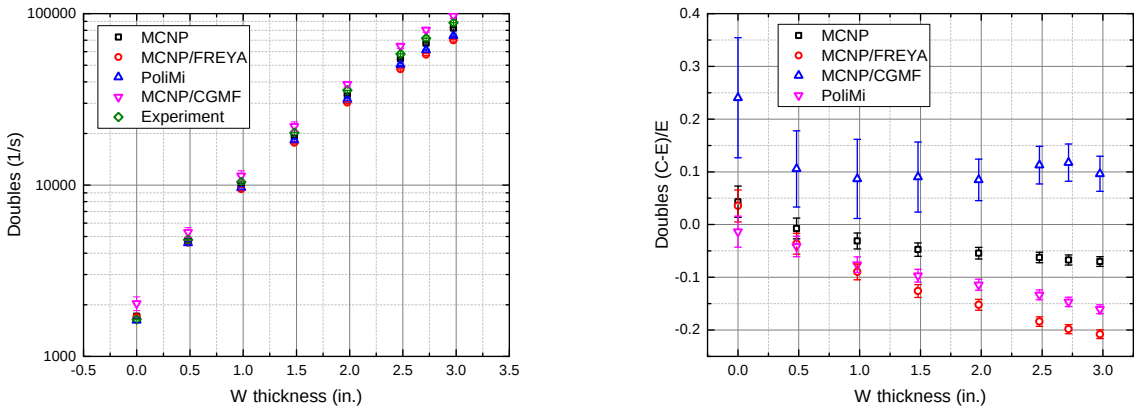

FIGURE 6.17: Doubles rates for all BeRP-W configurations.

MCNP seems to show the best agreement with measured singles and doubles rates for cases with thick tungsten reflection. MCNP/CGMF is the most discrepant from measured singles rates, but similar in deviation from experiment to both PoliMi and MCNP/FREYA for doubles rates. MCNP/CGMF has a consistent over-bias in both singles and doubles rates, while PoliMi and MCNP/FREYA show consistent under-biases in doubles rates.

Figure 6.18 plots leakage multiplication for the various BeRP-W configurations.

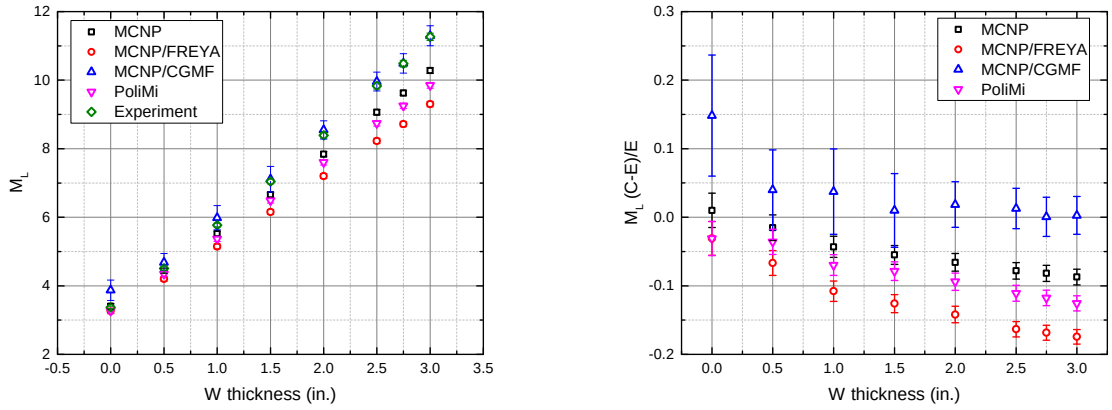

FIGURE 6.18: Leakage multiplication for all BeRP-W configurations.

MCNP/CGMF shows the best agreement with experimental leakage multiplication data. MCNP shows the next best agreement, followed by PoliMi, and then MCNP/FREYA. MCNP, PoliMi, and MCNP/FREYA all show significant under-bias for predicting interred leakage multiplication.

6.1.7 Correlations between nuclear data and observables

Correlations are observed to exist between differences in the multiplicity distribution nuclear data (induced and spontaneous fission $\bar{\nu}$ and σ) used by or extracted from the various codes, and differences in observables of interest (R_1,R_2, and M_L). As previously mentioned, 96 Pearson correlation coefficients exist over all configurations of the BeRP-W benchmark. These are plotted in Appendix E. The coefficients showing the largest correlations (defined as a correlation or anti-correlation value above 90%) are plotted in Figure 6.19.

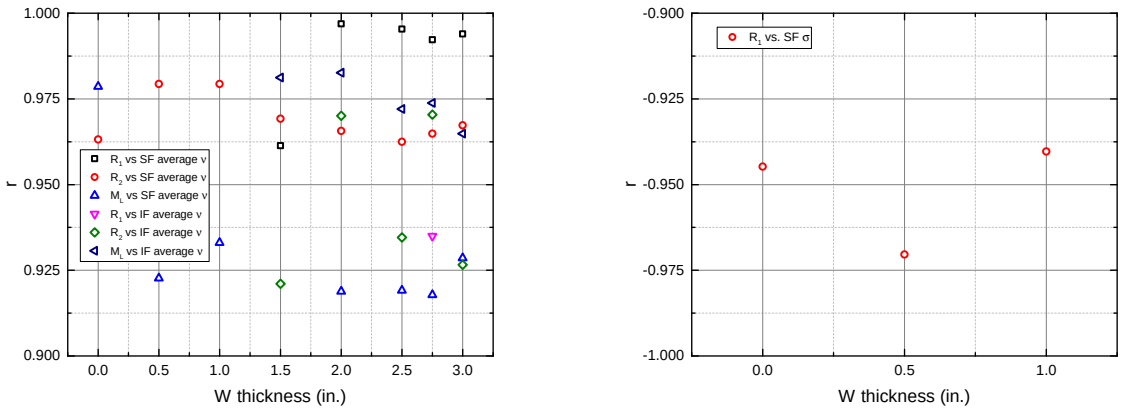

FIGURE 6.19: Pearson correlation coefficient "r" plotted for the most highly correlated combinations of observables and nuclear data items of interest, across all configurations of the BeRP-W benchmark.

The strongest correlations are between R_1, R_2, and M_L, and both SF and IF $\bar{\nu}$, especially for the highly reflected configurations. The strongest anti-correlations are between R_1 and SFσ, for the less reflected configurations. The observed correlations between multiplicity

distribution nuclear data and observables of interest may aid in future subcritical benchmark experiment design, by allowing experimenters to focus on observables that seem most sensitive to the nuclear data quantity of interest.

6.2 Genetic Algorithm for Nuclear Data Evaluation

The observables of interest in subcritical benchmarks are sensitive to the distribution of the number of neutrons emitted in fission. Neutron multiplicity distributions are represented as $P(\nu)$ and characterized by and σ. For spontaneous fission, $\bar{\nu}(E)$ simplifies to $\bar{\nu}$. The standard deviation is typically assumed to remain relatively constant across all incident neutron energies. Previous work in this area has focused on randomly (rather than intelligently, as in an optimization algorithm framework) perturbing $\bar{\nu}(E)$ in both an energy-independent and energy-dependent manner in order to produce improved Feynman histograms [97, 98]. The results of the energy-independent perturbations show that improvement in subcritical benchmark simulation performance worsens critical benchmark simulation performance. Energy-dependent perturbations did produce improvement in subcritical simulation performance with relatively minor worsening of critical simulation performance, but the suggested changes in $\bar{\nu}(E)$ as a function of energy reduced the smoothness of the curve, and were not adopted in the latest nuclear data evaluation. The nuclear data evaluation field strives to maintain consistency with the fundamental physics underlying nuclear data, and the physics underlying the fission reaction suggests smooth variation of $\bar{\nu}(E)$ as a function of incident neutron energy. In this work, a genetic algorithm for nuclear data evaluation has been developed and applied to subcritical benchmark measurements focusing on adjustments in nuclear data parameters that affect only the subcritical benchmark simulations. Because of the known high sensitivity of subcritical benchmark measurements to ^{239}Pu $\bar{\nu}(E)$ [9, 61], $\bar{\nu}(E)$ was also varied in an energy-independent manner. In order to allow for maximum flexiblity in the structure of the algorithm, a pre-existing algorithm was not used.

In the aspects of using nuclear data parameters as inputs, observables of interest (such as k_{eff}, or the moments of the Feynman histogram) as outputs, and feeding in sensitivities obtained from central difference method calculations, the work presented here is very similar to the commonly used methods for nuclear data evaluation and adjustment [99]. However, modern optimization methods such as the genetic algorithm are inherently more flexible than classical techniques such as the general linear least squares method typically used for nuclear data evaluation applications, and therefore can add another complementary method that is able to take into account larger and more diverse datasets. The following discussion is based on the submitted journal paper on the topic [100].

6.2.1 Theory

A genetic algorithm is a type of evolutionary optimization algorithm. The principles of a genetic algorithm framework are based on Darwinian evolution and survival of the fittest. Fitness, survival, and reproduction are applied to datasets in order to converge upon an optimized solution. Typically mutation is involved to prevent the algorithm from falling into a local minimum or maximum, and convergence is usually defined as the point at which the fitness of successive generations of data no longer improve at a certain minimum rate.

A typical genetic algorithm framework begins with randomly sampling an initial population with N members. Each member of the population is a datum point, or data set. A fitness function is then defined to evaluate the fitness of each member of the population. It is up to the user to decide how to represent the genetic material of each member of the population in data form, and how to quantitatively calculate fitness. Once the fitness of each member of the initial population is evaluated, reproduction occurs. The algorithm should be set up such that more fit members of the population are more likely to reproduce and pass their genetic material on to the next generation. This aspect is the optimization aspect of the algorithm. Again, it is up to the user to choose how to select parents and how to carry out reproduction. Reproduction can be carried out via cloning of the fittest members of the population, traditional 2 parent reproduction without replacement, 2 parent reproduction with replacement, etc. Each set of parents can produce one or multiple offspring. The actual gene combination process is again up to the user and depends on the form of the data being reproduced. A mutation probability is typically introduced during the reproduction process. This mutation probability adds more genetic variation into the population and aids in avoiding local minima or maxima.

After the second generation is created, the algorithm continues to iterate until the convergence criteria are reached. One iteration involves calculating the fitness of each member of the new population, selecting parents as a function of fitness, carrying out reproduction and mutation, and producing the next generation. Convergence criteria can include any number of requirements, such as a certain number of generations, a certain fitness level of overall population or the most fit member of the population, or a minimum level of change between succeeding generations. Once the convergence criteria are met, the algorithm terminates and the most fit member of the final generation is output as the optimized solution.

It is clear from the above discussion that a genetic algorithm is a very general framework,

with specifics that can vary widely across different applications and must be tailored to the problem the user wishes to apply it to. Genetic algorithms have been applied to other areas in the field of nuclear engineering, such as reactor design optimization [101, 102], optimization of multigroup neutron cross-section structure [103], reactor loading pattern optimization [104, 105], and others [106]. The following section describes how the genetic algorithm framework has been applied to nuclear data evaluation adjustment, using subcritical benchmark experiments.

6.2.2 Methods

The typical reflected plutonium subcritical benchmark measurement setup involves the BeRP ball surrounded by various thickness of metal reflectors, with multiplicity detectors 50 cm on either side. The BeRP-Ni benchmark geometry consists of the BeRP ball surrounded by various thicknesses of nickel reflectors, ranging from 0 in. to 3.0 in., with a LANL ^{3}He multiplicity detector (NPOD) 50 cm away on either side. The BeRP-W benchmark consists of the BeRP ball surrounded by various thicknesses of tungsten reflectors, ranging from 0 in. to 3.0 in., with an NPOD 50 cm away on either side. The SCRαP benchmark consists of the BeRP ball surrounded by various thicknesses and combinations of copper and high-density polyethylene (HDPE) reflectors, with a NoMAD 47 cm away on either side. The NPOD is a predecessor to the currently used NoMAD [9, 61, 68].

Neutron multiplicity measurements record list-mode data, which consist only of the time of neutron detection and the tube in which the detection occurred. The list-mode data can be used for many different types of multiplicity analysis methods; for this work the data was analyzed with the Hage-Cifarelli formalism based on the Feynman Variance-to-Mean method [62]. The list-mode data are binned into Feynman histograms according to specified time widths.

The magnitude of the n^{th} bin of the Feynman histogram at the specified time width τ is represented by the variable $C_n(\tau)$ in Equation 6.7. Equation 6.8 defines $m_r(\tau)$ as the r^{th} reduced factorial moment of the Feynman histogram [35].

$$p_n(\tau) = \frac{C_n(\tau)}{\sum_{n=0}^{\infty} C_n(\tau)} \tag{6.7}$$

$$m_r(\tau) = \frac{\sum_{n=0}^{\infty} n\,(n-1)\ldots(n-r+1)\,p_n\,(\tau)}{r!} \tag{6.8}$$

The MCNP transport code is used to produce all simulated results discussed in this work. The PTRAC output of MCNP is processed to obtain list-mode data, in the same format as the measured list-mode data. The simulated list-mode data is then processed using the exact same method as the measured list-mode data. The FMULT card in MCNP makes it possible to change the spontaneous fission multiplicity distribution mean, $\bar{\nu_S}$, and width, σ_S, as well as the induced fission multiplicity distribution width, σ_I. All other nuclear data comes from the ENDF/B-VII.1 nuclear data library at room temperature [107]. The spontaneous fission multiplicity distribution mean $\bar{\nu_S}$ was chosen because it is known to have a large effect on subcritical benchmark observables of interest [9, 61]. The combination of fission multiplicity distribution parameters $\bar{\nu_S}$, σ_S, and σ_I were chosen specifically because they affect only the subcritical benchmark simulations, as opposed to affecting both subcritical and critical benchmark simulations, and because both the spontaneous and induced fission multiplicity parameters are known to have large effects on subcritical benchmark observables of interest. In addition, $\bar{\nu_I}$ was varied energy-independently alongside $\bar{\nu_S}$, σ_S, and σ_I because it is known that ^{239}Pu will be the most sensitive nuclide for criticality calculations.

The genetic algorithm systematically adjusts neutron spontaneous and induced fission multiplicity distribution parameters to converge upon a solution that yields the largest improvement in (C-E)/E values for the first (m_1) and second (m_2) factorial moments of the Feynman histogram, across various subcritical neutron multiplication inference benchmarks. In this notation, C represents the simulated value of the observable of interest, and E represents the measured value. For this specific application to BeRP ball benchmarks, spontaneous fission refers to that of ^{240}Pu, and induced fission to that of ^{239}Pu.

The genetic algorithm begins by using Gaussian sampling of the currently used nuclear data values and uncertainties to create an initial population of N members. Each member of the population contains a value for the spontaneous fission multiplicity distribution mean, $\bar{\nu_S}$, and width, σ_S, as well as the induced fission multiplicity distribution width, σ_I. It was also made possible to add a value for the induced fission multiplicity distribution mean, $\bar{\nu_I}$, to each member of the population. Then, the fitness of each member of the population is calculated according to Equation 6.9, summed over all configurations of the BeRP-Ni, BeRP-W, and SCRαP benchmarks. The ideal fitness value is 0. This fitness function gives equal weighting

to (C-E)/E values for m_1 and m_2, but coefficients could be added to apply more weight to one of the observables. The results section of this work will explain the reasoning behind using equal weighting.

$$\sum|\frac{C-E}{E}|_{m_1} + \sum|\frac{C-E}{E}|_{m_2} \tag{6.9}$$

These new (C-E)/E values are calculated by using both the original (C-E)/E values and pre-determined sensitivities, such as $\frac{\partial\left(\frac{C-E}{E}\right)_{m_1}}{\partial\bar{\nu}_S}$, for the various observables and nuclear data parameters of interest. The pre-determined sensitivities are calculated according to the central difference method, using 20 times the uncertainty of the nuclear data parameter as the perturbation size. This size of perturbation was chosen after testing many perturbation sizes. 20 standard deviations appeared to be the smallest perturbation at which the sensitivities of the observables of interest to the nuclear data parameters of interest had reached the asymptotic value. Finally, the reproduction of the fittest members of the population is carried out in order to produce the next generation of nuclear data values. Reproduction is conducted by averaging the various nuclear data values of the 2 parents chosen to reproduce (probability of reproduction increases with decreasing fitness value) to create a single offspring. Reproduction is carried out N times to create the next generation of N members. A small mutation probability is also included with each reproduction, so as to introduce more genetic variability into the population and avoid falling into local minima.

The optimized solution of the genetic algorithm is then the member of the population that has the minimum (best) fitness value at the time of convergence. The convergence criteria is set such that the algorithm terminates when the variation of the fitness of the most fit member of the population falls below a certain value, or a minimum number of generations have been produced, whichever occurs last. The improvement is then defined as the percentage decrease from the original fitness value (sum of the absolute values of all original (C-E)/E values) to the fitness value of the solution of the optimized nuclear data parameters. The various genetic algorithm parameters used in this application are listed in Table 6.5.

TABLE 6.5: Genetic algorithm parameters.

Parameter	Value
Population size	1000
Mutation rate	10%
Convergence criterion	0.00001%
Minimum generations	100
$\bar{\nu}_S$	2.151 +/- 0.005
σ_S	1.151 +/- 1%
σ_I	1.140 +/- 1%
$\bar{\nu}_I$ (2 MeV)	3.1780 +/- 0.009

The genetic algorithm parameters in Table 6.5 (excepting the nuclear data values, which were taken from the FMULT cards of the detailed benchmark MCNP input files) were chosen after testing the performance of the algorithm for various combinations of different values for each parameter, and determining the combination of parameter values that yielded the combined best improvement and fastest convergence. The value and uncertainty of $\bar{\nu}_I$, as well as the uncertainty on $\bar{\nu}_S$, were obtained from the ENDF/B-VII.1 nuclear data library, although the uncertainty for $\bar{\nu}_S$ should really be approximately double that value due to the correlation between the uncertainties on $\bar{\nu}_S$ for ^{240}Pu and ^{252}Cf. ^{240}Pu $\bar{\nu}_S$ uncertainty must be at least as large as that of ^{252}Cf, since ^{252}Cf $\bar{\nu}_S$ is used to obtain ^{240}Pu $\bar{\nu}_S$ [108]. Because uncertainties on the widths of the neutron fission multiplicity distributions (σ_S and σ_I) do not currently exist within ENDF, uncertainties of 1% of the mean were assumed.

6.2.3 Results and analysis

The genetic algorithm for nuclear data evaluation has been tested and proven to show good improvement in (C-E)/E values with reasonable adjustments in neutron fission multiplicity distribution parameters, using the aforementioned BeRP-Ni, BeRP-W, and SCRαP benchmarks. Tables 6.6 and 6.7 list the naming conventions for the various configurations of the different benchmarks. The algorithm was run for $\bar{\nu}_S$, σ_S, and σ_I; $\bar{\nu}_S$ alone; and $\bar{\nu}_S$, σ_S, σ_I, and $\bar{\nu}_I$. The algorithm was run in both an unconstrained and constrained fashion, in terms of the number of standard deviations that each nuclear data parameter was allowed to vary.

TABLE 6.6: Naming conventions for the various configurations of the BeRP-Ni and BeRP-W benchmarks.

Benchmark	Specific configuration #	Overall configuration #
BeRP-Ni	1	1
	2	2
	3	3
	4	4
	5	5
	6	6
	7	7
BeRP-W	0	8
	1	9
	2	10
	3	11
	4	12
	5	13
	6	14
	7	15

TABLE 6.7: Naming conventions for the various configurations of the SCRαP benchmark.

Benchmark	Specific configuration #	Overall configuration #
SCRαP	0	16
	1	17
	2	18
	3	19
	4	20
	5	21
	6	22
	7	23
	8	24
	9	25
	10	26
	11	27
	12	28
	13	29
	14	30
	15	31
	16	32

The algorithm was run and a solution of optimized nuclear data values for $\bar{\nu}_S$, σ_S, and σ_I were obtained. These new $\bar{\nu}_S$, σ_S, and σ_I (the values of which are 2.1347, 1.1408, and 1.1441, respectively) were then input into the detailed benchmark MCNP inputs via the FMULT card. Expected improvement in (C-E)/E values, as calculated by the algorithm, were compared to actual improvements resulting from the new simulation results. It should be clarified here that "expected" values are those calculated by the algorithm using the sensitivities input into the algorithm and the nuclear data perturbations suggested by the algorithm, while "actual" values are those output from MCNP using the perturbed nuclear data suggested by the algorithm. As can be seen in Figure 6.20, the algorithm predictions are validated and an overall (C-E)/E improvement of 40% is observed, which is even better than the expected 25% improvement.

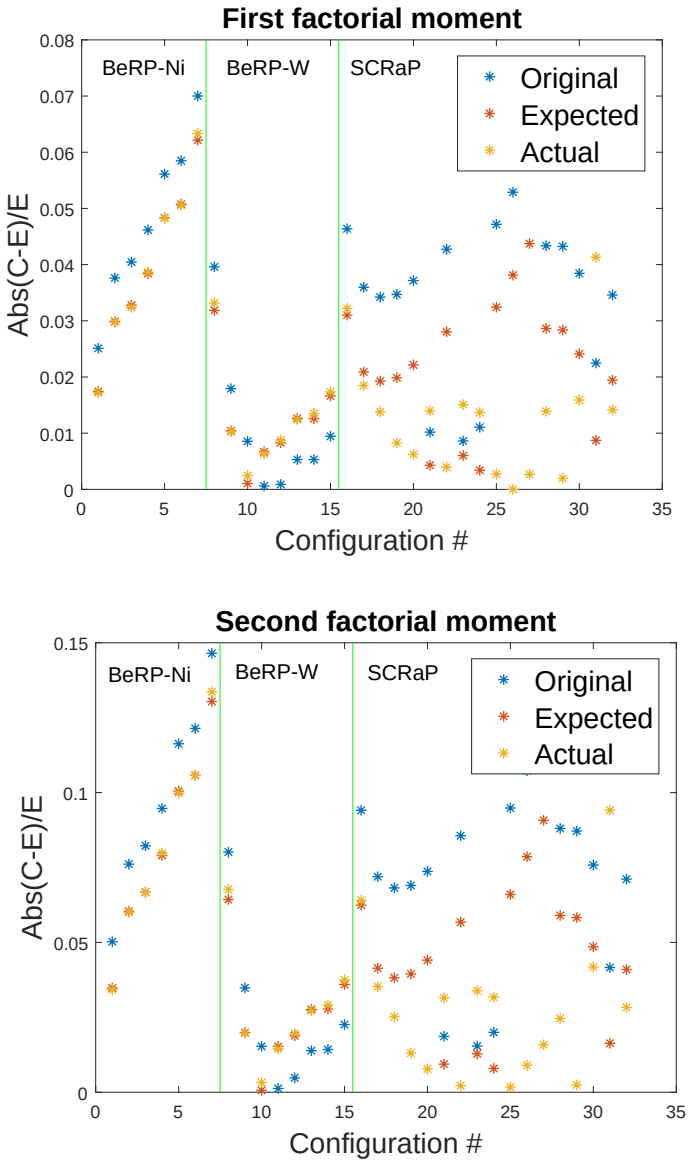

FIGURE 6.20: Expected vs. actual improvements in (C-E)/E values of m_1 and m_2 for all BeRP benchmark configurations when $\bar{\nu}_S = 2.1347$, $\sigma_S = 1.1408$, and $\sigma_I = 1.1441$. Original, expected, and actual values for m_1 sum to 1.0233, 0.7585, and 0.6027, respectively. Original, expected, and actual values for m_2 sum to 2.0762, 1.5590, and 1.2608, respectively.

Although the proposed changes in the widths of the multiplicity distributions in Table 6.15 are well within the assumed 1% uncertainty, $\bar{\nu}_S$ is suggested to decrease by more than 3 standard deviations from the original mean. Because this large of a change might be

unacceptable to nuclear data evaluators, the genetic algorithm was re-run with the additional constraint that all 3 of the nuclear data parameters are not allowed to vary more than 1 standard deviation away from the original mean, and then again with the constraint changed to 2 standard deviations away from the mean. The optimized solutions produced by the constrained algorithm are presented in Table 6.8. The expected improvement given by the constrained algorithm is 9% for 1 standard deviation constraint, and 17% for 2 standard deviation constraint as shown in Table 6.9.

TABLE 6.8: Original and optimized nuclear data values of $\bar{\nu}_S$, σ_S, and σ_I when applying a 1 standard deviation constraint, and when applying a 2 standard deviation constraint.

Nuclear data	Original	Optimized (1 std. dev. constraint)	# Std. dev. change
$\bar{\nu}_S$	2.1510	2.1460	-1.0000
σ_S	1.1510	1.1395	-1.0000
σ_I	1.1400	1.1400	0.0000
Nuclear data	Original	Optimized (2 std. dev. constraint)	# Std. dev. change
$\bar{\nu}_S$	2.1510	2.1410	-2.0000
σ_S	1.1510	1.1370	-1.2183
σ_I	1.1400	1.1450	0.4409

TABLE 6.9: Values of % improvement in combined m_1 and m_2 (C-E)/E values when applying a 1 standard deviation constraint, and when applying a 2 standard deviation constraint.

Nuclear data	Improvement in (C-E)/E (expected)	Improvement in (C-E)/E (actual)
Optimized with 1 std. dev. constraint	9%	26%
Optimized with 2 std. dev. constraint	17%	-

The results in Table 6.8 show that when the nuclear data are constrained within their corresponding uncertainties, $\bar{\nu}_S$ and σ_S are pushed as low as they are allowed to go, while σ_I

is left relatively unchanged. When the nuclear data are instead constrianed within 2 standard deviations, $\bar{\nu}_S$ is pushed as low as it is allowed to go, σ_S is decreased significantly, and σ_I is moderately increased. Combined with the results in Table 6.15, these results show that optimization is most easily reached by greatly decreasing $\bar{\nu}_S$, but when $\bar{\nu}_S$ is not allowed to fall below a certain value, σ_S is decreased much more to compensate. This results in less overall improvement in (C-E)/E values, but more reasonable changes in nuclear data. Figure 6.21 plots the expected and actual improvements in the (C-E)/E values of m_1 and m_2 for the 1 standard deviation constraint solution.

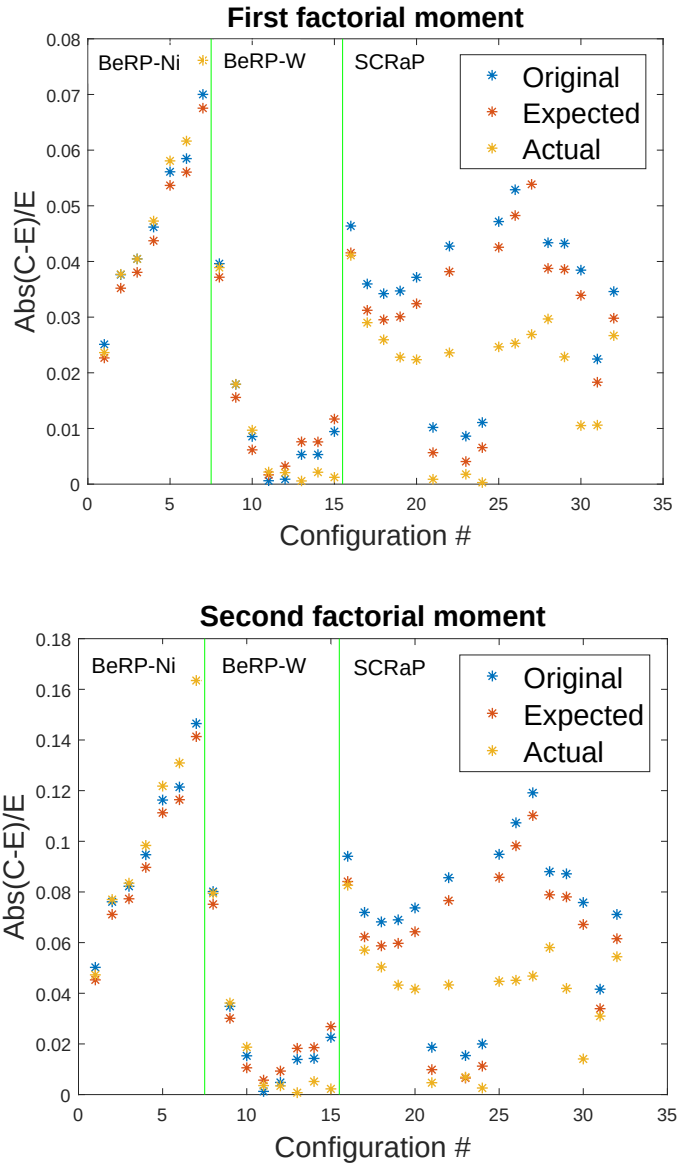

FIGURE 6.21: Expected vs. actual improvements in (C-E)/E values of m_1 and m_2 for all BeRP benchmark configurations when nuclear data adjustments are constrained to 1 standard deviation or less. Original, expected, and actual values for m_1 sum to 1.0233, 0.9308, and 0.7645, respectively. Original, expected, and actual values for m_2 sum to 2.0762, 1.8940, and 1.5403, respectively.

Due to the fact that $\bar{\nu}_S$ clearly has a much larger effect on the observables of interest, as compared to σ_S and σ_I, the genetic algorithm was run with only $\bar{\nu}_S$ being allowed to change.

The resulting solution is $\bar{\nu}_S = 2.1327$ with an expected improvement of 27%, which is very similar to the unconstrained solution of $\bar{\nu}_S = 2.1347$, $\sigma_S = 1.1408$, and $\sigma_I = 1.1441$.

Next, the capability of perturbing $\bar{\nu}_I$, the ^{239}Pu induced fission $\bar{\nu}$, was added to the algorithm. Perturbing $\bar{\nu}_I$ is much more complicated than perturbing the other neutron multiplicity parameters, which involve adjusting only the value listed on the FMULT card in the MCNP input file. In order to perturb $\bar{\nu}_I$, a Python script was used to adjust the values for each energy group in the ENDF/B-VII.1 ACE file for ^{239}Pu. Although $\bar{\nu}_I$ does affect critical benchmark as well as subcritical benchmark simulation performance, it was considered beneficially informative to determine how allowing variation of $\bar{\nu}_I$ would affect the nuclear data adjusment suggested by the algorithm. Table 6.10 lists the nuclear data adjustments output by the algorithm with the addition of $\bar{\nu}_I$, both with and without including the previous constraint of a maximum of 1 standard deviation adjusments. For $\bar{\nu}_I$, the entire curve of $\bar{\nu_I}(E)$ was varied in an energy-independent fashion rather than by energy group. The percent uncertainty was taken from ENDF/B-VII.1 at an incident neutron energy of 2 MeV and assumed to be representative across the entire curve. 2 Mev was chosen because this is the approximate average energy of neutrons causing fission in the bare BeRP ball [35]. The percent uncertainties at 0.0253 eV, 2 MeV, and 10 MeV incident neutron energy are 0.19%, 0.29%, and 0.31%, respectively. Therefore, 0.29% was considered to be a good approximation of the percent uncertainty over the entire energy range. In addition, the genetic algorithm recommended an adjustment of only -0.03% which is well within all of the above mentioned percent uncertainties. As can be seen in Figure 6.22 and Table 6.11, an overall improvement of 18% is predicted and 30% is observed when the constrained genetic algorithm solution is actually tested in MCNP.

TABLE 6.10: Original and optimized nuclear data values of $\bar{\nu}_S$, σ_S, σ_I, and $\bar{\nu}_I$ when allowing $\bar{\nu}_I$ to vary but maintaining the 1 standard deviation maximum adjustment constraint, and when allowing variation without constraint.

Nuclear data	Original	Optimized	# Std. dev. change
$\bar{\nu}_S$	2.1510	2.1460	-1.0000
σ_S	1.1510	1.1472	-0.3301
σ_I	1.1400	1.1403	0.0263
$\bar{\nu}_I$ (2 MeV)	3.1780	3.1771	-0.1000
$\bar{\nu}_S$	2.1510	2.1373	-2.7335
σ_S	1.1510	1.1529	0.1625
σ_I	1.1400	1.1405	0.0437
$\bar{\nu}_I$ (2 MeV)	3.1780	3.1777	-0.0230

TABLE 6.11: Values of % improvement in combined m_1 and m_2 (C-E)/E values when allowing $\bar{\nu}_I$ to vary but maintaining the 1 standard deviation maximum adjustment constraint, and when allowing variation without constraint.

Nuclear data	Improvement in (C-E)/E (expected)	Improvement in (C-E)/E (actual)
Optimized with 1 std. dev. constraint and including $\bar{\nu}_I$	18%	30%
Optimized with no constraint and including $\bar{\nu}_I$	25%	-

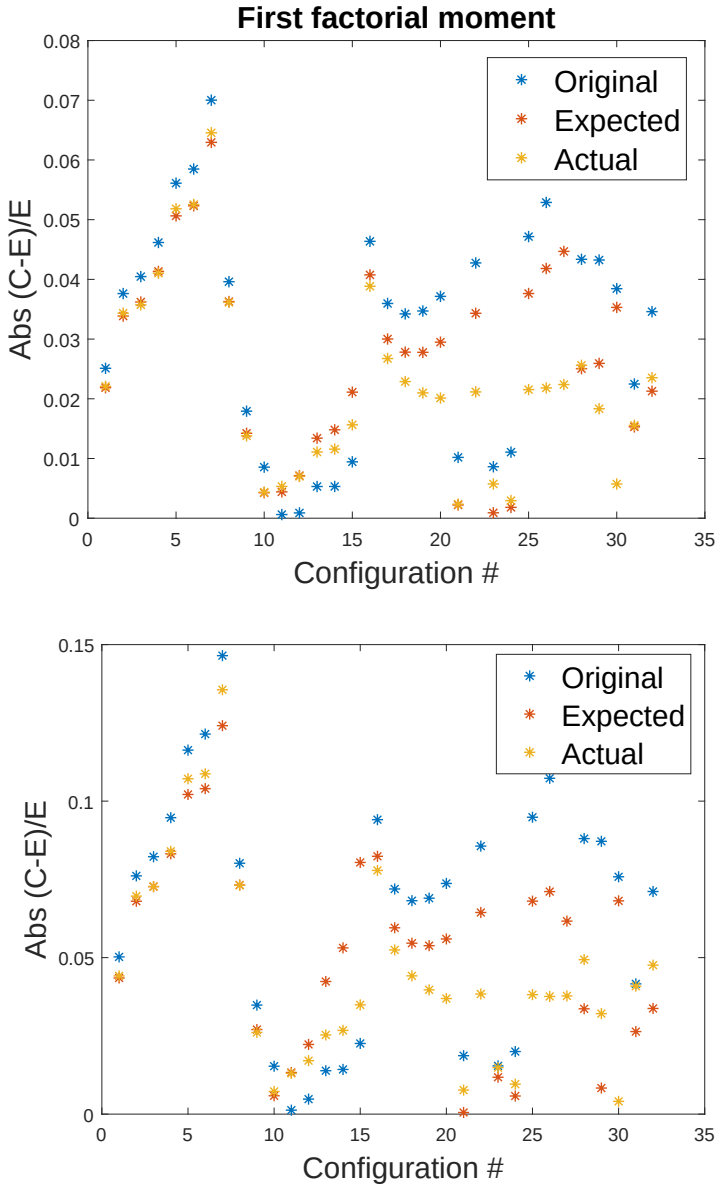

FIGURE 6.22: Expected vs. actual improvements in (C-E)/E values of m_1 and m_2 for all BeRP benchmark configurations when $\bar{\nu_I}$ is also allowed to vary within 1 standard deviation. Original, expected, and actual values for m_1 sum to 1.0233, 0.8569, and 0.7233, respectively. Original, expected, and actual values for m_2 sum to 2.0762, 1.6750, and 1.4545, respectively.

When allowing $\bar{\nu_I}$ to vary without constraint, it is not decreased by much. Rather, the algorithm focuses on decreasing $\bar{\nu_S}$ by several standard deviations. In fact, the unconstrained solution in Table 6.10 is very similar to that of $\bar{\nu_S} = 2.1347$, when $\bar{\nu_I}$ was not included. When applying the 1 standard deviation constraint, $\bar{\nu_I}$ is decreased more but still not by much. It

seems that because of the constraint on $\bar{\nu_S}$, the genetic algorithm again decreased the other nuclear data parameters to compensate. This behavior is similar to what is shown in Table 6.8 when applying the 1 and 2 standard deviation constraints on $\bar{\nu_S}$, σ_S, and σ_I. In fact, the improvement in (C-E)/E values is similar for both of the 1 standard deviation constraint solutions, although it is slightly larger when $\bar{\nu_I}$ is allowed to vary.

It should be mentioned that as of the new ENDF/B-VIII.0 release [1], $\nu_I(\bar{E})$ at 2 MeV incident neutron energy has been decreased from 3.1780 to 3.1755. The optimized values of $\bar{\nu_I}$ in Table 6.10 decreased $\bar{\nu_I}$, which is the same direction $\bar{\nu_I}$ was moved in ENDF/B-VIII.0. The magnitude for which $\bar{\nu_I}$ changed in ENDF/B-VIII.0 was greater than the magnitude suggested by the genetic algorithm, but the results from the genetic algorithm support the decision to decrease $\bar{\nu_I}$.

Summaries of the various nuclear data solutions output by the genetic algorithm, as well as the corresponding percent improvements, are shown in Tables 6.12 and 6.13. These tables show an overall tendency for the genetic algorithm to decrease the nuclear data parameters of interest. In general when the paramters are allowed to vary without restriction, they are decreased by more than in the restricted cases. More improvement in (C-E)/E values is shown when the nuclear data parameters vary without restriction, but such large changes might not be as desirable to nuclear data evaluators. Significant improvement can still be obtained when constraining the nuclear data values to within 1 or 2 standard deviations of their original mean values. The observables of interest also seem to be more sensitive to the $\bar{\nu}$ values as opposed to the values of σ, for both spontaneous and induced fission. Data such as that in Tables 6.12 and 6.13 will be provided to nuclear data evaluators to help provide additional information when making adjustments in future cross-section library releases.

TABLE 6.12: Original and optimized nuclear data values of $\bar{\nu}_S$, σ_S, σ_I, and $\bar{\nu}_I$ for various genetic algorithm initial conditions.

Nuclear data parameter	$\bar{\nu}_S$	σ_S	σ_I	$\bar{\nu}_I$(2 MeV)
Original	2.1510	1.1510	1.1400	3.1780
Unconstrained	2.1347	1.1408	1.1441	-
Unconstrained, varying $\bar{\nu}_S$ only	2.1327	-	-	-
Unconstrained, including variation of $\bar{\nu}_I$	2.1373	1.1529	1.1405	3.1777
1 std. dev. constraint	2.1460	1.1395	1.1400	-
2 std. dev. constraint	2.1410	1.1370	1.1450	-
1 std. dev. constraint, including variation of $\bar{\nu}_I$	2.1460	1.1472	1.1403	3.1771

TABLE 6.13: Values of % improvement in combined m_1 and m_2 (C-E)/E values for various genetic algorithm initial conditions.

Percent improvement	Expected	Actual
Unconstrained	25%	40%
Unconstrained, varying $\bar{\nu}_S$ only	27%	-
Unconstrained, including variation of $\bar{\nu}_I$	25%	-
1 std. dev. constraint	9%	26%
2 std. dev. constraint	17%	-
1 std. dev. constraint, including variation of $\bar{\nu}_I$	18%	30%

In order to verify that the optimized nuclear data values and overall (C-E)/E improvement were not specific to the set of 32 configurations included in the 3 BeRP benchmarks, the configurations were split into a series of 16 training and 16 testing configurations. The 8 different combinations of training and testing configurations are listed in Table 6.14.

TABLE 6.14: Training and testing data sets used to validate algorithm performance.

Iteration #	Training configurations
1	BeRP-Ni 4-7, BeRP-W 0-7, and SCRαP 0-3
2	BeRP-W 0-7 and SCRαP 0-7
3	BeRP-W 4-7 and SCRαP 0-11
4	SCRαP 0-15
5	SCRαP 4-16 and BeRP-Ni 1-3
6	SCRαP 8-16 and BeRP-Ni 1-7
7	SCRαP 12-16, BeRP-Ni 1-7, and BeRP-W 0-3
8	SCRαP 16, BeRP-Ni 1-7, and BeRP-W 0-7
Iteration #	Testing configurations
1	SCRαP 4-16 and BeRP-Ni 1-3
2	SCRαP 8-16 and BeRP-Ni 1-7
3	SCRαP 12-16, BeRP-Ni 1-7, and BeRP-W 0-3
4	SCRαP 16, BeRP-Ni 1-7, and BeRP-W 0-7
5	BeRP-Ni 4-7, BeRP-W 0-7, and SCRαP 0-3
6	BeRP-W 0-7 and SCRαP 0-7
7	BeRP-W 4-7 and SCRαP 0-11
8	SCRαP 0-15

For each of the 8 different combinations of training and testing sets, the 16 training configurations were used to run the original unconstrained genetic algorithm. Using the resulting optimized nuclear data values, the expected improvement of both the training and testing sets were calculated, and were also averaged in order to determine the overall expected improvement. All training set, testing set, and overall expected improvements are plotted in Figure 6.23 for the various training and testing set combinations. The optimized changes in nuclear data values are also plotted in Figure 6.23. It is clear that regardless of how the data is split into training and testing sets, the overall improvement hovers around 25%. In addition, all optimized changes in nuclear data values are similar, especially for $\bar{\nu}_S$. The optimized widths of the multiplicity distributions show much more variation, but it is clear that these parameters do not have nearly as much effect on the observables of interest as the mean of the spontaneous fission multiplicity distribution does.

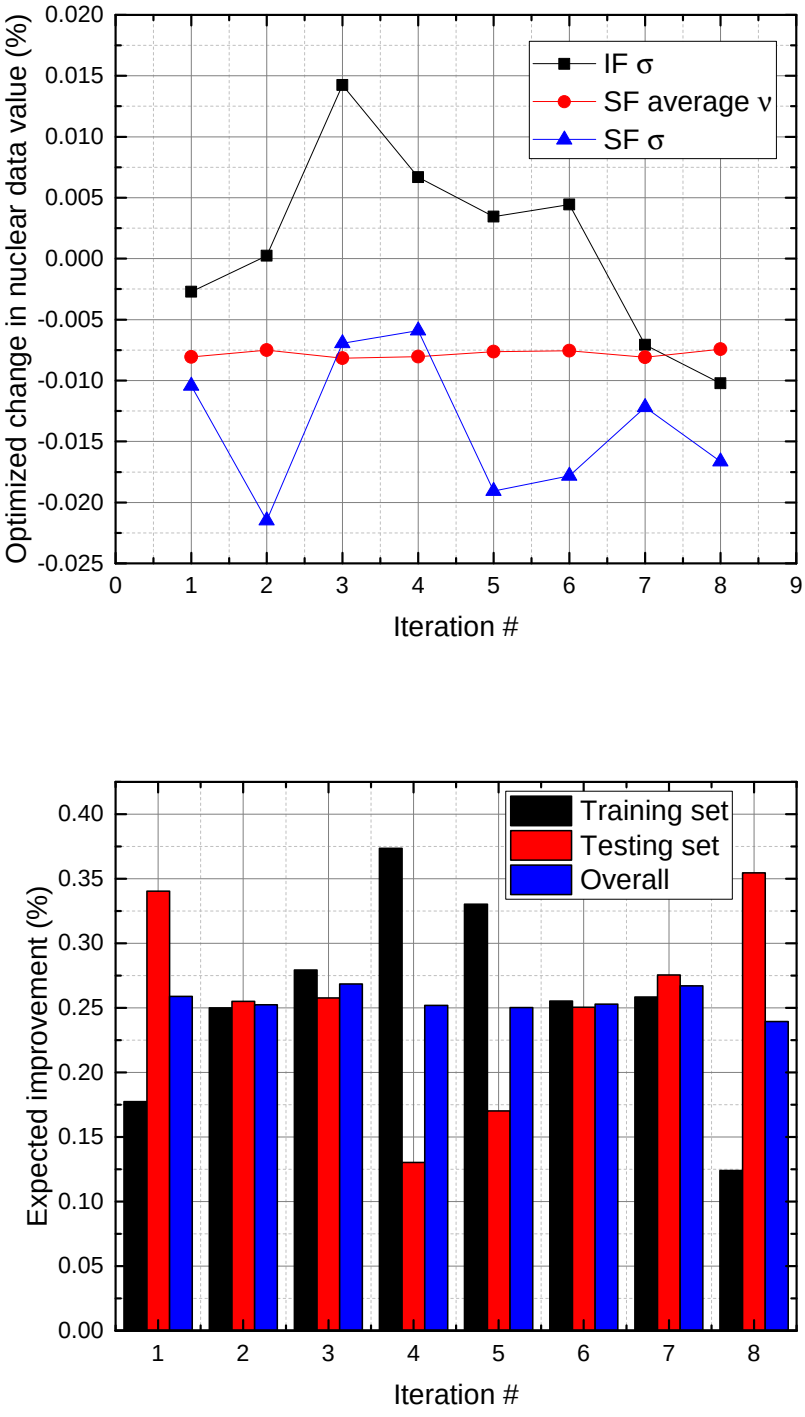

FIGURE 6.23: Optimized changes in nuclear data values and expected improvments for all combinations of training and testing data sets.

Tables 6.15 lists the original nuclear data values, the values output by the algorithm previously when using all 32 configurations as input data (optimized #1), and the values obtained when averaging over all 8 of 16 configuration training sets (optimized #2). For each of the optimized nuclear data values, the number of standard deviations away from the original values is also listed. Table 6.16 shows the expected and actual (when applicable) % improvement for both sets of adjusted nuclear data.

TABLE 6.15: Original and optimized nuclear data values of $\bar{\nu}_S$, σ_S, and σ_I when using all 32 configurations as input data (optimized #1), and when averaging over all 8 of the 16-configuration training sets (optimized #2).

Nuclear data	Original	Optimized #1	# Std. dev. change
$\bar{\nu}_S$	2.1510	2.1347	-3.2600
σ_S	1.1510	1.1408	-0.0886
σ_I	1.1400	1.1441	0.0360
Nuclear data	Original	Optimized #2	# Std. dev. change
$\bar{\nu}_S$	2.1510	2.1342	-3.3596
σ_S	1.1510	1.1351	-0.1381
σ_I	1.1400	1.1413	0.0113

TABLE 6.16: Values of % improvement in combined m_1 and m_2 (C-E)/E values for the original and optimized nuclear data values of $\bar{\nu}_S$, σ_S, and σ_I when using all 32 configurations as input data (optimized #1), and when averaging over all 8 of the 16-configuration training sets (optimized #2).

Nuclear data	Improvement in (C-E)/E (expected)	Improvement in (C-E)/E (actual)
Optimized #1	25%	40%
Optimized #2	25%	-

In order to test whether or not the genetic algorithm would output similar solutions when the (C-E)/E values for m_1 and m_2 are optimized separately, the algorithm was split into 2 algorithms, one that aims to optimize m_1 and the other that aims to optimize m_2. The resulting solutions are listed in Table 6.17, and compared to the solution originally obtained by optimizing m_1 and m_2 simultaneously. The improvements yielded by the m_1 and m_2 algorithms are both 27%, compared to the original expected 25% improvement. The comparison shows that regardless of whether the observables are optimized individually or together, similar solutions are produced. In fact, the variations among the 3 different solutions are within the range of variations shown among the different solutions produced by the previously discussed 8 training data sets. These results justify the decision to use equal weighting of the 2 observables in the fitness function.

TABLE 6.17: Optimized nuclear data values of $\bar{\nu}_S$, σ_S, and σ_I when optimizing m_1 alone, m_2 alone, and m_1 and m_2 together.

Nuclear data	Original	Optimized for m_1	# Std. dev. change
$\bar{\nu}_S$	2.1510	2.1338	-3.4415
σ_S	1.1510	1.1399	-0.9675
σ_I	1.1400	1.1437	0.3222
Nuclear data	Original	Optimized for m_2	# Std. dev. change
$\bar{\nu}_S$	2.1510	2.1333	-3.5468
σ_S	1.1510	1.1398	-0.9689
σ_I	1.1400	1.1419	0.1638
Nuclear data	Original	Optimized for m_1 and m_2	# Std. dev. change
$\bar{\nu}_S$	2.1510	2.1347	-3.2600
σ_S	1.1510	1.1408	-0.0886
σ_I	1.1400	1.1441	0.0360

TABLE 6.18: Values of % improvement in combined m_1 and m_2 (C-E)/E values when optimizing m_1 alone, m_2 alone, and m_1 and m_2 together.

Nuclear data	Improvement in (C-E)/E (expected)	Improvement in (C-E)/E (actual)
Optimized for m_1	27%	-
Optimized for m_2	27%	-
Optimized for m_1 and m_2	25%	40%

6.2.4 Other considerations

The novel genetic algorithm developed in this work yields improved performance for subcritical benchmark simulation results, both with and without affecting critical benchmark simulations. All of the nuclear data parameters varied in this work except for $\bar{\nu}_I$ do not affect criticality (such as KCODE in MCNP) simulations. The spontaneous fission multiplicity distribution is a descriptor of source neutrons only, and therefore does not affect the effective multiplication factor k_{eff}. In fact, one of the primary assumptions in the KCODE calculation process is that there are no external sources, and spontaneous fission is considered an external source. The structure of the induced fission multiplicity distribution, other than the mean $\bar{\nu}_I$, also does not affect the multiplication of the system.

Previous work in this area has focused on randomly (rather than optimally) perturbing $\bar{\nu}(E)$ in both an energy-independent and energy-dependent manner in order to produce improved Feynman histograms. Reduced χ^2 comparisons between simulated and measured Feynman histograms were used as a metric for the subcritical experiments, and χ^2 comparisons between simulated and measured k_{eff} values were used as a metric for the critical experiments. The total FOM was defined as the sum of the two χ^2 values. The energy-independent perturbation shifted the entire induced fission $\bar{\nu}(E)$ curve down by 1.14%. The results of this perturbation showed excellent improvement in subcritical χ^2 but drastic worsening of the critical χ^2, and was therefore considered unusable. The energy-dependent perturbations showed less improvement in subcritical χ^2 but preserved the critical χ^2 much better. However, the suggested changes in $\bar{\nu}(E)$ as a function of energy reduced the smoothness of the curve, and were not adopted in the latest nuclear data evaluation. The nuclear data evaluation field strives to maintain consistency with the fundamental physics underlying nuclear data, and the physics underlying the fission reaction suggests smooth variation of $\bar{\nu}(E)$ as a function of incident neutron energy [97].

Although the genetic algorithm in this work focuses on certain specific neutron fission multiplicity distribution parameters, any nuclear data parameter that subcritical benchmark experiments are sensitive to could be optimized using the algorithm framework. The ^{239}Pu induced fission cross-section, for instance, would likely have a large effect on the subcritical benchmark simulated results. However, these parameters would also affect the critical benchmarks. The primary nuclear data items varied in this work were specifically chosen to be able to improve subcritical benchmark simulation performance without affecting the

critical benchmark simulation performance. If an effort was made to improve both subcritical and critical benchmark simulation performance, it would be beneficial to include other nuclear data parameters that the benchmarks are sensitive to, such as the fission and capture cross-sections of the various isotopes of interest in the experiment.

The sensitivities of k_{eff} to the total cross-section of every isotope was calcluated using the KSEN option in MCNP for the BeRP-Ni configuration 7, the BeRP-W configuration 7, and the SCRαP configuration 15. These configurations were chosen because they represent the highest multiplication case for each of the benchmarks. The greatest sensitivities are listed in Table 6.19. From these results it can be concluded that if one were to vary other nuclear data using the subcritical neutron multiplication benchmarks, the ^{239}Pu and ^{240}Pu cross-sections, as well as the reflector material isotope cross-sections, would have the largest effects.

TABLE 6.19: Sensitivities of k_{eff} to select cross-sections in the subcritical benchmark models.

Benchmark	Isotope	Sensitivity
BeRP-Ni	^{239}Pu	7.76E-01
BeRP-Ni	^{58}Ni	9.72E-02
BeRP-Ni	^{60}Ni	4.58E-02
BeRP-Ni	^{240}Pu	3.34E-02
BeRP-Ni	^{62}Ni	9.19E-03
BeRP-W	^{239}Pu	7.57E-01
BeRP-W	^{186}W	5.60E-02
BeRP-W	^{184}W	5.50E-02
BeRP-W	^{182}W	4.76E-02
BeRP-W	^{240}Pu	3.12E-02
SCRαP	^{239}Pu	7.04E-01
SCRαP	^{63}Cu	9.44E-02
SCRαP	^{65}Cu	5.39E-02
SCRαP	^{1}H	4.83E-02
SCRαP	^{240}Pu	2.61E-02

Chapter 7

Conclusions and Future Work

7.1 Conclusions

SNM measurements and simulations are integral to nuclear nonproliferation and criticality safety, for applications such as SNM identification and characterization, experiment planning, detection system development, and many others. Predictive radiation transport codes and accurate nuclear data knowledge are necessary for precisely predicting the results of SNM measurements. The goal of this work was to apply subcritical neutron multiplication inference measurements and simulations to validation of the nuclear data and computational methods currently used to predicatively model SNM experiments.

Two subcritical neutron multiplication inference measurements (and corresponding simulations) have been completed. These include both a state-of-the-art subcritical benchmark (SCRαP) and an advanced subcritical measurement (CaSPER) designed to pave the way for future research reactor subcritical benchmarks. SCRαP shows good comparison between simulated and measured results, and preliminary sensitivity and uncertainty analysis has been conducted. Although good simulation performance is shown, discrepancies do still exist with measured data. These discrepancies are larger than the combinations of all statistical and systematic uncertainties, and therefore must be due to errors in the underlying nuclear data (such as ^{63}Cu, ^{65}Cu, or ^{239}Pu) or radiation transport codes. CaSPER has resulted in an established protocol for future research reactor subcritical neutron multiplication inference benchmarks. Following the completion and analysis of the two experiments, several methods of applying subcritical neutron multiplication inference benchmarks to nuclear data and computational methods validation were proposed. All have been completed. A Bayesian optimization algorithm for benchmark experiment design has been developed and validated. The algorithm significantly reduces the computation time required for subcritcal benchmark design. An improved FOM for Feynman histograms has been developed and validated, and allows for improved quantitative comparison of Feynman histograms. The performance of

various radiation transport codes that take into account the correlated physics of fission have been investigated by using the Pearson correlation coefficient to explore correlations between data items and observables of interest. There is no clearly best performing code, but correlations do exist (e.g., between R_1 and ^{240}Pu spontaneous fission $\bar{\nu}$) and should be investigated. A genetic algorithm for nuclear data evaluation has been developed and validated. The genetic algorithm has been tested and shows good performance. The algorithm is able to intelligently converge on a set of fission neutron multiplicity distribution parameters (^{240}Pu $\bar{\nu}$, ^{240}Pu σ, and ^{239}Pu σ) that yield improved performance of simulated results as compared to the measured benchmark results, when applied to the BeRP-Ni, BeRP-W, and SCRαP subcritical neutron multiplication inference benchmarks. The algorithm is able to yield such improved performance of subcritical benchmark results, without affecting critical benchmark simulations. In addition, if ^{239}Pu $\bar{\nu}$ is also allowed to vary, although it does affect critical benchmark simulations,improved performance of simulated subcritical benchmark results is also shown. The work presented here clearly follows the highlighted portions of the path of the nuclear data evaluation process outlined in Figure 1.15. Differential measurements are outside of the scope of this work, but the nuclear data evaluation step has been investigated through feedback from benchmark validation (specifically, subcritical benchmark) measurements in both the comparison of the correlated physics of fission radiation transport codes and the genetic algorithm for nuclear data evaluation development and testing. The nuclear data library processing and radiation transport code development steps are also outside of the scope of this work, but many radiation transport simulations focusing on different aspects of the correlated physics of fission in SNM have been completed and investigated. In addition to conducting two advanced subcritical measurements, the entire work focuses on subcritical benchmark validation measurements and how they are applied to nuclear data and transport code validations.

7.2 Future work

As future work, the SCRαP benchmark evaluation will be published in the next edition of the ICSBEP handbook. The CaSPER research reactor protocol will be applied to the proposed benchmark at the 7uPCX reactor at SNL. The improved FOM equation for Feynman histograms will continue to be used to quantitatively compare measured and simulated Feynman histogram results. The Bayesian optimization algorithm will be utilized in the design process of future subcritical neutron multiplication inference benchmarks, such as the SNL research reactor benchmark and the BeRP-Mo benchmark. The performance of correlated physics of fission codes will continue to be investigated as codes and nuclear data are improved and more subcritical benchmarks become available. The first step would

be to apply the comparison and correlation process to existing radiation transport codes, including MCATK and MORET. The genetic algorithm will be used as a basis for suggesting adjustments to fission neutron multiplicity distribution parameters to nuclear data evaluators. The algorithm can also be expanded to be applied to other nuclear data items, and other experiment types, of interest. The genetic algorithm should also be applied to the recently-released ENDF/B-VIII.0 nuclear data library. In addition, ICSBEP is currently working on calculating correlations between different configurations and benchmarks. Such a correlation matrix could be incorporated into the genetic algortihm framework. The genetic algorithm framework can be further expanded by including critical as well as subcritical benchmarks, and adding the capability to vary nuclear data parameters in an energy-dependent matter while still maintaining the physical structure of the curves. Data produced using the GA process developed here will be passed on to nuclear data evaluators which will provide them an additional tool to be used for nuclear data improvements in future cross-section libraries.

References

1. D. Brown, M. Chadwick, R. Capote, and et al., "ENDF/B-VIII.0: The 8th major release of the nuclear reaction data library with CIELO-project cross sections, new standards and thermal scattering data," *Nuclear Data Sheets*, vol. 148, pp. 1–142, 2018.

2. G. F. Knoll, *Radiation Detection and Measurement, Fourth Edition*. Wiley, 2010.

3. D. Reilly, N. Enselin, H. S. Jr., and S. Kreiner, "Passive nondestructive assay of nuclear materials," *NUREG/CR-5550, LA-UR-90-732*, 1991.

4. G. R. Keepin, *Physics of Nuclear Kinetics*, H. Goldstein, Ed. Addison-Wesley, 1965.

5. J. Hutchinson, B. Mustafa, M. A. Smith-Nelson, W. Myers, T. E. Cutler, C. J. Solomon, A. Sood, D. R. Dinwiddie, and T. J. Grove, "Subcritical multiplication experiments & simulations: Overview and recent advances," *Advances in Nuclear Nonproliferation Technology and Policy Conference*, 2016.

6. M. Chadwick *et al.*, "ENDF/B-VII.1 nuclear data for science and technology: Cross sections, covariances, fission product yields and decay data," *Nuclear Data Sheets*, vol. 112, pp. 2887–2996, 2011.

7. C. Wagemans, "The nuclear fission process," *CRC Press, Boca Raton*, 1991.

8. J. Lestone, "Energy and isotope dependence of neutron multiplicity distributions," *Nuclear Science and Engineering*, 2005.

9. B. Richard and J. Hutchinson, "Tungsten-reflected plutonium-metal-sphere subcritical measurements," *International Handbook of Evaluated Criticality Safety Benchmark Experiments*, vol. NEA/NSC/DOC/(95)03/I, pp. FUND–NCERC–PU–HE3–MULT–002, 2016.

10. T. H. Shin, J. Hutchinson, R. Bahran, and S. A. Pozzi, "A note on the nomenclature in neutron multiplicity mathematics," *Submitted to Nuclear Science and ENgineering*, 2018.

11. J. Briggs, J. Bess, and J. Gulliford, "Integral benchmark data for nuclear data testing through the ICSBEP & IRPhEP," *Nuclear Data Sheets*, vol. 118, pp. 396–400, 2014.

12. J. B. Briggs, "The international criticality safety benchmark evaluation project (ICSBEP)," *International Conference on Nuclear Energy for New Europe*, 2003.

13. F. Brown, "The mcnp6 analytic criticality benchmark suite," *LA-UR-16-24255*, 2016.

14. H. C. Paxton, "Thirty-five years at pajarito canyon site," *LA-7121-H, Rev.*, 1981.

15. R. E. Malenfant, "Experiments with the dragon machine," *LA-14241-H*, 2005.

16. D. Loaiza and D. Gehman, "End of an era for the los alamos critical experiments facility: History of critical assemblies and experiments (1946-2004)," *Annals of Nuclear Energy*, vol. 33, pp. 1339–1359, 2006.

17. J. A. Arthur, R. M. Bahran, J. D. Hutchinson, M. E. Rising, and S. A. Pozzi, "Comparison of the performance of various correlated fission multiplicity monte carlo codes," *Transactions of the American Nuclear Society Winter Meeting and Technology Expo*, 2016.

18. R. Bahran, J. Hutchinson, B. Richard, and A. Sood, "List-mode simulations of the Thor core benchmark sensitivity experiments," *Transactions of the American Nuclear Society Annual Meeting*, vol. 111, pp. 805–808, 2014.

19. A. Sood, C. J. Solomon, J. D. Hutchinson, and R. Bahran, "A review of recent R&D efforts in sub-critical multiplication measurements and simulations," *Transactions of the American Nuclear Society Annual Meeting*, 2014.

20. S. R. Bolding and C. J. Solomon, "Simulations of multiplicity distributions with perturbations to nuclear data," *Transactions of the American Nuclear Society*, vol. 109, pp. 251–254, 2013.

21. E. C. Miller, J. K. Mattingly, B. D. Dennis, S. D. Clarke, and S. A. Pozzi, "Simulations of neutron multiplicity measurements with MCNP-PoliMi," *Technical Report SAND2010-6830, Sandia National Laboratory*, 2010.

22. J. Mattingly, "Polyethylene-reflected plutonium metal sphere: Subcritical neutron and gamma measurements," *Sandia National Laboratory Report SAND2009-5804*, 2009.

23. R. Bahran, S. Croft, J. Hutchinson, M. Smith, and A. Sood, "A survey of nuclear data deficiences affecting nuclear non-proliferation," *Proceedings of the 2014 INMM Annual Meeting, Atlanta GA*, 2014.

24. R. T. Kouzes, J. H. Ely, A. Seifert, E. R. Siciliano, D. R. Weier, L. K. Windsor, M. L. Woodring, J. Borgardt, E. Buckley, E. Flumerfelt, A. Oliveri, and M. Salvitti, "Cosmic-ray-induced ship-effect neutron measurements and implications for cargo scanning at borders," *Nucl. Instruments and Methods in Physics Research Section A: Accelerators, Spectrometers, Detectors and Associated Equipment*, vol. 587, no. 1, pp. 89–100, 2008.

25. M. L. Ruch, M. Flaska, and S. A. Pozzi, "Pulse shape discrimination performance of stilbene coupled to low-noise silicon photomultipliers," *Nuclear Instruments and Methods in Physics Research A*, vol. 793, pp. 1–5, 2015.

26. T. H. Shin, M. Y. Hua, M. J. Marcath, D. L. Chichester, I. Pazsit, A. D. Fulvio, S. D. Clarke, and S. A. Pozzi, "Neutron multiplicity counting moments for fissile mass estimation in scatter-based neutron detection systems," *Nuclear Science and Engineering*, vol. 188, no. 3, pp. 246–269, 2017.

27. M. J.Marcath, T. H. Shin, S. D.Clarke, P. Peerani, and S. A. Pozzi, "Neutron angular distribution in plutonium-240 spontaneous fission," *Nuclear Instruments and Methods in Physics Research A*, vol. 830, pp. 163–169, 2016.

28. R. E. Uhrig, *Random Noise Techniques in Nuclear Reactor Systems*. The Ronald Press Company, 1970.

29. G. McKenzie, "Modern rossi alpha measurements," *University of Illinois at Urbana-Champaign M.S. Thesis*, 2014.

30. S. Degweker and R. Rudra, "On the relation between Rossi alpha and Feynman alpha methods," *Annals of Nuclear Energy*, vol. 94, pp. 433–439, 2016.

31. G. Hansen, H. Helmick, and J. Orndoff, "Neutron counting statistics in basic fast critical assemblies," *Transactions of a Japan-United States Seminar on Nuclear Reactor Noise Analysis*, 1968.

32. R. Kuramoto, A. D. Santos, R. Jerez, R. Diniz, U. Bitelli, T. M. Filho, and C. L. Veneziani, "Rossi-α experiment in the IPEN/MB-01 research reactor: Validation of two-region model and absolute measurement of β_{eff} and Λ," *PHYSOR-2006, ANS Topical Meeting on Reactor Physics*, 2006.

33. J. Hutchinson, G. McKenzie, J. Arthur, M. Nelson, and W. Monage, "Prompt neutron decay constant fitting using the rossi-alpha and feynman variance-to-mean methods," *Transactions of the American Nuclear Society*, vol. 117, pp. 986–989, 2017.

34. M. Y. Hua, J. D. Hutchinson, G. E. McKenzie, and M. A. Nelson, "2-exponential pdf and analytic uncertainty approximations for rossi-alpha histograms," *ANS Winter Meeting and Nuclear Technology Expo*, 2018.

35. J. D. Hutchinson, M. A. Smith-Nelson, T. E. Cutler, B. L. Richard, and T. J. Grove, "Estimation of uncertainties for subcritical benchmark measurements," *International Conference on Computing, Networking and Communications*, 2015.

36. E. F. Bennett, "The rice formulation of reactor noise," *Nuclear Science and Engineering*, vol. 8, no. 1, p. 53, 1960.

37. A. I. Mogilner and V. G. Zolotukhin, "The statistical r-method of measuring the kinetic parameters of a reactor," *Atomic Energy (USSR)*, vol. 10, no. 377, 1961.

38. N. Pacilio, "The polya model and the distribution of neutrons in a steady state reactor," *Nuclear Science and Engineering*, vol. 26, no. 4, p. 565, 1966.

39. D. Babala, "Neutron counting statistics in nuclear reactors," *Norwegian Report KR-114*, 11 1966.

40. P. Santi and M. Miller, "Reevaluation of prompt neutron emission multiplicity distributions for spontaneous fission," *Nuclear Science and Engineering*, vol. 160, pp. 190–199, 2008.

41. J. Terrell, "Distributions of fission neutron numbers," *Physical Review*, vol. 108, pp. 783–789, 1957.

42. NRDC-Network, "CSISRS/EXFOR library of experimental cross sections," *www.nndc.bnl.gov/exfor*, 2017.

43. M. Chadwick *et al.*, "ENDF/B-VII.0: next generation evaluated nuclear data library for nuclear science and technology," *Nuclear Data Sheets*, vol. 107, pp. 2931–3060, 2006.

44. J. A. Arthur, M. E. Rising, J. D. Hutchinson, A. T. McSpaden, and R. M. Bahran, "Validation of mcnp6 using subcritical benchmark experiments," *ANS Winter meeting & Expo*, 2018.

45. E. Barnard, A. Ferguson, W. McMurray, and I. V. Heerden, "Time-of-flight measurements of neutron spectra from the fission of U^{235}, U^{238}, and Pu^{239}," *Nuclear Physics*, vol. 71, pp. 228–249, 1965.

46. N. N. Flerov and V. M. Talyzin, "Average numbers ν and η of neutrons in the fission of u^{233} and pu^{239} by 14 MeV neutrons," *Translated from Atomnaya Energiya*, vol. 10, pp. 68–69, 1960.

47. R. H. Iyer, H. Naik, A. K. Pandey, P. C. Kalsi, R. J. Singh, A. Ramaswami, and A. G. C. Nair, "Measurement of absolute fission yields in the fast neutron-induced fission of actinides: ^{238}u, ^{237}np, ^{238}pu, ^{240}pu, ^{243}am, and ^{244}cm by track-etch-cum-gamma spectrometry," *Nuclear Science and Engineering*, vol. 135, pp. 227–245, 2000.

48. H. Naika, V. Mulikb, P. Prajapatic, B. Shivasankard, S. Suryanarayanae, K. Jagadeesanf, S. Thakaref, S. Sharmae, and A. Goswamia, "Mass distribution in the quasi-mono-energetic neutron-induced fission of ^{238}u," *Nuclear Physics A*, vol. 913, pp. 185–205, 2013.

49. R. Howerton, "Revisited," *Nuclear Science and Engineering*, vol. 62, pp. 438–454, 1977.

50. D. G. Madland and J. R. Nix, "New calculation of prompt fission neutron spectra and average prompt neutron multiplicities," *Nuclear Science and Engineering*, vol. 81, pp. 213–271, 1982.

51. N. E. Holden and M. S. Zucker, "Prompt neutron emission multiplicity distribution and average values (nubar) at 200 m/s for the fissile nuclides," *Nuclear Science and Engineering*, vol. 98:2, pp. 174–181, 1988.

52. M. Rising, "Evaluation and uncertainty quantification of prompt fission neutron spectra of uranium and plutonium isotopes," *Nuclear Science and Engineering*, vol. 175(1), pp. 81–93, Sept. 2013.

53. T. Goorley, M. James, T. Booth, F. Brown, J. Bull, and et al., "Initial MCNP6 release overview," *Nuclear Technology*, vol. 180, pp. 298–315, 2012.

54. C. Solomon, "The mcnptools package," LA-UR-14-27075, Tech. Rep., 2014.

55. A. McSpaden, "Duplicating MC-15 output with python and MCNP," *LA-UR-17-27588*, 2017.

56. P. Talou, R. Vogt, J. Randrup, M. Rising, S. Pozzi, J. Verbeke, M. Andrews, S. Clarke, P. Jaffke, M. Jandel, T. Kawano, M. Marcath, K. Meierbachtol, L. N. nad G. Rusev, A. Sood, I. Stetcu, and C. Walker, "Correlated prompt fission data in transport simulations," *The European Physical Journal A*, vol. 54, no. 9, 2018.

57. J. Arthur, R. Bahran, J. Hutchinson, A. Sood, M. Rising, and S. A.Pozzi, "Validating the performance of correlated fission multiplicity implementation in radiation transport codes with subcritical neutron multiplication benchmark experiments," *Annals of Nuclear Energy*, vol. 120, pp. 348–366, 2018.

58. J. Verbeke, J. Randrup, and R. Vogt, "Fission reaction event yield algorithm, FREYA – for event-by-event simulation of fission," *Computer Physics Communications*, vol. 191, pp. 178–202, 2015.

59. P. Talou *et al.*, "Prompt fission neutrons and gamma rays in a monte carlo Hauser-Feshbach formalism," *Physics Procedia*, vol. 47, pp. 39–46, 2013.

60. R. Bahran and J. Hutchinson, "Subcritical copper-reflected α-phase plutonium (SCRαP) integral experiment design," *Transactions of the American Nuclear Society*, vol. 114, pp. 527–529, 2016.

61. B. Richard and J. Hutchinson, "Nickel reflected plutonium metal sphere subcritical measurements," *International Handbook of Evaluated Criticality Safety Benchmark Experiments*, vol. NEA/NSC/DOC/(95)03/I, pp. FUND–NCERC–PU–HE3–MULT–001, 2014.

62. D. Cifarelli and W. Hage, "Models for a three-parameter analysis of neutron signal correlation measurements for fissile material assay," *Nuclear Instruments and Methods*, vol. A251, pp. 550–563, 1986.

63. J. Hutchinson, B. Rooney, W. Myers, A. Sood, and M. Smith-Nelson, "CALIBAN measurements near delayed critical using subcritical measurement methods," *2013 American Nuclear Society Winter Meeting, Washington DC*, 2013.

64. J. Hutchinson, M. A. Smith-Nelson, A. Sood, J. M. Goda, and J. A. Bounds, "Joint LANL/CEA measurements on Godiva IV," *American Nuclear Society Annual Meeting, Reno NV*, 2014.

65. J. Hutchinson, A. Sood, W. Myers, M. Smith-Nelson, and D. Dinwiddie, "Comparison of HEU measurements using measured and simulated data," *Transactions of the American Nuclear Society*, vol. 106, pp. 487–489, 2013.

66. J. Hutchinson, M. A. Nelson, A. Sood, D. K. hayes, and R. G. Sanchez, "Neutron noise measurements on HEU foils moderated by lucite," *American Nuclear Society Annual Meeting, San Antonio TX*, 2015.

67. B. C. Kiedrowski and F. B. Brown, "Adjoint-based k-eigenvalue sensitivity coefficients to nuclear data using continuous-energy monte carlo," *Nuclear Science & Engineering*, vol. 174, no. 3, pp. 227–244, 2013.

68. C. Moss, E. Sorenson, and M. Nelson, *Multiplicity Counter-15 (MC-15) User Manual*, Los Alamos National Laboratory, LA-UR-16-27099, 2016.

69. B. Richard *et al.*, "Nickel-reflected plutonium-metal-sphere subcritical measurements," *International Handbook of Evaluated Criticality Safety Benchmark Experiments, NEA/NSC/DOC/(95)03/I, FUND-NCERC-PU-HE3-MULT-001*, 2016.

70. M. Smith-Nelson, "Momentum: version 0.36.3," *LANL Software*, Mar. 2015.

71. J. Hutchinson, M. Nelson, T. Grove, J. Arthur, G. McKenzie, R. Bahrana, and T. Cutler, "Validation of statistical uncertainties in subcritical benchmark measurements: Part i - theory and simulations," *Annals of Nuclear Energy*, vol. 125, pp. 50–62, 2019.

72. J. Hutchinson, R. Bahran, T. Cutler, M. Nelson, T. Grove, J. Arthur, G. McKenzie, W. Monange, and E. Dumonteil, "Validation of statistical uncertainties in subcritical benchmark measurements: Part ii - measured data," *Annals of Nuclear Energy, In Press*, 2018.

73. T. Cutler and J. Arthur, "Copper- and polyethylene- reflected plutonium-metal-sphere subcritical measurements," *Submitted to International Handbook of Evaluated Criticality Safety Benchmark Experiments*, vol. NEA/NSC/DOC(95)03/IX, pp. FUND–NCERC–PU–HE3–MULT–003, 2018.

74. J. Arthur, R. Bahran, J. Hutchinson, A. Sood, N. Thompson, and S. Pozzi, "Development of a research reactor protocol for neutron multiplication measurements," *Progress in Nuclear Energy*, vol. 106, pp. 120–139, 2018.

75. R. Bahran, J. Hutchinson, J. Arthur, A. Sood, P. caracappa, N. Thompson, and S. Pozzi, "Development of a research reactor protocol for neutron multiplication measurements," *Transactions of the American Nuclear Society*, vol. 115, pp. 928–930, 2016.

76. N. Thompson, R. Bahran, G. Winters, E. Frantz, R. Gazda, B. McDermott, J. Wei, P. Caracappa, T. Trumbull, J. Thompson, and Y. Danon, "Nuclear engineering education

at the RPI walthousen reactor critical facility," *Proceedings of the Institute of Nuclear Materials Management 56th Annual Meeting*, 2015.

77. A. Trahan, "Utilization of the differential die-away self-interrogation technique for characterization of spent nuclear fuel," *University of Michigan Ph.D. thesis*, 2016.

78. M. E. Anderson and R. A. Neff, "Neutron energy spectra of different size ^{239}Pu-Be(α,n) sources," *Nuclear Instruments and Methods*, vol. 99, pp. 231–235, 1972.

79. S. Bolding, "Design of a neutron spectrometer and simulations of neutron multiplicity experiments with nuclear data perturbations," *Kansas State University M.S. thesis*, 2013.

80. M. A. Smith-Nelson and J. D. Hutchinson, "The Sm2 ratio for evaluating neutron multiplicity models," *Los Alamos National Laboratory Report, LA-UR-14-29047*, 2014.

81. A. McSpaden, M. Nelson, and J. Hutchinson, "Eliminating detector response in neutron multiplicity measurements for model evaluation," *Transactions of the American Nuclear Society*, vol. 117, 2017.

82. J. Mullins, "Pop!" *New Scientist*, vol. 38, pp. 40–44, 2005.

83. N. Thompson, J. Hutchinson, R. Bahran, E. Dumonteil, and W. Monage, "Neutron clustering measurements at rpi," *Nuclear Criticality Safety Program (NCSP) Technical Program Review*, 2018.

84. J. Arthur, R. Bahran, J. Hutchinson, and S. Pozzi, "Bayesian optimization for subcritical benchmark design," *American Nuclear Society Winter Meeting and Technology Expo*, 2018.

85. J. Hutchinson, R. Bahran, T. Cutler, and et al., "Subcritical copper-reflected α-phase plutonium (scrαp) measurements and simulations," *International Conference on Mathematics and Computational Methods Applied to Nuclear Science and Engineering, LA-UR-17-20621*, 2017.

86. J. Arthur, R. Bahran, J. Hutchinson, T. Grove, and S. Pozzi, "Improved figure of merit for feynman histograms," *Transactions of the American Nuclear Society Winter Meeting and Technology Expo*, 2017.

87. M. Rising *et al.*, "Correlated neutron and gamma-ray emissions in MCNP6," *ANS Winter Meeting and Nuclear Technology Expo*, 2014.

88. C. Hagmann *et al.*, "FREYA-A new monte carlo code for improved modeling of fission chains," *IEEE Transactions on Nuclear Science*, vol. 60, pp. 545–549, 2013.

89. S. Pozzi *et al.*, "MCNPX-PoliMi for nuclear nonproliferation applications," *Nuclear Instruments and Methods in Physics Research Section A*, vol. 694, pp. 119–125, 2012.

90. S. A. Pozzi, E. Padovani, and M. Marseguerra, "MCNP-PoliMi: a monte carlo code for correlation measurements," *Nuclear Instruments and Methods in Physics Research A*, vol. 513, pp. 550–558, 2003.

91. *MCNP6^{TM} User's Manual, Version 1.0*, May 2013.

92. J. M. Verbeke, J. Randrup, and R. Vogt, "Fission reaction yield algorithm FREYA user manual 2.0," *Lawrence Livermore National Laboratory report LLNL-SM-705798*, 2016.

93. W. Hauser and H. Feshbach, "The inelastic scattering of neutrons," *Physical Review 87*, 1952.

94. E. Padovani, S. A. Pozzi, S. D. Clarke, and E. C. Miller, *MCNPX-PoliMi User's Manual, C00791 MNYCP, Radiation Safety Information Computational Center, Oak Ridge National Laboratory*, 2012.

95. J. Hutchinson and D. Loaiza, "Plutonium sphere reflected by beryllium," *International Handbook of Evaluated Criticality Safety Benchmark Experiments, NEA/NSC/-DOC/(95)03/I, PU-MET-FAST-038*, 2007.

96. E. C. Miller, "Characterization of fissionable material using a time-correlated pulse-height technique for liquid scintillators," *University of Michigan PhD Thesis*, 2012.

97. S. Bolding, "Design of a neutron spectrometer and simulations of neutron multiplicity experiments with nuclear data perturbations," *Kansas State University M.S. thesis*, 2013.

98. E. C. Miller, J. K. Mattingly, S. D. Clarke, C. J. Solomon, B. Dennis, A. Meldrum, and S. A. Pozzi, "Computational evaluation of neutron multiplicity measurements of polyethylene-reflected plutonium metal," *Nuclear Science and Engineering*, vol. 176, no. 2, pp. 167–185, 2014.

99. M. E. Rising, F. B. Brown, and J. L. Alwin, "Using whisper-1.1 to guide improvements to nuclear data evaluations," *ANS 2017 Nuclear Criticality Safety Division Topical*, 2017.

100. J. Arthur, R. Bahran, J. Hutchinson, and S. A. Pozzi, "Genetic algorithm for nuclear data evaluation applied to subcritical neutron multiplication inference benchmark experiments," *Submitted to Annals of Nuclear Energy*, 2018.

101. L. Chen, C. Yan, Y. Liao, F. Song, and Z. Jia, "A hybrid non-dominated sorting genetic algorithm and its application on multi-objective optimal design of nuclear power plant," *Annals of Nuclear Energy*, vol. 100, pp. 150–159, 2017.

102. A. Kumar and P. V. Tsvetkov, "A new approach to nuclear reactor design optimization using genetic algorithms and regression analysis," *Annals of Nuclear Energy*, vol. 85, pp. 27–35, 2015.

103. M. Massone, F. Gabrielli, and A. Rineiski, "A genetic algorithm for multigroup energy structure search," *Annals of Nuclear Energy*, vol. 105, pp. 369–387, 2017.

104. A. Sobolev, A. Gazetdinov, and D. Samokhin, "Genetic algorithms for nuclear reactor fuel load and reload optimization problems," *Nuclear Energy and Technology*, vol. 3, pp. 231–235, 2017.

105. E. Israeli and E. Gilad, "Novel genetic algorithm for loading pattern optimization based on core physics heuristics," *Annals of Nuclear Energy*, vol. 118, pp. 35–48, 2018.

106. B. Li and L. Lu, "Genetic-algorithm-based fault detection of the heat transfer process in nuclear-based hydrogen production based on Cu-Cl cycle," *International Journal of Hydrogen Energy*, vol. 42, pp. 3863–3875, 2017.

107. M. Chadwick *et al.*, "ENDF/B-VII.1 nuclear data for science and technology: Cross sections, covariances, fission product yields and decay data," *Nuclear Data Sheets*, vol. 112, pp. 2887–2996, 2011.

108. P. Talou, "Personal correspondance."

Appendix A

RCF PuBe source

The PuBe shielding is a cylinder with outer dimensions of 12"x12". It is known to be made of paraffin wax with a hole in the center in which the source resides. It is assumed that the hole is cylindrical and extends from the top to the bottom of the shielding. According to RCF records, the source strength is on the order of 1E7 n/s and the hole diameter is on the order of 1 in. Using this shielding configuration and source strength in the CaSPER configuration 3 simulations did not yield a good match between simulated and measured results, as shown in Figure A.1. It was judged that either the source strength, shielding, or both could not be correct.

The source strength and hole diameter were then varied until a good match between simulated and experimental results for configuration 3 was found, as shown in Figure A.2. The optimized hole diameter and source strength are 3.8 in. and 1.4E7, respectively.

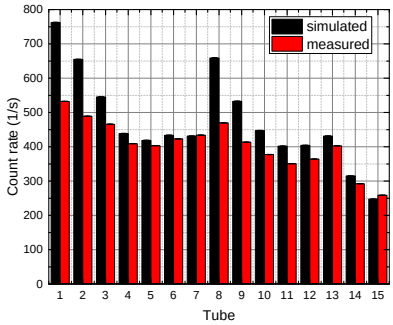

Figure A.1: Initial comparison between simulated and measured counts-per-tube histograms for configuration 3. The FOM value characterizing this comparison is 201686.

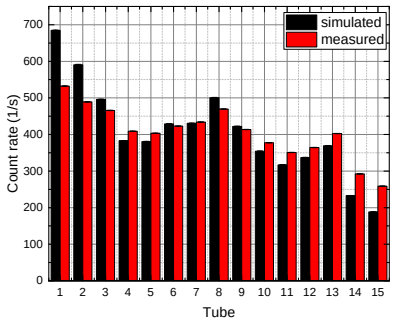

FIGURE A.2: Final comparison between simulated and measured counts-per-tube histograms for configuration 3. The FOM value characterizing this comparison is 49597.

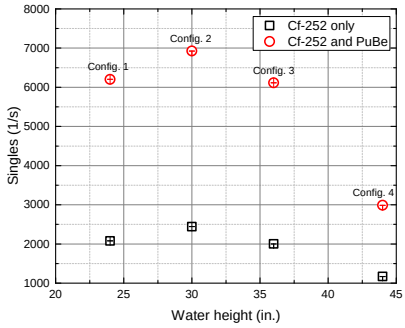

FIGURE A.3: Simulated contribution of the RCF PuBe starter source to the singles rate at different water heights, as compared to the singles rate due to ^{252}Cf alone.

The PuBe source constitutes the largest contribution to the singles rate. Figure A.3 and Table show only roughly 33-40% of singles are due to the ^{252}Cf source. Because this is simulated data it was possible to separate out the count rate due to ^{252}Cf alone, by simply not modeling the PuBe source.

TABLE A.1: Comparison of percentage contributions of the RCF PuBe source and the ^{252}Cf source.

Water height (in.)	^{252}Cf % contribution	PuBe % contribution
24	34	66
30	35	65
36	33	67
44	39	61

Appendix B

Leakage Multiplication Calculations

Equations 1.15-1.16 are true only if the (α, n) neutron emission rate from the fission source is assumed to be negligible. Theoretically, this would be the case in a system consisting of only a ^{252}Cf starter source and low-enriched uranium fuel. However, the large contribution to the measured signal from the RCF PuBe source (roughly 1E7 $\frac{n}{s}$ in strength) above the core renders this assumption inaccurate. Equations B.1-B.4 are used instead of the previous equations when the (α, n) neutron contribution is not negligible. These equations also assume that the (α, n) source and the fission source are coincident point sources; i.e., a small sample of uranium or plutonium oxide. Therefore, they are also not completely valid for the CaSPER measurement.

$$R_1 = \epsilon \left[b_{11} F_s + b_{12} S_\alpha \right] \tag{B.1}$$

$$R_2 = \epsilon^2 \left[b_{21} F_s + b_{22} S_\alpha \right] \tag{B.2}$$

$$b_{11} = M_L \nu_{s1} \; b_{12} = M_L \tag{B.3}$$

$$b_{21} = M_L^2 \left[\nu_{s2} + \frac{M_L - 1}{\nu_{I1} - 1} \nu_{s1} \nu_{I2} \right] \; b_{22} = M_L^2 \frac{M_L - 1}{\nu_{I1} - 1} \nu_{I2} \tag{B.4}$$

Two new methods for calculating leakage multiplication were primarily investigated. In method 1, it is assumed that $M_L = 1$ at the 24 in. water height configuration. Therefore, efficiency can be solved for at this configuration. This calculated efficiency is, as expected, very different from the value obtained using the typical method of taking the ratio of the

TABLE B.1: Adjusted efficiencies for each water height.

Water height (in.)	Efficiency	Adjusted efficiency
24	0.0506	0.00759
30	0.0530	0.00800
36	0.0430	0.00645
44	0.0149	0.00223
67	0.0001	0.00002

singles rate in the corresponding no-fuel measurement to the known ^{252}Cf source strength. The ratio of the "adjusted efficiency" to the typically calculated efficiency is then used as a multiplier to calculate adjusted efficiencies at all other water heights. Table B.1 lists the original and adjusted efficiencies for each water height. These adjusted efficiencies are used to calculate leakage multiplication.

It is clear that the original efficiencies are incorrect. From previous measurements with the NoMAD it is known that the absolute efficiency at a distance of 50 cm away from a ^{252}Cf source in air is on the order of 1%. Because the source-detector distance is 48.5 cm and at 24 in. water height the water level has not yet reached the bottom of the NoMAD, the efficiency value is expected to be much closer to 1% than 5%. Therefore, the adjusted efficiency values are much more realistic.

In method 2, equations for R_1 and R_2 [35] are manipulated to separate the contributions from the ^{252}Cf and PuBe sources. Efficiency is assumed to be a constant multiplied by the relative contributions of each source. It is also assumed that $M_L = 1$ at the 24 in. water height configuration. As shown in Equations B.5 and B.6, this becomes a system of 2 equations and 2 unknowns (efficiency constant ϵ and (α,n) source strength S_α). Because the solution of this system of equations yields the PuBe source strength, 1.12E5 $\frac{n}{s}$ (which is more of an effective source strength that treats the shielded above-core PuBe source as an unshielded point source coincident in space with the ^{252}Cf spontaneous fission source), this value can be input into the system of equations in B.7 and B.9. Therefore, ϵ and M_L can be solved for at all other configurations.

$$R_1 = \epsilon \left[f_{Cf} \nu_{s1} F_s + f_{PuBe} S_\alpha \right] \tag{B.5}$$

$$R_2 = \epsilon^2 \left[f_{Cf}^2 \nu_{s2} F_s + f_{PuBe}^2 S_\alpha \right] \tag{B.6}$$

$$R_1 = \epsilon \left[f_{Cf} b_{11} F_s + f_{PuBe} b_{12} S_\alpha \right] \tag{B.7}$$

$$b_{11} = M_L \nu_{s1} \; b_{12} = M_L \tag{B.8}$$

$$R_2 = \epsilon^2 \left[f_{Cf}^2 b_{21} F_s + f_{PuBe}^2 b_{22} S_\alpha \right] \tag{B.9}$$

$$b_{21} = M_L^2 \left[\nu_{s2} + \frac{M_L - 1}{\nu_{I1} - 1} \nu_{s1} \nu_{I2} \right] \; b_{22} = M_L^2 \frac{M_L - 1}{\nu_{I1} - 1} \nu_{I2} \tag{B.10}$$

Both methods of calculating leakage multiplication yield reasonable results for configurations 1-4, as seen in Figure B.1. However, method 2 shows an unreasonable trend versus CR height for configurations 5-7, as shown in Figure B.2. Therefore, method 1 was used to calculate final leakage multiplication results for this work. This complication with efficiency and leakage multiplication calculation is one of the reasons why the CaSPER measurements cannot be a benchmark. Additional measurements taken during the execution of CaSPER may have provided better estimates of efficiency.

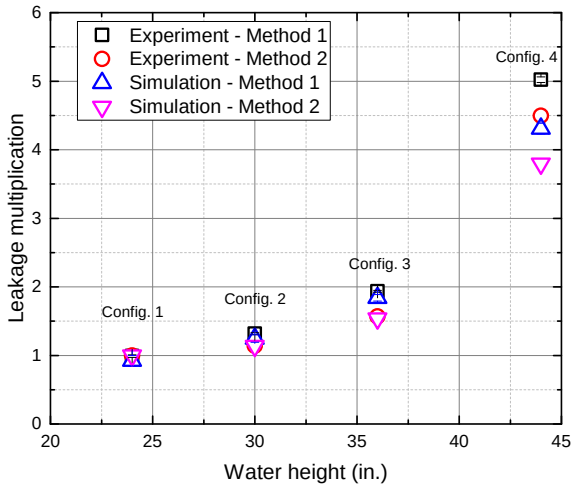

FIGURE B.1: Neutron leakage multiplication as a function of water height.

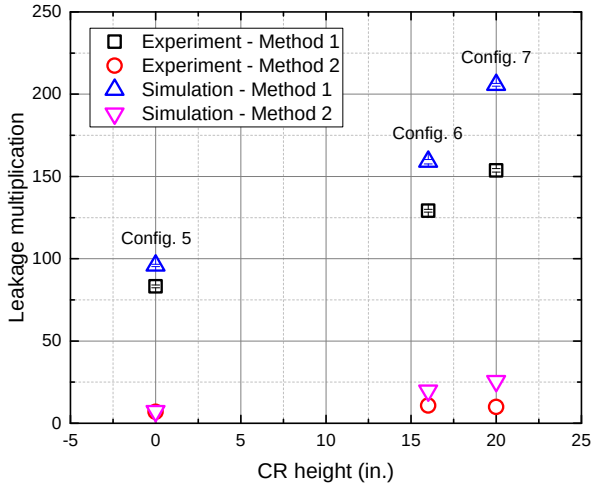

FIGURE B.2: Neutron leakage multiplication as a function of CR height.

Appendix C

Induced Fission Neutron Multiplicity Distributions

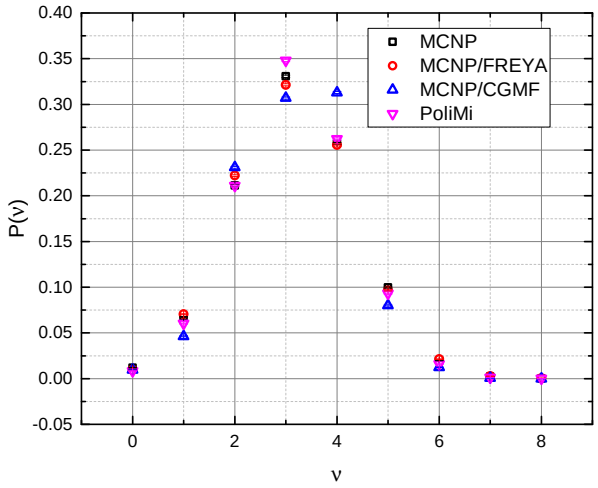

Figure C.1: ^{239}Pu induced fission multiplicity distributions for 0.5 in. W thickness.

Table C.1: ^{239}Pu induced fission multiplicity distribution parameters for 0.5 in. W thickness.

Code	$\bar{\nu}$	σ
MCNP	3.14	1.44
MCNP/FREYA	3.13	1.46
MCNP/CGMF	3.16	1.23
PoliMi	3.15	1.31

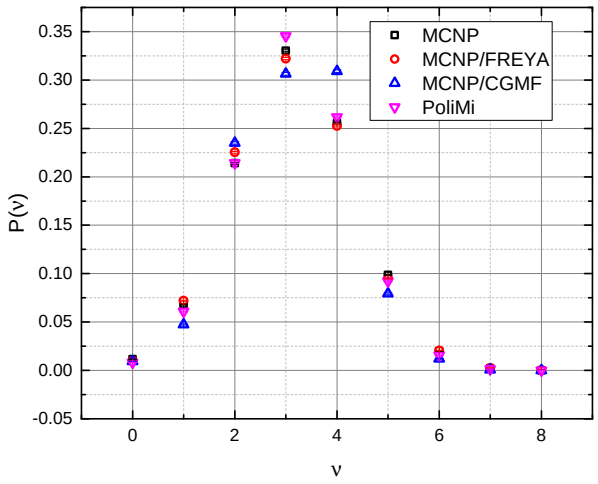

FIGURE C.2: ^{239}Pu induced fission multiplicity distributions for 1.0 in. W thickness.

TABLE C.2: ^{239}Pu induced fission multiplicity distribution parameters for 1.0 in. W thickness.

Code	$\bar{\nu}$	σ
MCNP	3.14	1.44
MCNP/FREYA	3.12	1.45
MCNP/CGMF	3.15	1.24
PoliMi	3.14	1.31

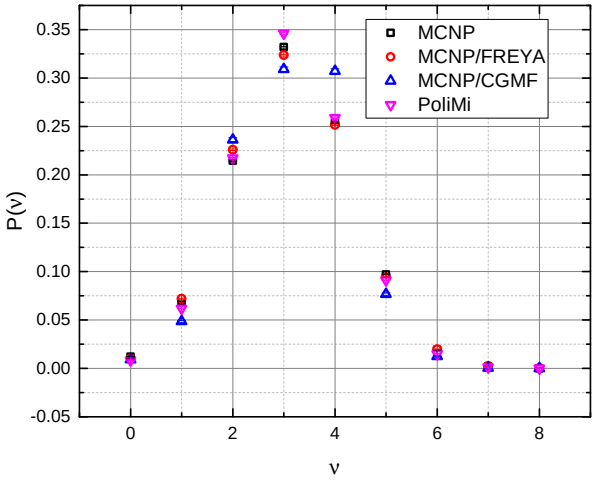

FIGURE C.3: ^{239}Pu induced fission multiplicity distributions for 2.0 in. W thickness.

TABLE C.3: ^{239}Pu induced fission multiplicity distribution parameters for 2.0 in. W thickness.

Code	$\bar{\nu}$	σ
MCNP	3.12	1.43
MCNP/FREYA	3.11	1.45
MCNP/CGMF	3.14	1.23
PoliMi	3.12	1.31

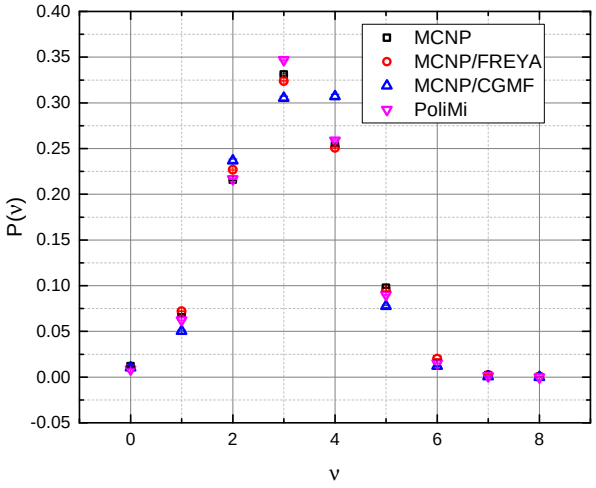

FIGURE C.4: ^{239}Pu induced fission multiplicity distributions for 2.5 in. W thickness.

TABLE C.4: ^{239}Pu induced fission multiplicity distribution parameters for 2.5 in. W thickness.

Code	$\bar{\nu}$	σ
MCNP	3.12	1.43
MCNP/FREYA	3.11	1.44
MCNP/CGMF	3.13	1.25
PoliMi	3.12	1.30

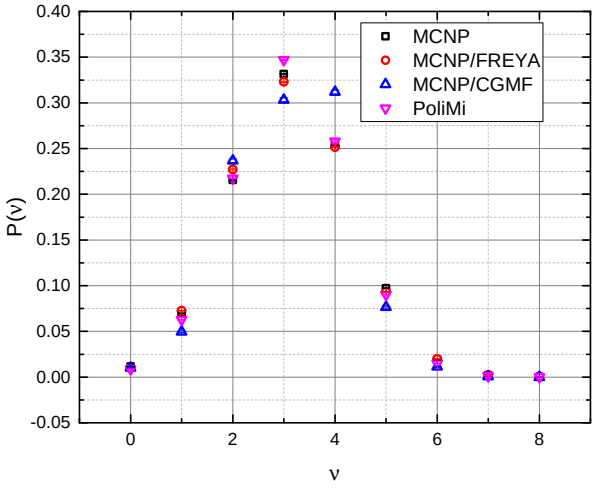

FIGURE C.5: ^{239}Pu induced fission multiplicity distributions for 2.75 in. W thickness.

TABLE C.5: ^{239}Pu induced fission multiplicity distribution parameters for 2.75 in. W thickness.

Code	$\bar{\nu}$	σ
MCNP	3.12	1.43
MCNP/FREYA	3.11	1.44
MCNP/CGMF	3.14	1.24
PoliMi	3.12	1.31

Appendix D

Feynman Histograms

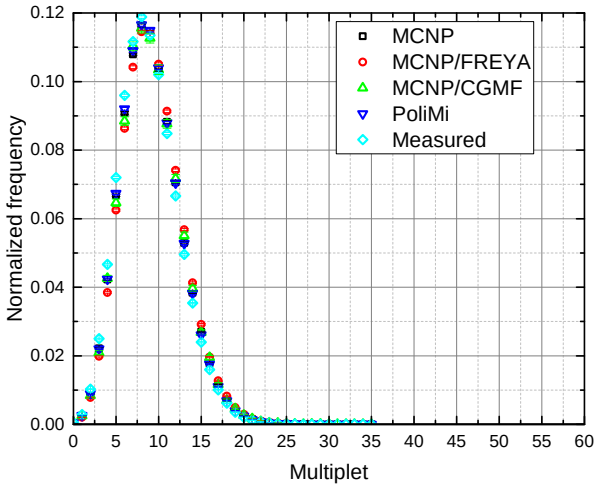

Figure D.1: Feynman histograms for 0.5 in. Ni thickness.

Table D.1: FOM values for the various simulated Feynman histograms, as compared to the measured histogram, for 0.5 in. Ni thickness.

Code	FOM
MCNP	34
MCNP/FREYA	84
MCNP/CGMF	6.3
PoliMi	27

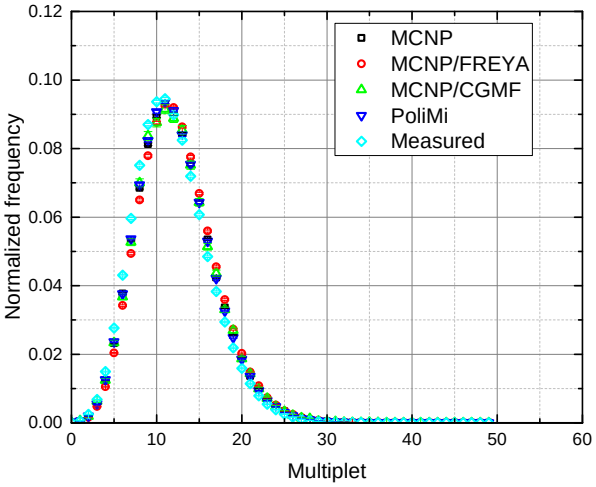

FIGURE D.2: Feynman histograms for 1 in. Ni thickness.

TABLE D.2: FOM values for the various simulated Feynman histograms, as compared to the measured histogram, for 1.0 in. Ni thickness.

Code	FOM
MCNP	38
MCNP/FREYA	71
MCNP/CGMF	29
PoliMi	27

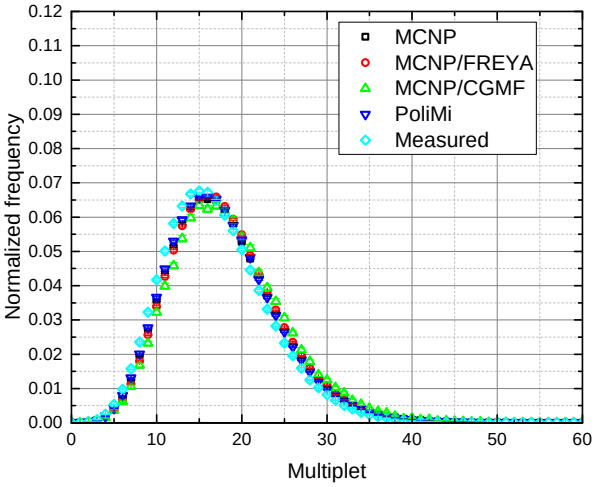

FIGURE D.3: Feynman histograms for 2 in. Ni thickness.

TABLE D.3: FOM values for the various simulated Feynman histograms, as compared to the measured histogram, for 2.0 in. Ni thickness.

Code	FOM
MCNP	35
MCNP/FREYA	41
MCNP/CGMF	23
PoliMi	24

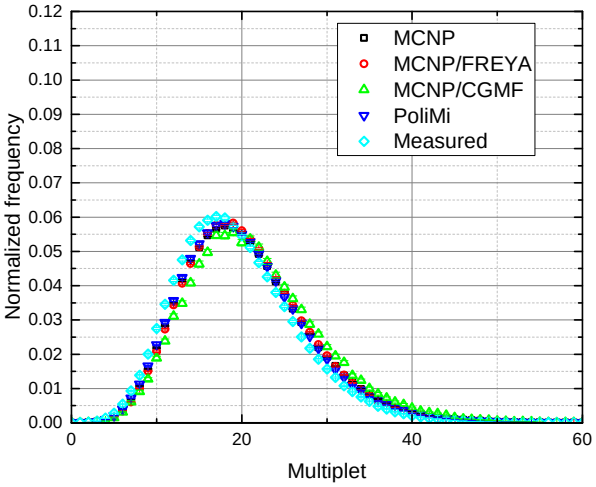

FIGURE D.4: Feynman histograms for 2.5 in. Ni thickness.

TABLE D.4: FOM values for the various simulated Feynman histograms, as compared to the measured histogram, for 2.5 in. Ni thickness.

Code	FOM
MCNP	43
MCNP/FREYA	41
MCNP/CGMF	27
PoliMi	26

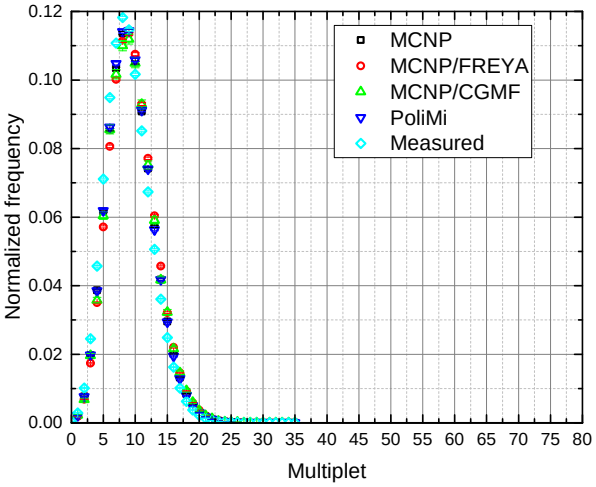

FIGURE D.5: Feynman histograms for 0.5 in. W thickness.

TABLE D.5: FOM values for the various simulated Feynman histograms, as compared to the measured histogram, for 0.5 in. Ni thickness.

Code	FOM
MCNP	13
MCNP/FREYA	50
MCNP/CGMF	50
PoliMi	8.2

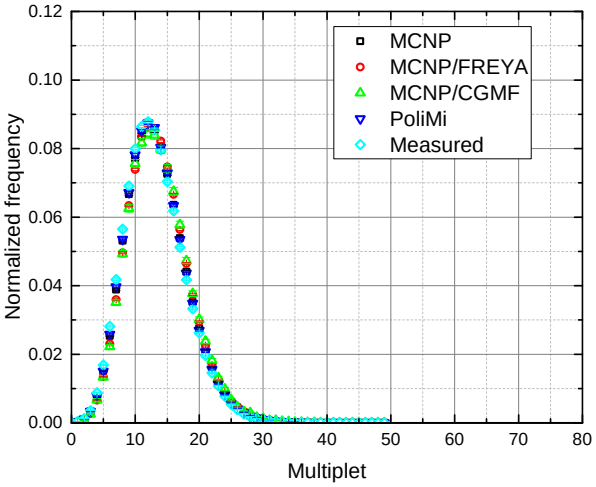

FIGURE D.6: Feynman histograms for 1 in. W thickness.

TABLE D.6: FOM values for the various simulated Feynman histograms, as compared to the measured histogram, for 1.0 in. Ni thickness.

Code	FOM
MCNP	3.1
MCNP/FREYA	12
MCNP/CGMF	2.9
PoliMi	2.0

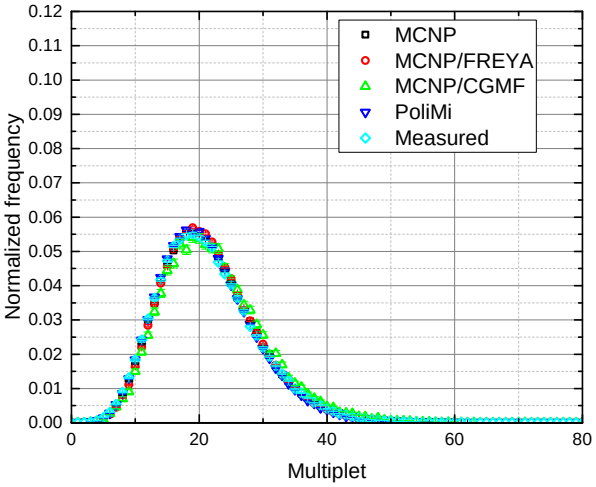

FIGURE D.7: Feynman histograms for 2 in. W thickness.

TABLE D.7: FOM values for the various simulated Feynman histograms, as compared to the measured histogram, for 2.0 in. Ni thickness.

Code	FOM
MCNP	1.2
MCNP/FREYA	5.0
MCNP/CGMF	1.7
PoliMi	4.4

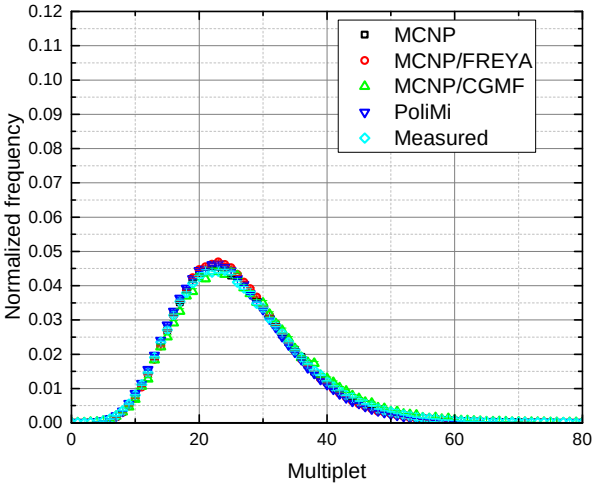

FIGURE D.8: Feynman histograms for 2.5 in. W thickness.

TABLE D.8: FOM values for the various simulated Feynman histograms, as compared to the measured histogram, for 2.5 in. Ni thickness.

Code	FOM
MCNP	1.2
MCNP/FREYA	7.3
MCNP/CGMF	2.5
PoliMi	5.7

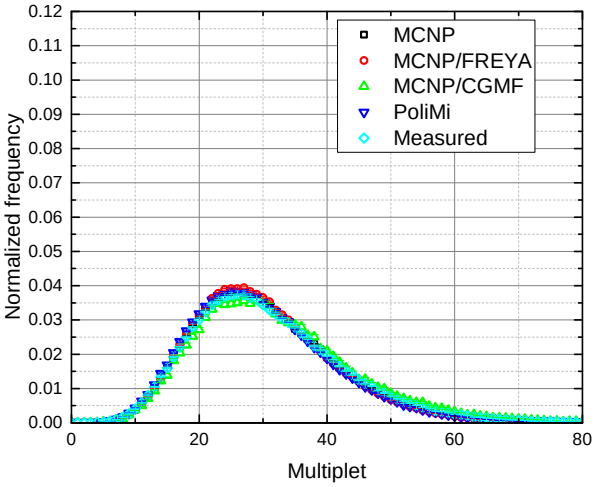

FIGURE D.9: Feynman histograms for 2.75 in. W thickness.

TABLE D.9: FOM values for the various simulated Feynman histograms, as compared to the measured histogram, for 2.75 in. W thickness.

Code	FOM
MCNP	0.73
MCNP/FREYA	3.7
MCNP/CGMF	4.8
PoliMi	2.6

Appendix E

Pearson Correlation Coefficients

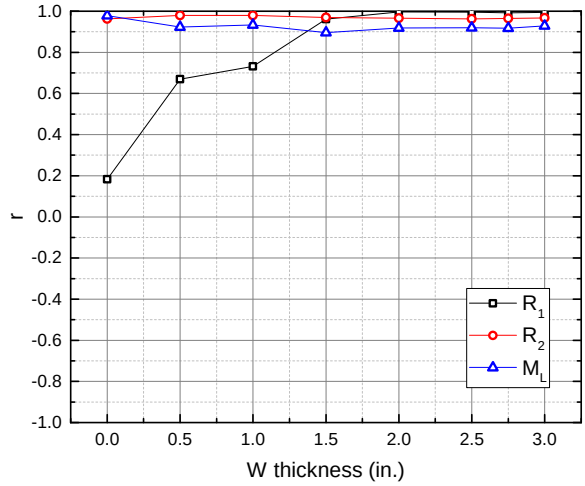

Figure E.1: Pearson correlation coefficient "r" plotted for all observables of interest vs. SF $\bar{\nu}$, across all configurations of the BeRP-W benchmark.

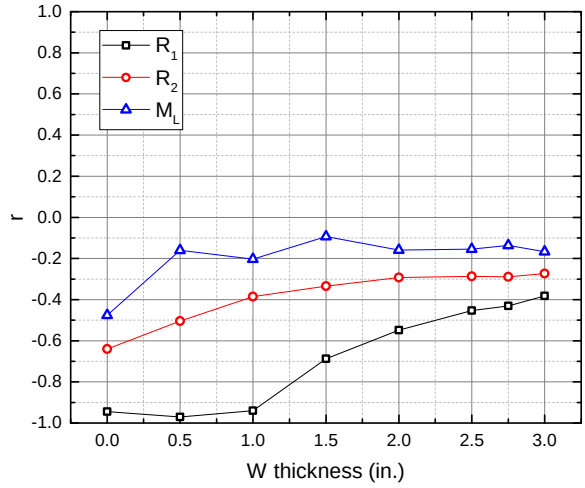

FIGURE E.2: Pearson correlation coefficient "r" plotted for all observables of interest vs. SF σ, across all configurations of the BeRP-W benchmark.

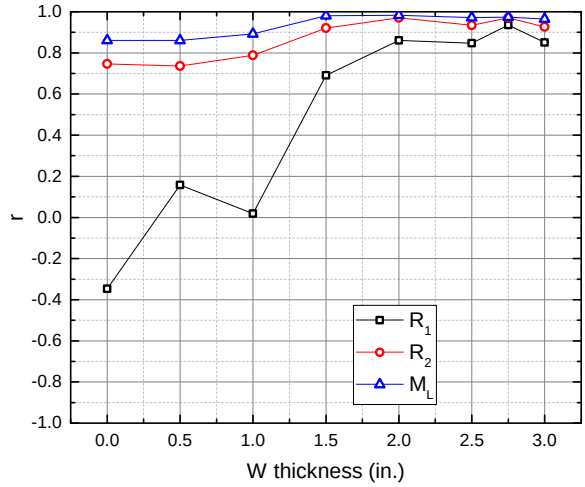

FIGURE E.3: Pearson correlation coefficient "r" plotted for all observables of interest vs. IF $\bar{\nu}$, across all configurations of the BeRP-W benchmark.

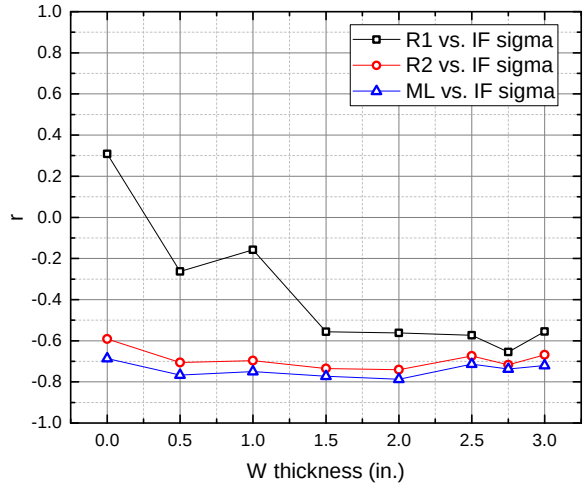

FIGURE E.4: Pearson correlation coefficient "r" plotted for all observables of interest vs. IF σ, across all configurations of the BeRP-W benchmark.

Appendix F

Genetic Algorithm

```
% Genetic algorithm for nuclear data evaluation
% Population size and mutation rate
N=1000;
m=.1;
% Nuclear data and uncertainties
IFnubar=1;
IFnubar_unc=.003;
IFsigma=1.140;
IFsigma_unc=.01*IFsigma;
SFnubar=2.151;
SFnubar_unc=0.005;
SFsigma=1.151;
SFsigma_unc=.01*SFsigma;
% Initial (C-E)/E values
m1_CE=[0.025108632
0.03762409
0.040465196
0.046176578
0.056109544
0.058480974
0.070012982
0.039610168
0.017926472
0.008552891
0.000611237
-0.00088428
-0.005308258
```

−0.005314369
−0.009440708
0.046369878
0.035963416
0.034218905
0.034705089
0.037152819
0.01018538
0.042755236
0.008619478
0.01106585
0.047165462
0.052884741
0.058475862
0.043362488
0.043238203
0.038441401
0.022475098
0.034594993
];
m2_CE=[0.050225916
0.076119226
0.08223573
0.094707349
0.116287992
0.121419587
0.146479786
0.080153389
0.034829913
0.015311539
−0.001265873
−0.004792699
−0.013872384
−0.014274596
−0.022579003
0.094079813

```
0.07192847
0.068188313
0.068988165
0.073699128
0.018670062
0.085627172
0.015403844
0.01999295
0.094853595
0.107293784
0.11914902
0.088024086
0.087157035
0.075828782
0.041614477
0.071122287
];
% Sensitivities of (C-E)/E values to 1unc in nuclear data
m1_IFnubar=[0.00992215
0.015354454
0.020772254
0.026816607
0.033641415
0.041249138
0.050531227
0.010424061
0.015329083
0.021684517
0.030298192
0.043239
0.063514072
0.078869125
0.102756363
0.01015977
0.014788683
0.020049262
```

0.026100399
0.033577089
0.038591369
0.0429107
0.054930458
0.052506764
0.05474631
0.071299476
0.100912836
0.149831218
0.276966442
−0.013205428
0.0326124
0.094144898
];
m2_IFnubar=[0.02172178
0.035918298
0.052034363
0.07301992
0.101054679
0.137041941
0.188921583
0.023048638
0.035229551
0.053613002
0.083938767
0.142542176
0.263000729
0.375944686
0.582106529
0.022310263
0.033455391
0.047903924
0.066888516
0.094229813
0.115191803

0.134539628
0.201196856
0.186896161
0.195227492
0.297430829
0.528965081
1.222129641
1.878075776
−0.006686265
0.081937746
0.304738979
];
m1_IFsigma=[−8.95901E−07
−3.16602E−05
−3.99307E−06
4.24605E−06
8.10978E−06
−2.74132E−05
−4.67786E−06
2.3276E−07
1.49476E−05
−1.70485E−05
−2.90562E−07
−2.2779E−05
−4.19647E−05
−4.22187E−05
−2.68662E−05
−2.71594E−06
−5.37163E−05
−9.06034E−06
−7.70375E−05
−9.06008E−05
−3.35497E−05
−0.00012218
−3.15933E−05
−2.36343E−06

−0.000145765
−0.00018083
−0.000176496
−6.59959E−05
−0.00012115
−0.000192916
−0.000148859
6.22123E−05
];
m2_IFsigma=[8.87402E−05
6.28339E−05
0.000155301
0.000197116
0.000238014
0.000187745
0.00026891
0.000109164
0.000159361
0.000121912
0.000198071
0.000207813
0.000181782
0.000196026
0.000241662
7.52042E−05
1.84399E−05
0.000135956
2.26296E−05
1.22308E−05
0.000141337
−4.11607E−05
0.000190192
0.000247546
−5.15881E−05
−0.000119882
−0.000103748

0.000183501
6.61964E−05
−0.00012123
−7.21425E−06
0.00041637
];
m1_SFnubar=[0.00232446
0.002341715
0.002330113
0.002355311
0.002358248
0.00234133
0.002388602
0.002357305
0.002285622
0.002261687
0.002224935
0.002245753
0.002226112
0.002207743
0.002181886
0.004667581
0.004568043
0.004545085
0.004502857
0.004535697
0.004403078
0.004466548
0.004457756
0.004409575
0.004463292
0.004459376
0.004455056
0.004475943
0.004512863
0.004318773

```
0.004215
0.004610021
];
m2_SFnubar=[0.004671126
0.00476424
0.004701691
0.004768146
0.004805125
0.004756131
0.004904416
0.004815999
0.004542273
0.004437531
0.004277647
0.00428345
0.004196362
0.004128595
0.004076126
0.009616593
0.009265122
0.009125257
0.008967102
0.008963653
0.008543291
0.008773372
0.008614101
0.008533961
0.008756375
0.008687038
0.008609125
0.008838063
0.008773098
0.008227199
0.007768441
0.009190191
];
```

m1_SFsigma=[0.000110008
8.27354E-05
8.88975E-05
0.000100075
8.75857E-05
8.9741E-05
8.72116E-05
8.37132E-05
6.71979E-05
0.000134549
5.8554E-05
9.3059E-05
7.16154E-05
6.25021E-05
7.19101E-05
0.000150453
0.000166846
0.000148452
0.000140247
0.000209414
0.000127255
0.000117377
0.000104157
9.73769E-05
0.000148376
0.000173982
0.000163599
0.000133368
0.00014343
0.000208418
-4.58739E-05
0.000179752
];
m2_SFsigma=[0.000267538
0.000232735
0.000230463

```
0.000245023
0.000222186
0.000234234
0.000222107
0.000197137
0.000160334
0.000298733
0.000149427
0.000209307
0.000181726
0.000148721
0.00017953
0.000351395
0.000382718
0.000337714
0.000303267
0.000457788
0.000282986
0.000264264
0.000241886
0.00021857
0.000335677
0.000370667
0.000361238
0.000314162
0.000332648
0.000445085
-7.20845E-05
0.00039997
];
% Experimental uncertainties (relative)
m1_unc=ones(32,1);
m2_unc=m1_unc;
% Original fitness
f_original=sum(abs(m1_CE.*m1_unc)+abs(m2_CE.*m2_unc));
```

```
% Create a population of N elements with random genetic material
% In this case, normal distributions around the current nubar and sigma value
% using the corresponding uncertainties
P_new=zeros(N,4);
P_new(:,1)=normrnd(IFnubar,IFnubar_unc,N,1);
P_new(:,2)=normrnd(IFsigma,IFsigma_unc,N,1);
P_new(:,3)=normrnd(SFnubar,SFnubar_unc,N,1);
P_new(:,4)=normrnd(SFsigma,SFsigma_unc,N,1);

f=-f_original;
fitness_old=f_original;

n=1;
% Continue main loop until fitness converges
while abs((f-fitness_old)/fitness_old)>.0000001 || n<100
    % Generation counter
    n=n+1;
    P=P_new;
    fitness_old=f;
    % Calculate fitness for N elements
    fitness=zeros(N,1);
    for i=1:length(P)
        % Calculate new (C-E)/E values using sensitivities, and folding
        % in both correlation matrix and experimental uncertainties
        m1_temp=m1_CE+m1_IFnubar.*(P(i,1)-IFnubar)/IFnubar_unc+m1_IFsigma.*(P
        m2_temp=m2_CE+m2_IFnubar.*(P(i,1)-IFnubar)/IFnubar_unc+m2_IFsigma.*(P
        fitness(i)=sum(abs(m1_temp.*m1_unc)+abs(m2_temp.*m2_unc));
    end
    % Record best fitness
    [f,pos]=min(fitness);
    % Reproduction/selection N times
    % Pick first 2 parents less than a random number
    P_new=zeros(N,4);
    for i=1:N
        ind=[];
        while length(ind)<2
```

```
    x=rand()*(max(fitness)-min(fitness))+min(fitness);
    ind=find(fitness<=x);
    ind=ind(randperm(length(ind)));
end
parents=ind(1:2);
% Crossover, with small mutation probability
P_new(i,1)=mean([P(parents(1),1),P(parents(2),1)]);
if rand()<=m
    P_new(i,1)=normrnd(IFnubar,IFnubar_unc,1,1);
end
if P_new(i,1)<IFnubar-IFnubar_unc
    P_new(i,1)=IFnubar-IFnubar_unc;
elseif P_new(i,1)>IFnubar+IFnubar_unc
    P_new(i,1)=IFnubar+IFnubar_unc;
end
P_new(i,2)=mean([P(parents(1),2),P(parents(2),2)]);
if rand()<=m
    P_new(i,2)=normrnd(IFsigma,IFsigma_unc,1,1);
end
if P_new(i,2)<IFsigma-IFsigma_unc
    P_new(i,2)=IFsigma-IFsigma_unc;
elseif P_new(i,2)>IFsigma+IFsigma_unc
    P_new(i,2)=IFsigma+IFsigma_unc;
end
P_new(i,3)=mean([P(parents(1),3),P(parents(2),3)]);
if rand()<=m
    P_new(i,3)=normrnd(SFnubar,SFnubar_unc,1,1);
end
if P_new(i,3)<SFnubar-SFnubar_unc
    P_new(i,3)=SFnubar-SFnubar_unc;
elseif P_new(i,3)>SFnubar+SFnubar_unc
    P_new(i,3)=SFnubar+SFnubar_unc;
end
P_new(i,4)=mean([P(parents(1),4),P(parents(2),4)]);
if rand()<=m
    P_new(i,4)=normrnd(SFsigma,SFsigma_unc,1,1);
```

```
            end
            if P_new(i,4)<SFsigma-SFsigma_unc
                P_new(i,4)=SFsigma-SFsigma_unc;
            elseif P_new(i,4)>SFsigma+SFsigma_unc
                P_new(i,4)=SFsigma+SFsigma_unc;
            end
        end
    end
    % Optimized solution
    solution=P(pos,:);
    improvement=(f-f_original)/f_original;
    m1_CE_new=m1_CE+m1_IFnubar.*(solution(1)-IFnubar)/IFnubar_unc+m1_IFsigma.*(so
    m2_CE_new=m2_CE+m2_IFnubar.*(solution(1)-IFnubar)/IFnubar_unc+m2_IFsigma.*(so
```

Appendix G

(C-E)/E Values and Sensitivities

All original (C-E)/E values used in the genetic algorithm are listed in Table G.1. The predetermined (C-E)/E sensitivities are listed in Table G.2.

TABLE G.1: Original (C-E)/E values used in genetic algorithm.

Configuration #	m_1 (C-E)/E	m_2 (C-E)/E
1	0.025109	0.050226
2	0.037624	0.076119
3	0.040465	0.082236
4	0.046177	0.094707
5	0.056110	0.116288
6	0.058481	0.121420
7	0.070013	0.146480
8	0.039610	0.080153
9	0.017926	0.034830
10	0.008553	0.015312
11	0.000611	-0.001266
12	-0.000884	-0.004793
13	-0.005308	-0.013872
14	-0.005314	-0.014275
15	-0.009441	-0.022579
16	0.046370	0.094080
17	0.035963	0.071928
18	0.034219	0.068188
19	0.034705	0.068988
20	0.037153	0.073699
21	0.010185	0.018670
22	0.042755	0.085627
23	0.008619	0.015404
24	0.011066	0.019993
25	0.047165	0.094854
26	0.052885	0.107294
27	0.058476	0.119149
28	0.043362	0.088024
29	0.043238	0.087157
30	0.038441	0.075829
31	0.022475	0.041614
32	0.034595	0.071122

TABLE G.2: Pre-determined (C-E)/E sensitivities used in genetic algorithm.

Configuration #	$\frac{\partial\left(\frac{C-E}{E}\right)_{m_1}}{\partial\sigma_I}$	$\frac{\partial\left(\frac{C-E}{E}\right)_{m_2}}{\partial\sigma_I}$	$\frac{\partial\left(\frac{C-E}{E}\right)_{m_1}}{\partial\bar{\nu}_S}$	$\frac{\partial\left(\frac{C-E}{E}\right)_{m_2}}{\partial\bar{\nu}_S}$	$\frac{\partial\left(\frac{C-E}{E}\right)_{m_1}}{\partial\sigma_S}$	$\frac{\partial\left(\frac{C-E}{E}\right)_{m_2}}{\partial\sigma_S}$
1	-0.000001	0.000089	0.002324	0.004671	0.000110	0.000268
2	-0.000032	0.000063	0.002342	0.004764	0.000083	0.000233
3	-0.000004	0.000155	0.002330	0.004702	0.000089	0.000230
4	0.000004	0.000197	0.002355	0.004768	0.000100	0.000245
5	0.000008	0.000238	0.002358	0.004805	0.000088	0.000222
6	-0.000027	0.000188	0.002341	0.004756	0.000090	0.000234
7	-0.000005	0.000269	0.002389	0.004904	0.000087	0.000222
8	0.000000	0.000109	0.002357	0.004816	0.000084	0.000197
9	0.000015	0.000159	0.002286	0.004542	0.000067	0.000160
10	-0.000017	0.000122	0.002262	0.004438	0.000135	0.000299
11	0.000000	0.000198	0.002225	0.004278	0.000059	0.000149
12	-0.000023	0.000208	0.002246	0.004283	0.000093	0.000209
13	-0.000042	0.000182	0.002226	0.004196	0.000072	0.000182
14	-0.000042	0.000196	0.002208	0.004129	0.000063	0.000149
15	-0.000027	0.000242	0.002182	0.004076	0.000072	0.000180
16	-0.000003	0.000075	0.004668	0.009617	0.000150	0.000351
17	-0.000054	0.000018	0.004568	0.009265	0.000167	0.000383
18	-0.000009	0.000136	0.004545	0.009125	0.000148	0.000338
19	-0.000077	0.000023	0.004503	0.008967	0.000140	0.000303
20	-0.000091	0.000012	0.004536	0.008964	0.000209	0.000458
21	-0.000034	0.000141	0.004403	0.008543	0.000127	0.000283
22	-0.000122	-0.000041	0.004467	0.008773	0.000117	0.000264
23	-0.000032	0.000190	0.004458	0.008614	0.000104	0.000242
24	-0.000002	0.000248	0.004410	0.008534	0.000097	0.000219
25	-0.000146	-0.000052	0.004463	0.008756	0.000148	0.000336
26	-0.000181	-0.000120	0.004459	0.008687	0.000174	0.000371
27	-0.000176	-0.000104	0.004455	0.008609	0.000164	0.000361
28	-0.000066	0.000184	0.004476	0.008838	0.000133	0.000314
29	-0.000121	0.000066	0.004513	0.008773	0.000143	0.000333
30	-0.000193	-0.000121	0.004319	0.008227	0.000208	0.000445
31	-0.000149	-0.000007	0.004215	0.007768	-0.000046	-0.000072
32	0.000062	0.000416	0.004610	0.009190	0.000180	0.000400

Appendix H

Bayesian Optimization Algorithm

```
% Optimizes experimental sensitivites using Bayesian optimization
% Training points
xd=[1.52;3];
fd=[0.0016;1.6572e-04];
ind_d=[38;75];
% All points
x=transpose(.04:.04:4);
% Parameters (should be optimized with cross-validation)
l=1;
s=.000001;
A=10;
% Known function
y=[0.00098527000000000;0.00179210000000000;0.00212480000000000;0.0027085000

a=0;
c=0;
mu2=100;
sigma2=100;
% Until max training point is greater than all mu+sigma
while a+c<max(mu2+sigma2)
    % For all points
    I=length(xd);
    J=length(x);
    mu=zeros(J,1);
    sigma=zeros(J,1);
    for i=1:J
        xstar=x(i);
```

```
        % Calculate Kstar
        Kstar=zeros(I,1);
        for j=1:I
            Kstar(j)=exp(-.5/l*(xd(j)-xstar).^2);
        end
        % Calculate K
        K=zeros(I,I);
        for j=1:I
            for k=1:I
                K(j,k)=exp(-.5/l*(xd(j)-xd(k)).^2);
            end
        end
        % Calculate mean and stddev
        mu(i)=transpose(Kstar)*(K+s*eye(I))^-1*fd;
        sigma(i)=sqrt(1-transpose(Kstar)*(K+s*eye(I))^-1*Kstar);
    end
    % Maximize utility function
    u=mu+A*sigma;
    u(ind_d)=-10;
    [val,ind]=max(u);
    % Sample next training point and update
    xd=[xd;x(ind)];
    fd=[fd;y(ind)];
    ind_d=[ind_d;ind];
    % Current max of GP
    [a,b]=max(mu);
    c=sigma(b);
    mu2=mu;
    sigma2=sigma;
    mu2(b)=[];
    sigma2(b)=[];
end
[a,b]=max(mu);
solution=x(b);
err=sum((mu-y).^2);
l=length(fd);
```

```
% Plot
figure
plot(xd,fd,'*')
hold on
plot(x,y)
errorbar(x,mu,sigma)
legend('Sampled points','Actual curve','GP curve')
```